



CZECH TECHNICAL UNIVERSITY IN PRAGUE  
Faculty of Biomedical Engineering  
Department of Biomedical Technology

***BIO-MOLECULAR SENSORS FOR MOLECULAR  
DIAGNOSTICS IN NANOMEDICINE BASED ON  
COLOR CENTRES IN DIAMOND***

**Doctoral Thesis**

***Michal Gulka***

*Kladno, February, 2017*

Ph.D. Programme: Biomedical and Clinical Technology  
Branch of study: Biomedical and Clinical Technology

**Supervisor: prof. RNDr. Miloš Nesládek, CSc., HDR**  
**Supervisor-Specialist: Mgr. Zdeněk Remeš, Ph.D**



The work was produced in the full-time Ph.D. study at the Department of Biomedical Technology of the Faculty of Biomedical Engineering of the CTU in Prague, together with Universiteit Hasselt in bilateral cooperation.

**Candidate:** Ing. Michal Gulka  
CTU in Prague, FBME  
Nám. Sítná 3105, 272 01 Kladno, Czech Republic  
and Universiteit Hasselt, Belgium  
Martelarenlaan 42, B-3500 Hasselt, Belgium

**Supervisor:** Prof. RNDr. Miloš Nesládek, CSc, HDR  
IMEC, Institute for Materials Research, University Hasselt  
Wetenschapspark 1, B-3590 Diepenbeek, Belgium

**Co-supervisor:** Mgr. Zdeněk Remeš, Ph.D.  
Institute of Physics CAS, v. v. i.  
Cukrovarnická 10/112, Prague 6



Hereby I declare that this Thesis has been written by me in its entirety as the result of my own original research. I have acknowledged all the sources of information which have been used in the Thesis in compliance with the Methodological Instruction No. 1/2009 - On maintaining ethical principles when working on a university final project.

Prohlašuji, že jsem tuto Doktorskou práci vypracoval samostatně na základě vlastního výzkumu a že jsem uvedl veškeré použité informační zdroje v souladu s Metodickým pokynem č. 1/2009 o dodržování etických principů při přípravě vysokoškolských závěrečných prací.

.....  
Michal Gulka

28. 2. 2017

## ANNOTATION

Recent developments of engineered nitrogen-vacancy (NV) centres in diamond hold great promise for novel sensitive nanoscale probes that can be used for quantum measurements and for diagnostics in nanomedicine. The aim of this work is to enable these sensing applications by studying NV photo-physics and by investigating NV detection sensing schemes. In this research we include both: fluorescent nanodiamond particles (NDs) and NV-containing single crystal diamond. We first study the fabrication processes of NDs, such as particle irradiation and surface termination with Fluorine, enabling for more homogeneous formation of NV centers in NDs and stabilization of NV charge by fluorination. Second part of the NDs' research focuses on in-cell application. We demonstrate a novel method of visualising NDs simultaneously with cell nucleus using Raman imaging and we observe the internalization rates of NDs by following the mechanical changes of cell membrane with the means of atomic force spectroscopy. In single crystal diamond we focus more on the novel photocurrent method of NV spin readout, which we develop with aim of future quantum sensing applications. Our photoelectric readout demonstrates higher detection rates than commonly used optical methods. We show that this technique is compatible with pulsed coherent NV spin manipulation and readout, demonstrating thus perspectives for progressing towards compact and scalable single spin quantum chip device.

## ANOTACE

Nedávný progres v oblasti dusík-vakance center (NV) v diamantu otevírá nové možnosti pro realizace citlivých nano-sond pro aplikace v kvantové detekci či nano-medicinské diagnostice. Tato práce se zabývá foto-fyzikálními vlastnostmi NV center a možnostmi jejich detekce, s cílem umožnit a posunout dále vývoj senzorických aplikací na bázi NV center. K tomuto účelu jsou použité jak fluorescenční nanodiamanty (ND), tak monokrystalický diamant. První část práce se zabývá ND. Je zkoumán proces přípravy svítivých ND, konkrétně procesu iradiace a povrchové úpravy, s výsledkem zlepšení homogenity připravených ND a stabilizace NV náboje díky terminaci částic Fluorem. Následně jsou ND dopraveny do buněk, kde je detekován jejich proces internalizace. K tomu je využita jak nově vyvinutá metoda Ramanovy mikroskopie, která umožňuje současnou detekci NV center a buněčných jader, tak spektroskopie atomárních sil, kde jsou sledovány mechanické změny buněčné membrány. Druhá část práce se věnuje nové fotoproudové metodě pro detekci NV spinů v monokrystalickém diamantu, kterou jsme vyvinuli pro budoucí kvantové senzorické aplikace.

Naše fotoelektrická metoda dosahuje vyšší intenzity detekce v porovnání se standardně používanými optickými metodami. Možnost koherentní pulzní manipulace a detekce spinů pomocí této metody je demonstrována, což je nezbytný prvek pro výrobu kompaktních senzorů na bázi kvantových jedno-spinových čipů.

## PREFACE

This thesis is a result of four-year doctoral program: Biomedical and Clinical Technology at Faculty of Biomedical Engineering of Czech Technical University and two-year Czech-Flemish bilateral project BOF15BL08 with Hasselt University, Belgium. Part of the work dealing with nanodiamond particles was carried out at Institute of Physics CAS, Institute of Organic Chemistry and Biochemistry CAS and at Laboratoire Charles Coulomb, Université de Montpellier. Photoelectric measurements were performed at Institute for Materials Research (IMO), Hasselt University. During my studies I have encountered many brilliant people, who helped me during my research in one way or another. I would like to take this opportunity to thank them all for making my PhD experience smooth-running and enjoyable.

My greatest and most sincere gratitude undoubtedly goes to my supervisor Miloš Nesládek. I cannot thank him enough for all the given opportunities, trust, support and for his enthusiasm and motivation. Most of all, I would like to thank him for all the time he devoted, even during weekends, to answering all my questions, correcting papers, planning further work and overall for his caring guidance during my whole study. Even at his busiest he always found a time to help me with my projects, which I deeply appreciate. I would also like to thank my co-supervisor Zdeněk Remeš for valuable advices and explanations and for his help on the development of the optical setup.

My warm thanks go to my friends and colleagues Vladimíra Petráková and Václav Petrák for the introduction to the nano-field and for all their help and consultations. I have enjoyed all the common activities, projects and summer schools. My thanks go also to all of my other colleagues and friends at FBME.

I would also like to express thanks to all my colleagues from Institute of Physics, especially to Andrew Taylor for consultations, help in the lab and all the support; to Marie Krečmarová, Vincent Mortet and Petr Ashcheulov for the discussions; and to Ivan Gregora for his help with Raman measurements.

Big thanks goes to my tutor, colleague and friend Emilie Bourgeois. I value all the physic discussions we had and the time we spent together in the lab. Her working determination is inspirational to me. I would also like to thank the other colleagues from IMO; Jaroslav Hrubý for the software development, Takashi Yamamoto for the advices and motivation and Johny Baccus for quick manufacture of the setup components and for his ability to always find a working solution.

My special thanks goes to Csilla Gergely for the opportunity to work in her group at Laboratoire Charles Coulomb, for the kind and friendly care and for making my stays in Montpellier pleasant and productive. Further, I would like to thank: Hamideh Salehi for help with Raman imaging, cell preparation and for showing me around; Marta Martin for the AFM measurements and for the assistance in the lab; Bela Varga for his help on my project during my stay and after my leave; Frederic Cuisinier for his friendly welcome and aid with the TEM image analysis; Thierry Cloitre for the help with luminescent experiments and Elodie Middendorp for the introduction to the Bio-lab and cell growing.

It is my great pleasure to thank Petr Cigler and all the people in his NanoChem group at Institute of Organic Chemistry. His expertise, critical thinking and advices were highly beneficial to me and I am really thankful for the collaborations. I would like to acknowledge Jan Havlík for preparation of the nanodiamonds, Helena Raabová for help with Raman and DLS measurements and Jitka Neburková for help with the peptide functionalization.

Further, I would like to thank Michael Trupke (TU Wien) for his explanations and help with pulsed ODMR measurements, Philip R. Hemmer (Texas A&M University) for the aid with the Ramsey PDMR experiments. Great thanks to Dominik Rohner (University of Basel) and David Broadway (University of Melbourne) for their discussions about NV photo-physics and science in general.

Lastly, but most importantly, I would like to thank my family and friends. I am lucky, that they were always there for me and greatly supported my studies. Special thanks to my parents, who always put my education in the first place and encourage me in my research, to my sister for proof-reading of the thesis and to my girlfriend for her patience with all my research stays abroad.

## OUTLINE

1.	MOTIVATION .....	1
2.	AIMS OF THE THESIS .....	4
3.	INTRODUCTION AND STATE OF THE ART.....	6
3.1.	Nanodiamond.....	6
3.1.1.	Properties .....	6
3.1.2.	Classification .....	6
3.1.3.	Synthesis .....	7
3.2.	Nitrogen-vacancy (NV) centre .....	8
3.2.1.	NV physical structure .....	8
3.2.2.	NV electronic structure.....	9
3.2.3.	Photoluminescence .....	13
3.2.4.	NV formation.....	14
3.2.5.	Hyperfine structure of NV <sup>-</sup> centre .....	16
3.2.6.	NV <sup>-</sup> spin properties .....	17
3.2.7.	NV <sup>-</sup> spin relaxation times .....	18
3.3.	Magnetic resonance of NV <sup>-</sup> centre .....	20
3.3.1.	Static EPR and ODMR .....	20
3.3.2.	Pulsed ODMR.....	21
3.4.	Sensing with NV <sup>-</sup> centre .....	25
3.4.1.	Magnetometry.....	25
3.4.2.	Opportunities and challenges for NV <sup>-</sup> centre.....	27
3.4.3.	Magnetic field sensing schemes .....	28
3.4.4.	Experimental realizations .....	30
3.4.5.	NMR and nano-MRI.....	34
3.4.6.	Summary.....	35
4.	RESULTS.....	36

4.1. Home-built setup for detection of NV related signals .....	38
4.2. Production of fluorescent nanodiamonds with a narrower emission intensity distribution	41
4.2.1. Abstract .....	41
4.2.2. Introduction .....	42
4.2.3. Methods and materials .....	44
4.2.4. Results and discussions .....	45
4.2.5. Conclusion .....	50
4.3. Benchtop Fluorination of Fluorescent Nanodiamonds on a Preparative Scale: Toward Unusually Hydrophilic Bright Particles .....	51
4.3.1. Abstract .....	51
4.3.2. Introduction .....	52
4.3.3. Methods and materials .....	53
4.3.4. Results and discussions .....	56
4.3.5. Conclusion .....	63
4.4. Label free visualization of near-IR probes in cells using Raman imaging .....	65
4.4.1. Abstract .....	65
4.4.2. Introduction .....	65
4.4.3. Methods and materials .....	66
4.4.4. Results and discussions .....	67
4.4.5. Conclusion .....	71
4.5. AFM study of diamond particles internalization by monitoring the cell membrane stiffness changes .....	73
4.5.1. Abstract .....	73
4.5.2. Introduction .....	73
4.5.3. Methods and materials .....	74
4.5.4. Results and discussions .....	75
4.5.5. Conclusion and future work .....	78

4.6. Photoelectric detection of electron spin resonance of nitrogen-vacancy centres in diamond	79
4.6.1. Abstract.....	79
4.6.2. Introduction.....	80
4.6.3. Methods and materials .....	81
4.6.4. Results and discussion .....	83
4.6.5. Conclusion .....	91
4.7. Enhanced dual-beam excitation photoelectric detection of NV magnetic resonances in diamond .....	92
4.7.1. Abstract.....	92
4.7.2. Introduction.....	92
4.7.3. Methods and materials .....	94
4.7.4. Results and discussions.....	94
4.7.5. Conclusion .....	99
4.8. Pulsed photoelectric coherent manipulation and detection of NV centre spins in diamond	100
4.8.1. Abstract.....	100
4.8.2. Introduction.....	100
4.8.3. Methods and materials .....	101
4.8.4. Results and discussions.....	102
4.8.5. Conclusion .....	109
5. SUMMARY AND FUTURE PERSPECTIVES .....	110
5.1. Development of confocal setup .....	111
5.2. Nanodiamond particles .....	112
5.3. Single crystal diamond .....	114
6. OUTLOOK FOR THE BIOMEDICAL ENGINEERING.....	116
7. LIST OF AUTHOR'S PUBLICATIONS AND SELECT.ED PRESENTATIONS	125

7.1. Publications .....	125
7.2. First-author presentations .....	126
Reference .....	129

# 1. MOTIVATION

Nanoscience and nanotechnology have been growing rapidly within the past 30 years. It is thanks to the right tools, such as the scanning tunneling microscope (STM) or the atomic force microscope (AFM), which enabled to perceive the nano-world. It has been found, that at the atomic, molecular and macromolecular scale, properties of well-known materials significantly differ from those at a large scale (1). This happens, alongside other things, thanks to the much greater surface-to-size ratio in comparison with larger-scale materials, meaning that more surface is available for interactions with surroundings, and also due to the quantization in very small objects. The nano-techniques are prominent because the nanoscale interactions combine new concepts and ideas of modern technology.

The resolution of imaging instruments, by which scientists collect information about the ongoing biological processes, may substantially change our understanding of biological world. The recent development of ultra-high precision optical resolution techniques has given rise to nanoscale quantum imaging methods, as a tool for reaching increasingly smaller scales and ultimately single molecules without need of averaging. Such probes can be based on quantum sensors. One of the example of the quantum sensor is a so-called nitrogen-vacancy (NV) centre in diamond with both electron spin and photoluminescence properties that can be used for the sensing. These atomistic probes allow to reach the resolution comparable to dimensions of electron orbits and are anticipated to bring a groundbreaking understanding of life cycle processes, including applications in medicine, such as real-time monitoring of disease initiation. These nanoscale sensors can be used as non-perturbing probes for sensing nanoscale magnetic or electric fields related to the interaction of a probe with spin-carrying moieties (radicals, paramagnetic ions) present in chemical or biological environment. Some of these quantum sensors have been already demonstrated in the past, such as ensembles of cold atoms or SQUIDS. These systems, however, require specific working conditions, such as cryogenic temperatures or ultra-high vacuum, and have limited spatial resolution.

Recent developments of engineering's NV centres in diamond have opened the way towards the use of nanodiamond as a novel sensitive nanoscale probe that can be used for quantum measurements and for diagnostics in medicine. NV centre is a defect in the diamond lattice where two adjacent carbon atoms are replaced by nitrogen and a lattice vacancy. One of the most striking properties of the NV centre is the fact that the electron transitions among NV

electron spin states can be influenced even by very weak external electric or magnetic fields (those emerge upon the interaction with biological and chemical environment). This allows the optical detection of electromagnetic fields (charge, spin) that interact with a single NV centre electron spin at room temperature. The transitions between the NV states can be monitored by electron spin resonance techniques. Due to differences in photoluminescence intensity of radiative transitions on the electron spin triplet with spins  $m_s=0$  and  $m_s=\pm 1$ , these transitions can be directly optically monitored by a technique called optically detected magnetic resonance (ODMR). Since the electrons can be promoted from  $m_s = 0$  to  $m_s = \pm 1$  by using microwave (MW) excitation at resonance frequency ( $\sim 2.87$  GHz zero-field splitting) and due to the Zeeman splitting of the degenerate  $m_s = \pm 1$  states, this system can be used to detect very weak magnetic field in order of nT or lower (2). By measuring dynamic properties of the spins such as  $T_1$ ,  $T_2$ ,  $T_2^*$  relaxation times or by using phase coherent pulse protocols, one can monitor on a very short time scale the temporary changes of the NV centre spin environment. This makes the solid-state sensors based on the NV centres in diamond a system of a leading interest for atomistic imaging and biomolecular sensing.

Another useful feature of NV nanodiamond is its strong and stable photoluminescence. Fluorescent nanodiamonds are becoming an increasingly attractive tool for biological cellular imaging (3). Though there are plenty of markers available including simple fluorescent dyes, voltage sensitive dyes (VSD) or quantum dots, the drawbacks of these markers are either photobleaching, biotoxicity or their influence on ongoing biochemical processes. The fluorescent nanodiamonds overcome these disadvantages as they are biocompatible and possess non-blinking and non-bleaching luminescence even for particles of  $\sim 5$  nm in size. The size range is also important for biomedical applications and it is, for example, different for endosomatic penetration of particles through cellular membrane and for a penetration of particles to cell nucleus for which are these ultra-small nanodiamonds required. Fluorescent nanodiamonds can also act as a bimolecular probe as their luminescence spectrum can be changed upon surface interactions with different atoms or molecules dropped on the surface or bound to it. This can be used for remote monitoring of chemical processes in biological environments based on color changes from photoluminescence (4). It has been previously shown by our group that one can detect the change of pH of ND environment (5) or that NDs can be used as a platform for DNA delivery with monitored release (6). Both methods use only a simple optical excitation of NVs together with spectral detection. The probed information is

encoded in the color change of NV luminescence (due to the charge switching between NV's negative and neutral state with different spectral properties).

## 2. AIMS OF THE THESIS

The aim of this work is to develop fluorescent nanodiamond probes and techniques towards photoelectrical detection of NV centres in diamonds. This would include the mastering of the physical principles and manipulation with photon or spin centres in such way, that they could react to the external optical and microwave fields. To be able to read specific signals of NV centres, the optical confocal setup is rebuilt to enable pulsed excitation and readout of NV and is enhanced by the methods of ODMR for sensing application. The rest of the thesis can be divided in two main parts.

The first part is dealing with further development and improvement of **luminescent nanodiamond (ND) particles** for the purpose of intracellular probing and drug delivery. To further enhance and stabilize luminescence properties of these probes, the thesis addresses the preparation procedures of NDs. Recently, it was shown that by optimal annealing conditions and proper oxidation, one can produce NDs with ten-fold higher luminescence intensity (7). Building on this result, here the irradiation conditions are studied with aim to produce more homogeneously irradiated particles. The goal is to develop method of fluorescent nanodiamonds fabrication that will permit creating exactly one NV centre per ND with a high yield, which is essential for magnetic field sensing relying on the optical detection of electron spin resonance of  $NV^-$  color centre. To further stabilize the  $NV^-$  luminescence, possibility to create fluorinated surfaces is studied and results are compared to the commonly use oxidation methods. Finally, the detection methods of NV diamond are tested in various biological environment and the nanodiamond faith in cells is studied. The aim is to develop a method of visualization and localization of NDs in the non-fixed cells without the use of additional labels. Further, using AFM force spectroscopy cell-membrane behavior upon NDs uptake is examined for any observable changes in Young's modulus (stiffness) of the membrane, with the goal to obtain a novel non-optical way to sense NDs uptake rates in cells.

In the second part, the detection properties of **NVs in single crystals** (both in bulk and close to the diamond surface) are studied. The main goal is to develop a new method based on photocurrent readout of the spin states and develop coherent spin protocols that are used for quantum sensing. The objective is the enhancement of the detection rates of spin state readout of negatively charged NV centre to obtain high sensitivity, high signal-to-noise ratio, and increased resolution. This is very important for many NV applications including quantum

sensing or magnetometry, where the detection of weak magnetic fields originating e.g. from the targeted spins is realized by appropriate manipulation of the spins to affect the precession phase accumulation of the highly coherent NV electronic spin (8). Current methods for readout of NVs rely on optical detection (i.e. ODMR) and the detection rates are thus limited by the photon collection efficiency. Here, direct monitoring of the spin-preserving electron transitions through measurement of NV related photocurrent is studied, reaching higher detection rates thanks to the efficient electron readout and photoelectric gain. Establishing photoelectric detection brings additional advantages such as easier integration on chip (which is of big value to quantum information applications) and possibility for more compact sensing device (which can be useful for magnetometry). The applicability of photoelectric method for quantum measurements, where coherent spin manipulation and readout is necessary, is tested and comparison to ODMR is discussed.

### 3. INTRODUCTION AND STATE OF THE ART

#### 3.1. Nanodiamond

##### 3.1.1. Properties

Diamond, allotrope of carbon, is known to be an outstanding and unique material. Its crystal structure is one of the closest packed lattice (face-centered cubic) with  $sp^3$  covalent bond, making diamond extremely hard and chemically inert. It is optically transparent, possesses high index of refraction, is excellent thermal conductor, and is wide-bandgap semiconductor. Moreover, diamond is a biocompatible and non-toxic material which makes it a suitable candidate for various biomedical applications. Nanodiamonds are crystalline fractions of diamond with dominantly  $sp^3$  bonded carbon structure of size  $\sim 1\text{--}100$  nm in the form of diamond films, diamond particles, 1D diamond rods and 2D diamond nanoplatelets. At nanoscale, diamond preserves most of its outstanding properties (9).

##### 3.1.2. Classification

Ordinary bulk diamond hosts wide variety of crystallographic defects and color centres. Most common impurity is nitrogen or boron that replace the carbon in diamond lattice. Depending on the number and the type of impurities present in the lattice, diamonds are classified into several groups. Primary classification divides diamonds into two groups: type I with high nitrogen concentration and type II with very low nitrogen concentration (less than 1 ppm (10)). Type I is further divided into Ia, which is more common in nature and contains nitrogen in form of aggregates (IaA for “A” aggregate form and IaB for “B” aggregate form), and Ib, which contains isolated substitutional nitrogen (11). Type II is divided into pure IIa diamond with undetectable defect concentration and p-type semiconductor IIb diamond with boron as a major impurity (12). Schematic configuration of different diamond types is shown in Figure 1.

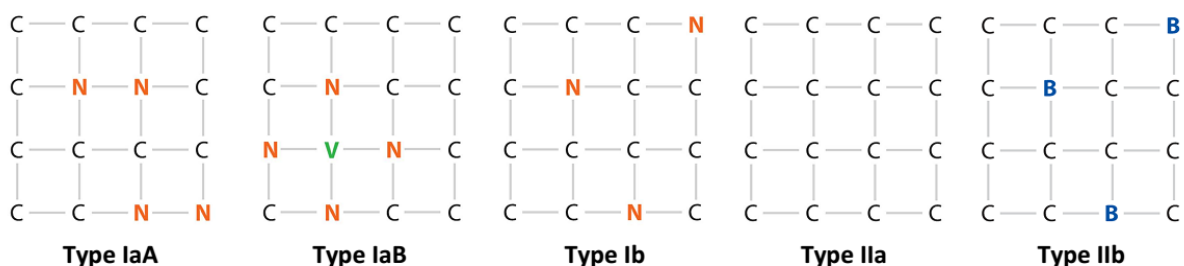


Figure 1: The schematic configurations of impurities in diamond lattice according to classification types (V stands for vacancy) (13).

### 3.1.3. Synthesis

Nowadays, there are many methods of nanodiamond production. Synthetization has been reported by laser ablation, autoclave synthesis from supercritical fluids, chlorination of carbides, ion irradiation of graphite or electron irradiation of carbon ‘onions’, ultrasound cavitation (14), yet there are three main processes known and widely used today to synthesize artificial diamonds: high-pressure high-temperature method (HPHT), chemical vapour deposition (CVD) and detonation.

#### **HPHT synthesis**

This method is inspired by actual geological processes involved in the formation of natural diamonds. A source material (carbon-rich melt) is subjected to high pressure (above 5 GPa) and high temperature (above 1500 °C), inducing the phase transition of graphite to diamond. Usually, metal solvents are used during this process, for the reason they act as catalytic materials and lower the energy needed to form the diamond (15). This, however, limits the purity and leads to creation of Ib diamond with nitrogen concentration typically up to 300 ppm in the form of grain (10).

#### **CVD synthesis**

Growth of the nanodiamond using CVD process does not take place in conditions, in which diamond is thermodynamically stable. It is therefore often called metastable synthesis, where the deposition of carbon is rather driven by kinetics than by thermodynamics. CVD diamond is formed in a growth deposition chamber heated up to temperatures above 800 °C (16). Feed gas, typically mixture of methane (CH<sub>4</sub>) and hydrogen (H<sub>2</sub>), is injected into the chamber and serves as a precursor. Methane is then decomposed in the chamber and thin diamond layer grows in an atom-by-atom, layer-by-layer process (17). The diamonds produced in this method can be easily grown with selected impurities such as nitrogen or boron and then milled down to create nanoparticles. CVD method is mainly used to coat large areas of monocrystalline diamond, and CVD diamonds are the main source of ultrapure diamond (type IIa) (18).

#### **Detonation synthesis**

Another way to synthesize diamonds is by detonation. Diamond crystals, nominally a few nanometres in size (typically around 5 nm (19)), originate from the detonation of carbon-containing explosives in a metal chamber. Variety of carbon sources can be used within the

explosive precursor. Most common is popular military explosive made out of 40% trinitrotoluene (TNT) and 60% hexogen (RDX). The explosion is surrounded by a non-oxidizing cooling media of either gas (N<sub>2</sub>, CO<sub>2</sub>, Ar etc.) or water (ice), so-called “dry” or “wet” synthesis, respectively (20). Explosion creates appropriate conditions for the thermodynamic stability of diamond, which is of high pressure (~ 20–30 GPa) and high temperature (~ 3000–4000 K) (9). Due to the fact, that the reaction continues even after the temperature and pressure drops, created nanodiamond powder contains significant amount of contamination, as the particles are covered in graphitic shell and surrounded by soot. To obtain pure and individual particles, thorough subsequent purification and de-aggregation processes are needed (21).

## 3.2. Nitrogen-vacancy (NV) centre

### 3.2.1. NV physical structure

Among all of the different color centres that exist in diamond lattice, VN<sub>1</sub> structure (generally addressed as nitrogen-vacancy or NV centre) is probably the most studied. It consists of substitutional nitrogen atom (N) adjacent to a vacant lattice site (V). It forms C<sub>3v</sub> symmetry so the defect’s symmetry axis may be oriented along one of the four possible crystallographic directions. These four NV orientations are usually almost equally populated, however some preferential NV orientation has been observed in CVD diamond with in-grown NVs (22).

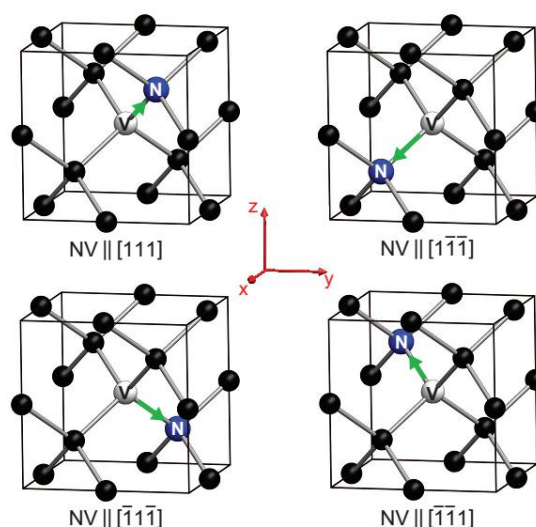


*Figure 2: Four orientations of the NV centre in diamond. Carbon atoms are depicted in black, nitrogen (N) atoms in blue, and vacancies (V) in white. The NV electronic spin is indicated by green arrows. Four additional orientations are possible by flipping the nitrogen atoms and vacancies in each configuration above; however, orientations with equivalent symmetry axes are spectrally indistinguishable and may therefore be considered in the same NV orientation class. Taken from (23).*

NV centres have two possible charge states; the neutral  $NV^0$  and negative  $NV^-$ . However, it is believed that third type of NV centre exists; positive  $NV^+$  (24). Nitrogen is bonded covalently to three neighboring carbons leaving two unbonded valence electrons, which create a lone pair. Another three electrons are present from three carbons surrounding vacancy and two of them form a pair together with nitrogen lone pair electrons, leaving one unpaired electron (25). Additional donor electron is present in  $NV^-$  centres, forming a spin  $S=1$  couple with one of the vacancy electrons (26). It is believed that this electron is gained from nearby N donor impurity (23). The ground state energy levels for  $NV^-$  and  $NV^0$  centre relative to the valence band top are 2,0 eV and 1,2 eV, respectively, as calculated from Schrödinger equation, and  $NV^-$  is located about 2 eV below the conduction band of ND (26). The NV charge state depends on the presence of nearby electron donors or acceptors (27) and one diamond sample can contain both neutral and negative NV state. NV centre is a stable defect, but photochromic switching between the two charge states has been observed. This photoconversion can be induced either by direct ionization of  $NV^-$  or indirectly, by the ionization of the substitutional nitrogen donors surrounding the NV centre in the crystal (28) (29).

### 3.2.2. NV electronic structure

The foundation of theoretical models for understanding the energy levels of NV centre comes from  $C_{3v}$  symmetry. Also, the properties of NV centre are determined by dangling electrons (immobilized free radicals) in orbitals of the carbon and nitrogen atoms neighbouring the vacancy (30) (31). Two approaches are possible: ab initio calculations and semi-empirical molecular model of deep-level defects in semiconductor (32) (33). Even though these two methods contradict in some matters, basic electronic structure of NV centres has been accorded by both and confirmed by electron paramagnetic resonance and optical studies.

#### **$NV^-$ centre:**

When modelling energy levels of  $NV^-$  centre, six electrons need to be taken into account. It is simpler, however, to interpret the  $NV^-$  centre as if it were a molecule. For such defect, possible configurations of many-electron states are  $^1A_1$ ,  $^3A_2$ ,  $^1E$  and  $^3E$  (25). The  $A_1$ ,  $A_2$  and  $E$  represent the type of symmetry and first upper digit represents the number of allowable  $m_s$  spin states (spin multiplicity ranging from  $-S$  to  $S$  with total  $2S + 1$  states, where  $S$  represents the highest spin value). The ground state of  $NV^-$  has been identified to be a spin-tripled with  $^3A_2$  symmetry, where the lower two states  $a_1(1)$  and  $a_1(2)$  are fully occupied and the degenerate  $e_x$  and  $e_y$  orbitals are populated by one unpaired electron each. Spin-spin interaction between these

unpaired electrons gives rise to axial zero-field splitting (ZFS) of the spin triplets separating spin states  $m_s = 0$  ( $|0\rangle$ ) and  $m_s = \pm 1$  ( $|\pm 1\rangle$ ) by  $D_{gs} \approx 2.87 \text{ GHz} \equiv 12 \mu\text{eV}$ . The corresponding excited state, resulting from promotion of the electron from the orbital  $a_1(2)$  to the orbital  $e_{x,y}$ , is spin-triplet  ${}^3E$  state with 1.945 eV (ZPL 637 nm) transition (see Figure 3) and axial ZFS of 1.42 GHz. A triplet state is an electronic state in which two electrons in different molecular orbitals have parallel spins, which is rare in molecules (34).

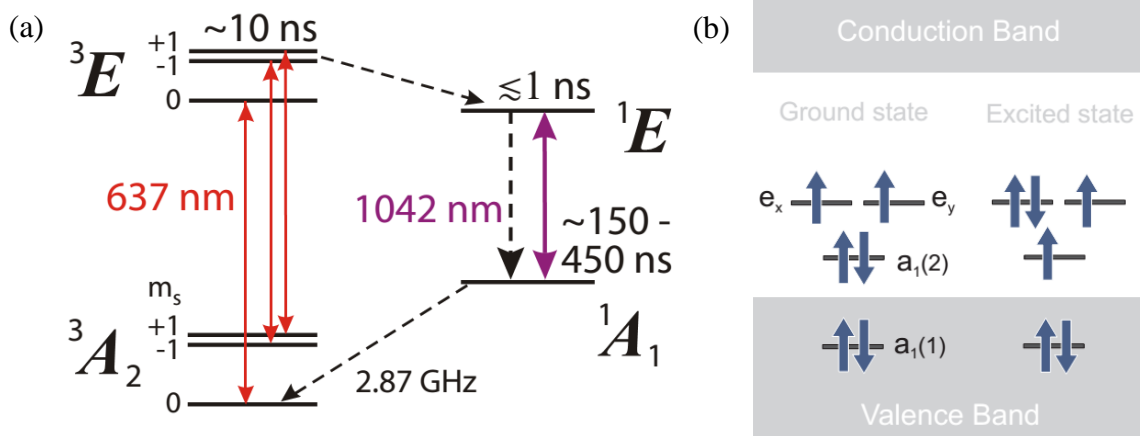


Figure 3: (a) Level diagram for the NV<sup>-</sup> centre showing spin-triplet ground and excited states, as well as the singlet system involved in intersystem crossing. Radiative transitions are indicated by solid arrows and non-radiative transitions by dashed arrows. (b) Electronic structure of the NV<sup>-</sup> ground and first excited state. (a) Taken from (35), (b) taken from (36).

The two possible transition dipoles (associated with the excitation of one electron from  $a_1(2)$  to either  $e_x$  or  $e_y$ ) are perpendicular to the NV axis and to each other. Therefore, an excitation with a laser beam parallel to the NV axis is the most efficient (36). Optical transitions from  ${}^3E$  excited state to  ${}^3A_2$  ground state are primarily spin conserving; there exists, however, a primarily non-radiative alternative decay path allowing the transfer of the spin population from the  $|\pm 1\rangle$  to the  $|0\rangle$  through the singlet states. This intersystem crossing (ISC) is possible when the magnetic field from orbital motion of the two electrons interacts with their spin magnetic moments, so there is certain degree of “spin-orbit coupling”. Experiments have shown that the singlet levels involved in the ISC include  ${}^1E$  and  ${}^1A_1$ , although the ordering of these levels is still under debate. Some of the models set the  ${}^1A_1$  symmetry as lower state and  ${}^1E$  as the upper state (37), some do it the other way around (31). However, the separation of the two levels is known to be 1042 nm (1,190 eV ZPL) (38). The energy spacing between the singlet and triplet states is yet unknown, but it is believed that lower singlet state is roughly  $\sim 0,7 \text{ eV}$  above the ground state (31).

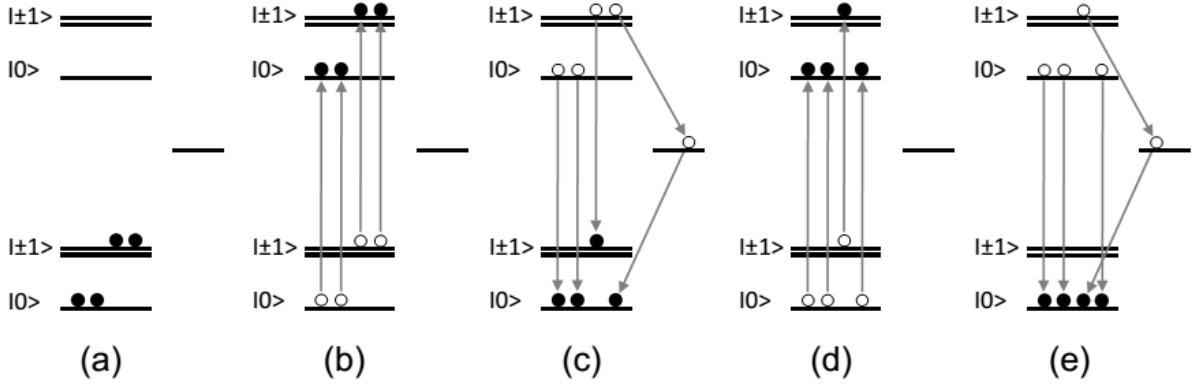


Figure 4: Schematic representation showing the mechanism of the  $NV^-$  polarization for the ensemble of the NV centres (notice, that the NV centre is a single photon source, so only one electron is excited at the time). (a) Initially, the  $NV^-$  population is evenly distributed between the ground spin sublevels  $m_s = 0$  and  $m_s = \pm 1$ . (b) Spin conserving transition of the electrons towards the excited states upon the green laser excitation. (c) The system relaxation; part of the population from the excited  $m_s = \pm 1$  spin sublevel relaxes non-radiatively, via the intermediate singlet level, towards the ground sublevel  $m_s = 0$ . (d) The following cycle. (e) After a few optical cycles, all the population ends up in the ground spin sublevel  $m_s = 0$  and the NV spin state is therefore initialized. Taken from (39).

The ground state has three allowable spin states split by crystal field into doublet degenerate ( $m_s = \pm 1$ ) and singlet ( $m_s = 0$ ) state. In thermal equilibrium at temperatures above  $\sim 1$  K, the ground state sublevels are nearly equally populated (40). Excitation from the  $m_s = 0$  sublevel is spin conserving and the system decays straight back while emitting red photon. Starting from  $m_s = \pm 1$  system is promoted to the  $m_s = \pm 1$  excited state and has 30% chance to decay, taking alternative path via ISC (41). System falls to the excited singlet state  $^1E$  and directly decays further to the  $^1A_1$  metastable state while emitting an infrared photon ( $\lambda = 1042$  nm). Afterwards, the system crosses over, predominantly to the  $m_s = 0$  sublevel of the  $^3A_2$  ground state (42). These spin-selective decay paths result in two important features of the NV centres. Firstly, it is possible to optically readout the spin value of the NV centre. Secondly, system can be optically pumped to  $m_s = 0$  ground state, enabling spin polarization which is very important for quantum information application, where a system initialization to a known quantum state is necessary. The process of optical polarization to  $m_s = 0$  ground state is depicted at Figure 4.

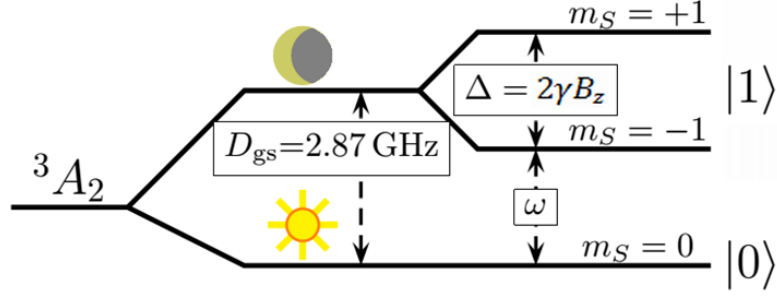


Figure 5: Scheme of the  ${}^3A_2$  ground state sublevels indicating the encoding of bright state  $|0\rangle$  and dark state  $|1\rangle$ . Taken from (43).

Often, the ground sublevels are encoded as bright state (for the  $m_s = 0$ ) and dark state (for the  $m_s = \pm 1$ ), considering their influence on the red NV fluorescence (see Figure 5). The occupation of these sublevels can be manipulated with microwave field. The zero-field splitting of the ground state ( $D_{gs}$  or  $D$ ) is equivalent to 2.87 GHz. At the resonant frequency, the population of  $m_s = 0$  and  $m_s = \pm 1$  is flipped. In the presence of a small axial magnetic field,  $B_z \ll D_{gs}/(g_s\mu_B)$ , the degenerate  $m_s = \pm 1$  levels are shifted by  $m_s g_s \mu_B B_z$  due to the **Zeeman effect** (where  $g_s$  is electron spin factor also called dimensionless magnetic moment;  $\mu_B$  is Bohr magneton – physical constant for expressing the magnetic moment of an electron caused by either its orbital or spin angular momentum). Total energy difference of Zeeman split ( $\Delta E_Z$ ) is then  $\Delta E_Z = 2g_s\mu_B B_z$ , often expressed in terms of frequency as  $\Delta = 2\gamma B_z$  (where  $\gamma$  is gyromagnetic ratio and it is equal to  $\gamma = g_s\mu_B/\hbar = 2,80 \text{ MHz/G}$ , where the  $\hbar$  is reduced Planck constant) (35).

### NV<sup>0</sup> centre:

NV<sup>0</sup> centre consists of 5 electrons but the exact structure is not yet determined. The EPR signal was for a long time undetectable due to the Jahn-Teller effect (dynamic coupling that broadens the EPR line dramatically. See (25) for more details). The current model (see Figure 6) sets the  ${}^2E$  doublet state ( $S = 1/2$ ) as a ground state. The symmetry of the excited doublet state is possibly  ${}^2A_1$  or  ${}^2A_2$  with the ZPL transition of 2,156 eV (corresponding to the 575 nm luminescence). The metastable spin quartet state was observed by the EPR and it is believed to be of  ${}^4A_2$  symmetry (31). Since NV<sup>0</sup> does not possess such qualities as the NV<sup>-</sup> (e.g. its electronic spin cannot be prepared and read out optically), more focus lies on the negative charged NV<sup>-</sup>, which is studied far more.

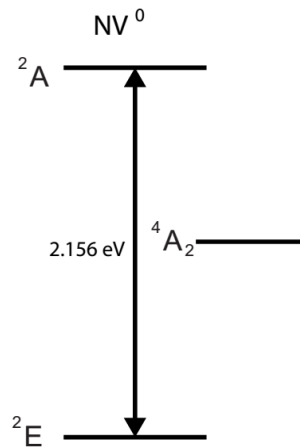


Figure 6: Schematics of the known aspects of the NV<sup>0</sup> electronic structure. The energy of the observed ZPL is indicated. Taken from (44).

### 3.2.3. Photoluminescence

Nanodiamond particles with incorporated NVs have been shown as an excellent luminescent marker for microscopy. Recently, Stephan Hell received Nobel Prize in Chemistry (2014) for the development of super-resolved fluorescence microscopy named STED (Stimulated Emission Depletion microscopy). He was carrying part of his work using NV nanodiamond as a fluorescent marker (see (45)). NV centres exhibit strong and stable photoluminescence even for particles as small as 5 nm with no photo-bleaching or photo-blinking (46). Together with good biocompatibility, not-toxicity and luminescence that has small absorption in tissue and differs from cell's auto-fluorescence ND particles are perfect candidates for bioimaging and intracellular sensing.

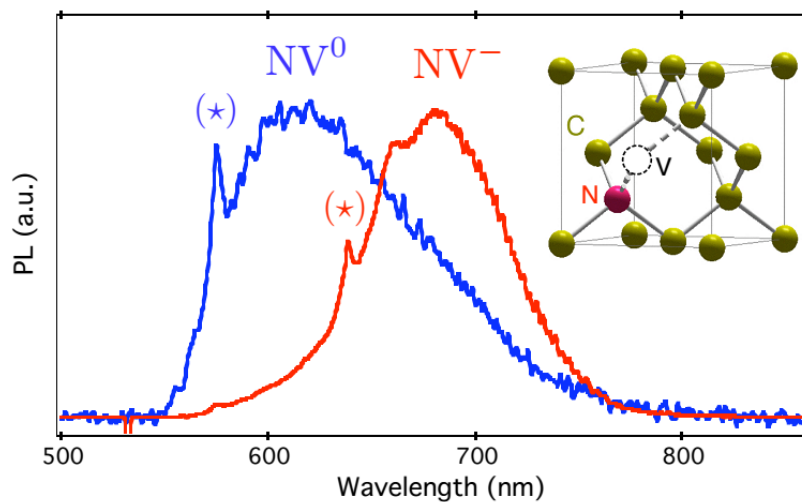


Figure 7: Photoluminescence from single NV<sup>0</sup> (blue) and NV<sup>-</sup> (red) centre in nanodiamonds. ZPLs of 575 nm and 637 nm are marked with asterisk. The inset shows atomic structure of NV. Taken from (47).

The fluorescence spectrum coming from NV centres (see Figure 7) is broad (superposition of  $NV^-$  and  $NV^0$ ), ranging from 550 nm to 800 nm, peaking around 690 nm. The excitation band is in a spectral range of 480–580 nm (48). The  $NV^-$  has a strong optical transition with a zero phonon line (ZPL) at 637 (corresponding to electronic transition between the excited and ground state 1.945 eV) with a broad red-shifted phonon sideband (PSB) of 640–800 nm. Broad PSB can be explained by Franck-Condon principle (see Figure 8): changes of the electronic states induced by optical transition vary the inter-atomic distances and therefore excite lattice vibrations (phonons). As confirmed by ab initio calculations, the ground and excited states have significantly different coordinates, therefore only 4% of the photons are emitted to the ZPL (36). Remaining photons relax into PSB. Similarly,  $NV^0$  emits with ZPL at 575 nm (2.156 eV) with  $\sim 50$  nm red-shifted sideband. This strong phonon broadening allows an efficient optical off-resonant excitation of the NVs.

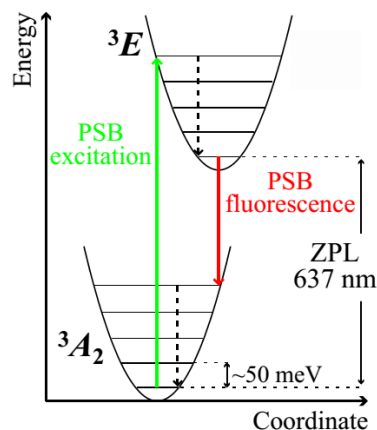


Figure 8: Schematic illustration of the Franck-Condon principle for excitation and fluorescence of the main optical transition of NV centre. Non-radiative decay is shown with dashed lines. Phonons play an important role in both the optical transitions and spin dynamics of the NV. In thermal equilibrium at room temperature, about 90% of NV centres will be in the lowest vibrational level, corresponding to an effective (there are no clearly discrete levels) vibrational spacing of  $\sim 50$  meV. The most probable vertical transitions are to the turning point in the  ${}^3E$  harmonic well, which corresponds to about 4 vibrational quanta ( $\sim 0.2$  eV), resulting in the broad peak (PSB – phonon sideband) in the absorption spectrum as well as in emission spectrum. Taken from (35).

#### 3.2.4. NV formation

Different techniques can be employed to ensure that NV centres are formed in diamond, depending on the aim, which can be obtaining the highest concentration of NVs, precise positioning of the defect formation or isolation of single NV. The most common approaches include irradiation or ion implantation with subsequent annealing and incorporation of NVs during CVD growth.

### Irradiation:

Irradiation of Ib diamond is the most straightforward and commonly used method for nanodiamond particles. HPHT Ib diamond is commercially available and already contains isolated substitutional nitrogen. To create vacancies, focused beam of ions or electrons accelerated to high energy (KeV, MeV) is used to bombard the crystalline structure. The diamond is then exposed to subsequent annealing process at temperatures higher than 600 °C. The annealing enhances the migration of the vacancies, which become trapped by nitrogen, forming stable NV centres (see Figure 9). Commonly used annealing parameters for creation of NVs in diamond are in the range of 700–800 °C for 1–2 hours (3). Recently, our group published article in high impact journal *Nanoscale*, identifying a discrete maximum of NV number for diamond particles annealed at 900 °C for 1 hour (J. Havlík, M. Gulka, M. Nesládek et al. in *Nanoscale*, 2012).

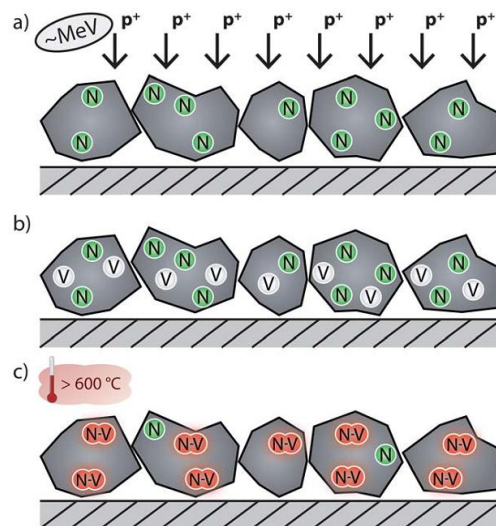


Figure 9: Creation of NV centres by irradiation technique; (a) bombardment by high energy ions, (b) creation of vacancies and (c) formation of NV centres by thermal annealing. N stands for nitrogen atom and V for vacancy. Taken from (7).

### Ion implantation:

To produce the NV centres in type IIa pure diamond, irradiation with nitrogen ( $N^+$ ) ions is used to create both nitrogen impurities and vacancies. The following process is then the same as in the previous technique; annealing at high temperature causes formation of NVs. The major strengths of this technique are the ability to localize the NV centre in the sample (49) and the deterministic implantation. Unfortunately, two main drawbacks of this method are the

stochastic nature of ion beam (that causes some parts of the sample to contain more than one NV centre, while others contain none) and unsubstantial control of the ion beam spot size (50).

### **CVD growth:**

Nitrogen impurities may be incorporated into the diamond during CVD synthesis by addition of nitrogen (N<sub>2</sub>) into the feed gas. The inclusion of NV centres and nitrogen in the diamond lattice occurs spontaneously during the growth of the crystals when nitrogen is present. The concentration of NV defects that are incorporated into the diamond is determined by a combination of growth conditions: amount of nitrogen gas introduced into the growth chamber, substrate temperature, chamber pressure, etc. and these are being still exerted (51) (52). The N-rich CVD diamond can be further irradiated and annealed to produce higher concentration of NV centres.

#### 3.2.5. Hyperfine structure of NV<sup>-</sup> centre

Fine structure is possible to resolve at NV<sup>-</sup> ground state level, due to the Fermi contact hyperfine interactions between the NV electronic spin and the nuclear spin of the N in NV complex. This splitting can be visualized by EPR when low laser intensity and low microwave power is applied (see chapter 3.33.2.6). In natural abundance, nitrogen is composed of 99.6% of <sup>14</sup>N with nuclear spin  $I = 1$ , and 0.4% of <sup>15</sup>N with spin  $I = \frac{1}{2}$  (53). Therefore, the coupling to <sup>15</sup>N is often neglected. The splitting due to the <sup>14</sup>N gives rise to three separate levels (for both  $m_s = 0$  and degenerate  $m_s = \pm 1$  sublevels) with nuclear magnetic quantum numbers  $m_I$  of -1, 0 and +1 (coming from  $I = 1$ ). However, for single NV centre, only six transitions are allowed, as it is shown in Figure 10a.

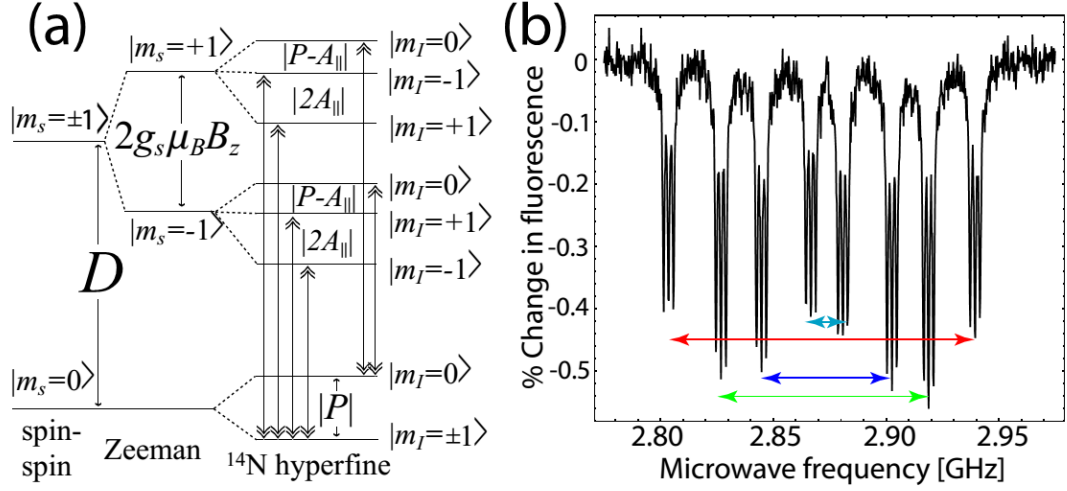


Figure 10: (a) Ground state level structure of the NV centre under a small axial magnetic field. Allowed magnetic dipole transitions are shown with double-headed arrows. (b) Optically Detected Magnetic Resonance (ODMR) spectrum (excited at 532 nm) for a low-defect-density CVD diamond. The 24 separate resonances correspond to two different  $|\Delta m_s| = 1$  transitions, four different NV orientations, and three different  $^{14}\text{N}$   $m_I$  levels. Taken from (37).

There are four possible ways for NV centre orientation within the lattice and since even the small magnetic field on the N-V axis affects the transition frequency, there are four shifted copies of the single spectrum (54). For magnetic field orientation along the [100] crystal direction,  $B_z$  is the same for all four possible orientations of NV. However, for most field  $B_z$  orientation, this is not the case and there are all together 24 different resonances (4 NV orientations, 2  $m_s$  spin states and 3 nuclear magnetic quantum numbers) as shown in Figure 10b. This feature enables diamond sensor to act as a **vector magnetometer** measuring both magnitude and direction of an external magnetic field (55).

### 3.2.6. $\text{NV}^-$ spin properties

As described above,  $\text{NV}^-$  ground state is a spin triplet without spin-orbit interaction, so the electron spin is mainly influenced by spin-spin and Zeeman interactions. When disregarding nuclear Zeeman interaction and the nuclear quadrupole interaction (which are negligible in the experiments discussed in this thesis), the spin Hamiltonian of  $\text{NV}^-$  centre can be written as (56):

$$\hat{H} = \hat{H}_{ZFS} + \hat{H}_{ZS} + \hat{H}_{HF} \quad (3.1)$$

The first term in this equation  $\hat{H}_{ZFS}$  corresponds to zero field splitting (ZFS) from the spin–spin interactions of the two unpaired electrons. ZFS occurs only for the non-spherical spin densities. For NV<sup>-</sup> centre, the main deviation from spherical symmetry takes place along NV axis and therefore influences mainly the axial component of the spin. The transversal components of the spin are only affected when the axial symmetry is broken by transversal strain or electric field. Values of transversal ZFS parameter E are in the kHz-MHz range, thus much lower comparing to axial ZFS ( $D_{gs} \approx 2.87$  GHz).

Second term  $\hat{H}_{Zs}$  describes Zeeman interaction of the electron spin with the external magnetic field. For magnetic fields parallel with the NV axis, the interaction causes a linear splitting of the  $m_s = \pm 1$  states by  $\sim 56$  MHz/mT. When the magnitude of the magnetic field is equal to roughly 102 mT, a level anti-crossing (LAC) occurs as the ZFS is compensated by the Zeeman shift, resulting in mixing of energy levels (57). For misaligned magnetic fields, the shift of  $m_s = \pm 1$  states is not linear and depends on the angle between the magnetic field and NV axis (see Figure 11).

Last term,  $\hat{H}_{HF}$ , accounts for hyperfine interactions between electron spin and nitrogen nuclear spin explained in previous chapter. Since the NV lattice is predominantly composed of the spineless carbon isotope <sup>12</sup>C, hyperfine coupling to other nuclei can be neglected.

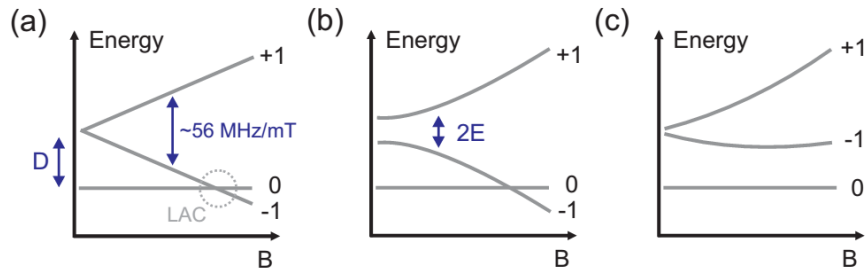


Figure 11: Ground state spin levels of NV<sup>-</sup> centre for various fields: (a) magnetic field B parallel to NV axis and E = 0, (b) B parallel to NV axis and E ≠ 0, (c) B not parallel to NV axis. Taken from (36).

### 3.2.7. NV<sup>-</sup> spin relaxation times

The Hamiltonian equation (3.1) given in previous chapter does not account for dynamic changes related to the interactions with NV environment, such as the lattice vibrations or magnetic and electric field noise. These effects cause relaxation of polarization and coherence

of the spin system and are characterized mainly by two important time scales, the longitudinal ( $T_1$ ) and transverse ( $T_2, T_2^*$ ) relaxation time.

### **Longitudinal relaxation time - $T_1$**

The  $NV^-$  spin may interact with phonon lattice, resulting in change of the spin quantum number  $m_s$  and in the change of its energy. It involves phonon-mediated mechanisms such as Raman and Orbach processes, as well as cross relaxation via dipole–dipole interaction. These spin-flips lead to subsequent population decay (i.e. spin-lattice relaxation) and as a result, the polarization of the  $NV^-$  spin population eventually decays back to thermally mixed state (that exists before optical pumping). This **spin relaxation** is characterized by  $T_1$  time scale and is quite sensitive to temperature. At room temperature, the phonon-mediated processes dominate in high-purity diamond samples, although they are relatively weak due to the low spin-orbit interaction and low phonon density of states.  $T_1$  for  $NV^-$  in bulk diamond at room temperature is typically few milliseconds (58). At low temperature,  $T_1$  is limited by cross relaxation because phonon interactions are suppressed. For high purity diamond crystal at 5 K the longitudinal relaxation time can reach 100 s (59).

### **Transverse relaxation time - $T_2, T_2^*$**

In compare to longitudinal relaxation time that describes the spin relaxation, transverse relaxation time characterizes the loss of phase coherence of a spin state. For the  $NV^-$  centre, this is dominated by spectral diffusion due to the fluctuations of the local fields predominantly from the spin–spin interactions (60).

$$\frac{1}{T_2} \cong \left(\frac{1}{T_2}\right)_{\substack{^{13}\text{C} \\ \text{flip-flop}}} + \left(\frac{1}{T_2}\right)_{\substack{\text{nitrogen} \\ \text{impurity}}} + \left(\frac{1}{T_2}\right)_{\substack{\text{paramagnetic} \\ \text{defect}}} + \left(\frac{1}{T_2}\right)_{\substack{\text{spin-lattice} \\ \text{relaxation}}} \quad (3.2)$$

Influence of particular interaction on the transverse relaxation time is dependent on the diamond crystal. One of the dominant sources of phase coherence loss of  $NV^-$  spin is dipolar hyperfine coupling with non-zero  $^{13}\text{C}$  nuclear spin bath ( $I = 1/2$ , with natural abundance of 1.1%). These spins are largely unpolarized (61), affecting each  $NV^-$  site with different effective magnetic field. This leads to inhomogeneous broadening of ensemble resonances. Interactions with nitrogen impurities (known as P1 centres,  $S = 1/2$ ) can also contribute significantly. It is assumed that two nitrogen atoms are required to form  $NV^-$  centre; one that is forming the  $NV^-$

and one that acts as a donor (62). The donor nitrogen  $N^+$  is not paramagnetic, but the unconverted P1 centres are. Other paramagnetic defects can influence the spin as well. This could be for example interaction with other NV centres (in samples with high NV concentration) or, for shallow NV centres, with paramagnetic species on the diamond surface. Transverse relaxation time can be also limited by the spin-lattice relaxation. However, this contribution is usually small even at room temperature due to the low (phonon-induced) longitudinal relaxation rate (36). Effect of all of these four interactions to transverse relaxation time is demonstrated in simplified equation (3.2).

$T_2$  is the characteristic time for homogeneous spin dephasing and is more commonly referred to as a **spin decoherence time**, whereas  $T_2^*$  is denoted as **spin dephasing time** and is the characteristic time for inhomogeneous spin dephasing. Specifically, while  $T_2$  is intrinsic to the NV centre and to its local spin environment (spin-spin relaxation),  $T_2^*$  is sensitive to external inhomogeneities (such as in applied static and MW fields). Typical  $T_2$  values range from milliseconds (for isotopically pure diamond) (30) to a few microseconds (for N-rich bulk diamond (63) or nanodiamond particles (64)).  $T_2^*$  times are shorter, usually in order of nanoseconds. However, it has been shown that for isotopically engineered high-purity diamond with low nitrogen and  $^{13}C$  concentration, the dephasing time can be extended past few microseconds (30). For most doping conditions  $T_1 \gg T_2 \gg T_2^*$ .

The dependence of longitudinal and transverse relaxation rates on magnetic field fluctuations in the NV- surrounding can be implemented for magnetometry and spin sensing application. The possibility to use NV- for magnetometry using static and pulse microwave resonance method will be discussed in following chapters.

### 3.3. Magnetic resonance of NV<sup>-</sup> centre

#### 3.3.1. Static EPR and ODMR

Electron paramagnetic resonance (EPR) (or electron spin resonance (ESR)) spectroscopy is analogous to that of nuclear magnetic resonance (NMR), but it is electron spins that are excited instead of the spins of atomic nuclei. The EPR spectra can be obtained by either varying the microwave (MW) frequency incident on a sample while holding the magnetic field constant or doing the reverse. When the energy of MW matches the energy of the gap between two spin states of unpaired electrons, the MW transmission is reduced.

To experimentally determine the NV spin resonances, method of Optically Detected Magnetic Resonance (ODMR) is used, with principle similar to the EPR. Simultaneous low intensity laser excitation (typically at 532 nm) and low power microwave (MW) radiation are applied. ODMR measurement is then realized by sweeping the microwave frequency (with range that contains resonance frequencies) and collecting luminescence signal. The drop in luminescence is observed at resonance frequency (2.87 GHz for zero external B field present), as the electrons are driven into the dark state. When external magnetic field is present, the ODMR spectrum of a single NV consists of two resonances: one corresponds to the ground state transition between  $m_s = 0$  and  $m_s = -1$  spin states, the other to the ground state transition between  $m_s = 0$  and  $m_s = +1$  spin states (see Figure 12). The splitting between the two resonances is proportional to the magnitude of the projected magnetic field along the NV symmetry axis. This is the basic operation principle of the most diamond-based magnetometers to date (65).

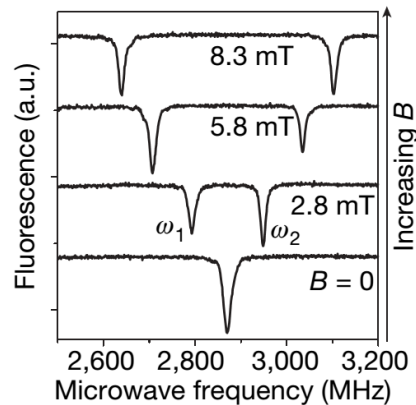


Figure 12: Optically detected magnetic resonance spectra for a single nitrogen-vacancy defect at increasing magnetic field (from bottom to top). Taken from (65).

### 3.3.2. Pulsed ODMR

Most of the sensing schemes, however, employ pulsed coherent manipulation and readout of NV spin state. The separation of spin manipulation, spin readout and phase accumulation (for e.g. magnetic field measurement) in time leads to reduction of power broadening effect of EPR lines (as less effective laser and MW power is applied) and enables various sensing schemes including those of NMR and nano-MRI. Some of the fundamental protocols are explained in following paragraphs.

### Rabi nutations:

The simple case is to apply laser pulse followed by a MW pulse. After the laser initialization, the NV is polarized to the spin state  $m_s = 0$ . Applying resonant MW field induces oscillations between the  $m_s = 0$  and  $m_s = \pm 1$  spin sublevels as the electron spins are transferred first to  $m_s = \pm 1$ , then back to  $m_s = 0$  by stimulated emission and so on (depending on the length and power of MW pulse). The pulse protocol for Rabi measurement is shown in Figure 13a. The length ( $\tau$ ) of the MW pulse is varied at fixed power to induce the oscillations. Subsequent laser pulse is used to readout the spin state. Hundreds of repetitions for each MW length are necessary to get sufficient statistics.

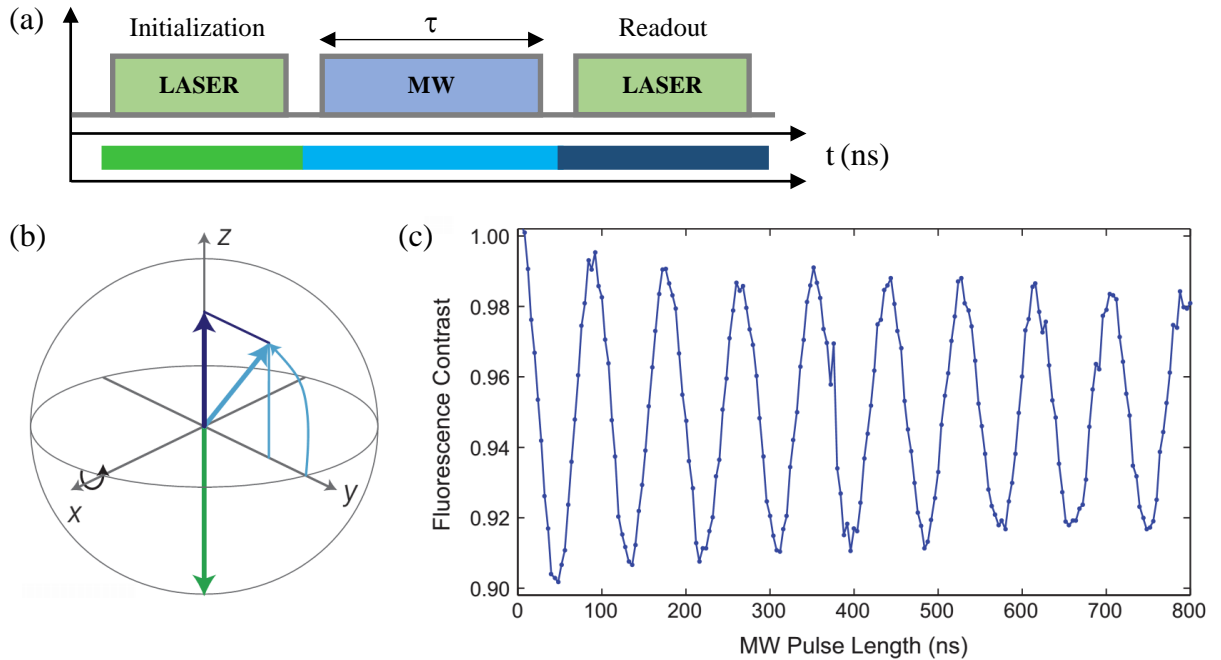


Figure 13: Demonstration of the Rabi measurement. (a) Pulse sequence used to induce and readout the oscillations and (b) the corresponding Bloch sphere. First, laser pulse polarizes the NV to the  $m_s = 0$  spin state (green arrow), after the MW resonant pulse is applied to flip the spin vector along the x axis (light blue arrow), finally the spin is readout by subsequent laser pulse (dark blue arrow). (c) Example of resulting Rabi curve with characteristic oscillation. Taken and modified (b) from (66) and (c) from (23).

In the beginning (for  $\tau = 0$ ), the luminescence signal is at the maximum as the NV spin is at the  $m_s = 0$  sublevel. When the duration of the MW pulse starts to increase, the luminescence signal begins to drop. Eventually, it reaches its minimum value when the spins are most likely to be in  $m_s = \pm 1$  sublevels. Such MW pulse that induces the flip between the sublevels is called  $\pi$  pulse and its duration (that can be obtained from fit of the Rabi curve) varies for different MW powers and different samples. Similarly, the MW pulse that brings the spin into the superposition of the two sublevels is called  $\pi/2$  pulse. The effect of the MW pulse to the spin

state is visualized at the Bloch sphere (see Figure 13b). The south pole corresponds to the initial  $m_s = 0$  state, MW induces rotation of the spin vector around the x axis and eventually flips the spin to the  $m_s = \pm 1$  state (north pole). An example of a typical Rabi curve is shown in Figure 13c where the normalized luminescence intensity is plotted as a function of MW pulse duration ( $\tau$ ). It is important to note that these nutations do not continue infinitely. There is a characteristic exponential decay as the control of spin state is fading over time and ultimately the oscillations are lost. Often there is a “beating” of the signal due to the detuned driving from the hyperfine transitions of the N nuclear spin, so one has to consider the Rabi curve to be the superposition of two or three sinus curves with different frequencies.

### **Ramsey fringes:**

Ramsey sequence is used to determine the dephasing time  $T_2^*$ . After the spin polarization, a  $\pi/2$  MW pulse is used to bring the spin into the superposition of the  $m_s = 0$  and  $m_s = \pm 1$  states (Figure 14a). The MW frequency is typically detuned from resonance to induce precession of the state vector around the z axis of the Bloch sphere (Figure 14b). As a result, second  $\pi/2$  MW pulse after time  $\tau$  does not always bring the spin to  $m_s = \pm 1$ , but an oscillation is observed (so-called Ramsey fringes) when the free precession time  $\tau$  is varied (Figure 14c). The resulting curve can also contain beating from the N hyperfine transitions (three in the case of  $^{14}\text{N}$ , two for  $^{15}\text{N}$ ). The  $T_2^*$  time is extracted from characteristic decay of the envelope of this curve. This damping of the oscillation is induced by spin bath fluctuations and is present even in high purity samples, where dephasing is dominated by the  $^{13}\text{C}$  naturally present in the diamond lattice. Ramsey sequence is commonly employed for DC magnetometry (see chapter 3.4.3) and in other sensing schemes. This is because during the free evolution (precession) time  $\tau$ , the two spin sublevels are in superposition and the spin accumulates a phase shift depending on the magnetic field of the environment. The accumulated phase is then converted to either  $m_s = 0$  or  $m_s = \pm 1$  states and is thus detectable. Therefore, an observation of free (undriven) dynamics of external spins is possible with this technique, which is essential to study local magnetic fields and spin environment of the NV.

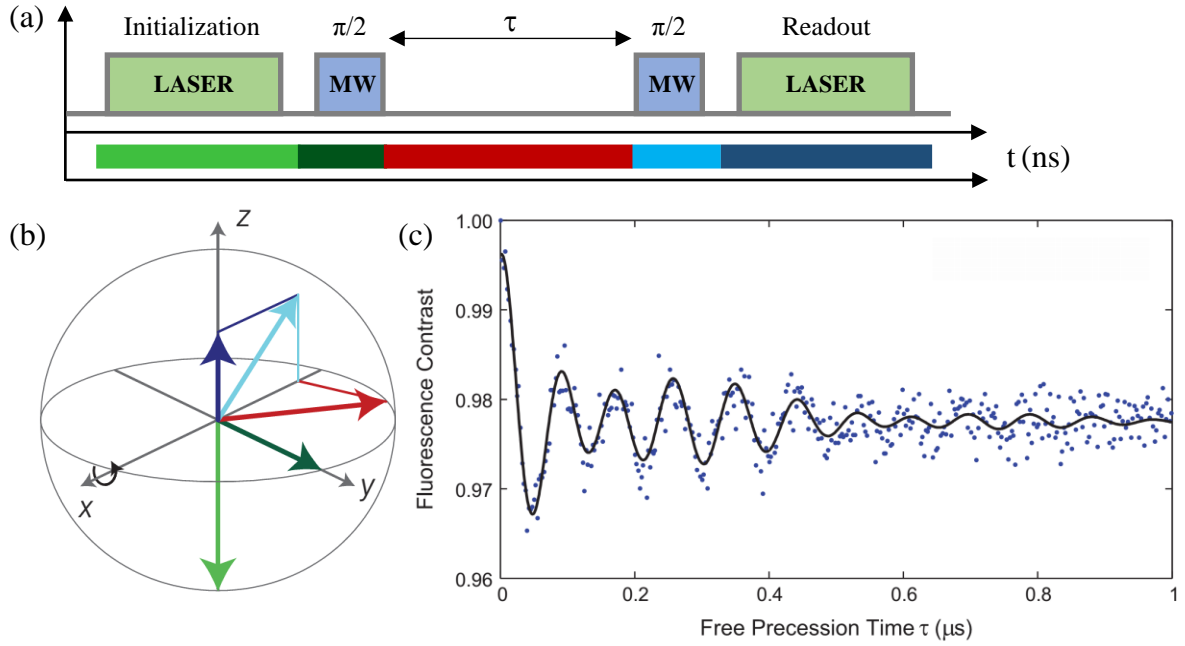


Figure 14: Demonstration of the Ramsey measurement. (a) Pulse sequence used to induce and readout the Ramsey fringes and (b) the corresponding Bloch sphere. First, laser pulse polarizes the NV to the  $m_s = 0$  spin state (light green arrow), after the MW  $\pi/2$  pulse is applied to bring the spin into a superposition state (dark green arrow), during the free precession time  $\tau$  the spin accumulates the phase (red arrow), another MW  $\pi/2$  pulse projects the phase to one of the sublevels (light blue arrow) and finally the spin is readout by subsequent laser pulse (dark blue arrow). (c) Example of resulting Ramsey curve with characteristic oscillation. Taken and modified (b) from (66) and (c) from (23).

### Hahn-echo:

Even though Ramsey interferometry can be employed to probe the spin bath of NV environment, the rapid decay and strong modulation lower the sensitivity of this method and usually preclude the sensing of a single spin. To refocus the dephasing induced by static or slowly varying magnetic fields and thus to enhance the sensitivity, in Hahn-echo, a  $\pi$ -pulse is inserted into the middle of the free evolution time of the Ramsey sequence (see Figure 15). The  $\pi$ -pulse inverts the accumulated phase of the first  $\tau/2$  and as a same amount of phase from DC fields is accumulated over the second free precession interval  $\tau/2$ , the net phase shift is eliminated (ideally). The relaxation time is prolonged to the decoherence  $T_2$  value but as a consequence, Hahn-echo is insensitive to static magnetic fields (and to slow magnetic field frequencies  $\lesssim 1/T_2$ ), albeit it can reach high sensitivity to the AC fields (see chapter 3.4.3) with the frequency of  $1/\tau$  as demonstrated on single spin NMR (see chapter 3.4.5).

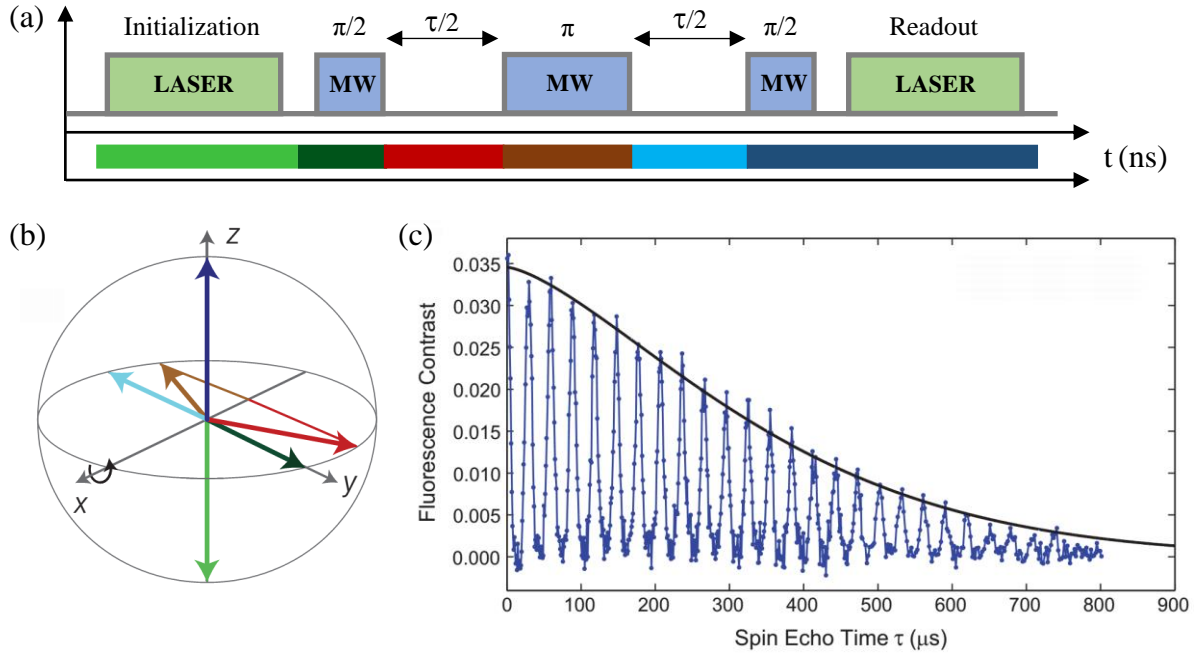


Figure 15: Demonstration of Hahn-echo measurement. (a) Pulse sequence used to induce and readout the echo measurement and (b) the corresponding Bloch sphere. First, laser pulse polarizes the NV to the  $m_s = 0$  spin state (light green arrow), the MW  $\pi/2$  pulse is applied to bring the spin into a superposition state (dark green arrow), after a delay of  $\tau/2$  (red arrow)  $\pi$ -pulse mirrors the state vector to the other half of the Bloch sphere (brown arrow), after another delay of  $\tau/2$  (light blue arrow) the spin is projected to one of its sublevels ( $m_s = 0$  or  $m_s = \pm 1$ ) by MW  $\pi/2$  pulse and is subsequently readout by laser pulse (dark blue arrow). (c) Example of resulting Ramsey curve with characteristic oscillation. Taken and modified (b) from (66) and (c) from (23).

### 3.4. Sensing with NV<sup>-</sup> centre

#### 3.4.1. Magnetometry

Detection and imaging of weak magnetic fields is of high importance considering the vast application range of magnetic sensors. Measurements of magnetic fields can reveal information about the electrical activity in the human brain and heart, chemical identity of certain atoms or simply indicate the presence or absence of metal (67). For many years we have been using magnetic sensors for analyzing and controlling many functions. We can find magnetic sensors in read heads in computer hard-disks, in cars for determination of the engine crank shaft or wheel braking position. Airplanes fly with higher safety standards thanks to non-contact switching with magnetic sensors (68). In medicine, measurements associated with the neural currents in the brain can be used to diagnose epilepsy, stroke and mental illnesses, as well as to study brain function (69). Even more possibilities would open up with routine detection of very low magnetic fields ( $\sim$  fT,  $\sim$  pT) with nanoscale spatial resolution, such as magnetoencephalography (MEG) (69), magnetic resonance force microscopy (MRFM) (70) or more powerful applications of for example magnetic resonance imaging (MRI), magnetic force microscopy (MRF), and scanning Hall probe microscopy (71).

Magnitude of magnetic field can be determined using variety of different techniques and technologies. Each of them has its own unique properties making it suitable for particular applications. Sensors' usage can range from simply sensing the presence or change in the magnetic field to the precise measurement of magnetic field's scalar or vector properties. To determine which sensor is best suited for specific application, one has to take into account the sensors' cost, frequency response, size, power requirements, and of course its sensitivity (68).

The most important characteristic of magnetic sensor is its **sensitivity** and the frequency range of signals to which it will respond. Therefore it is necessary to consider how the inherent noise of the instrument varies with frequency. The noise level at frequency "f" is traditionally specified as the spectral density  $S_B(f)$  of the equivalent mean-square field within 1 Hz bandwidth centered at the frequency f. So, for example, when considering white noise (a random signal having equal intensity at different frequencies),  $S_B$  is independent from frequency, and the total mean-square field noise detected in a measurement is equal to  $S_B$  multiplied by the bandwidth, within which the measurement is made. But since  $S_B$  is related to the square of the field (when comparing noise with the strength of signal), it is more relevant to consider the square root of the spectral density, which has the unit of "tesla per root hertz" ( $T/\sqrt{Hz}$ ) and gives the root mean square (RMS) field within a 1 Hz bandwidth. Thus, with white noise, the total RMS field detected in a measurement is equal to square root of  $S_B$  multiplied by the square root of the bandwidth (72).

Measuring of weak magnetic fields, however, is complicated for several reasons. Main problem arises from the presence of ambient magnetic noise everywhere around us. The strength of the Earth's magnetic field amounts to around tens of  $\mu T$  (69) and geomagnetic noise has magnitude of approximately hundreds of pT (68). But many more things are the source of the magnetic disturbance, such as power lines (up to  $\mu T$ ) or even steel car passing by (nT), or screw driver in close proximity (up to nT) (69). Also, the biomagnetic fields have to be considered. For example, heart's magnetic fields above chest are 100 to 1000 times stronger than the signals from brain above the head (0.1 to 1 pT). So it is much easier to measure heart rhythm than it is to measure brain fields (69).

There are few options how to reduce the ambient noise. One of them is shielding the desired magnetic object using passive or active method. Locally, shields made of thick layer of high magnetic permeability metal like Mumetal, Permalloy (both alloys of nickel and iron) or

sheet of aluminium can be used. For instance thick hemispherical shell of lead, cooled to liquid Helium temperature to become superconductive, is used during the MEG measurement because superconductors perfectly reflect magnetic fields (69). Active shielding can be achieved using magnetically shielded rooms with reference sensor that read ambient magnetic field signals for computer correction. It is a whole room that is created out of Mumetal and aluminium, which magnetically shields the ongoing measurement. Similarly to active shielding, use of several reference sensors is possible to reduce ambient noise. By taking the difference between the readings of two or more spatially separated sensors, it is possible to filter desirable signal (68). Combination of both techniques mentioned above is usually necessary when measuring very low magnetic fields.

Magnetic sensors can be divided into **vector magnetometers** that measure component of magnetic field and **scalar** (also called total field) **magnetometers** that measure the magnitude of the magnetic field (73). It might seem that vector magnetometers are superior to total field magnetometers, since they carry out additional information. For some cases, however, scalar magnetometers provide exceeding results. Consider measuring a moving ferromagnetic object and trying to detect small changes in magnetic field. Rotational vibration due to the motion will generate changes in the vector components of the earth's field detected by a vector magnetometer. These changes are difficult to separate from the signal and are often much greater than the signal from ferromagnetic object (68). Scalar magnetometers carry the important advantage of insensitivity to rotational vibrations.

### 3.4.2. Opportunities and challenges for NV<sup>-</sup> centre

Although best sensors can measure a field as low as few pT (i.e. SQUID (69)), they require low temperature, extreme vacuum or long data acquisition, all of which restricts their application. Resonance magnetometers, on the other hand, have limited sensitivity due to the spin-altering collisions (74). Nitrogen-vacancy (NV) centres could serve as a possible alternative for detection of weak magnetic fields with high resolution. As stated in previous chapters, NV<sup>-</sup> centres possess excellent properties, which make them well-suited for magnetometry. It is a stable point defect and it can be theoretically localized on sub-nanometer length scale. Therefore, the spatial resolution of a single-NV magnetic sensor is typically a few nanometers. Moreover, NV centre spin can exhibit long coherence times at room temperature (thus allowing sensitive magnetometry in ambient conditions) and it can be easily initialized and manipulated. In addition, a diamond (with NV centre) is stable over a wide range of

pressures, temperatures, etc., allowing the possibility of magnetic field measurement in harsh environments. Over the past few years, various magnetic methods using NV centres in bulk as well as in nanoparticles have been developed (75) (76).

However, there is still a technical challenge for room temperature magnetometers and that is the sharp temperature dependence of magnitude on the ground state zero-field splitting ( $D_{gs}$ ). Recently it was proposed, that happens due to the lattice expansion, which effectively changes the displacement of the electronic spins (77). The slope of this dependence is  $dD_{gs}/dT \approx -75 \text{ kHz/K}$ , so even if ambient temperature can be controlled at the 1-mK level, this would lead to magnetic field variation of 3 nT. One of the solution is monitoring both of the  $\Delta m_s = \pm 1$  resonances, as the energy difference between the two resonances depends only on magnetic field and does not depend on  $D_{gs}$ . Alternatively, using two phase synchronized microwave tones (78) to produce coherence and observe precession directly amongst the  $m_s = \pm 1$  levels could be employed. It has been already shown (38) that using this method, it is possible to obtain  $\sim 10 \text{ nT}/\sqrt{\text{Hz}}$  sensitivity under 4 mT bias field that is promising.

Another challenge is a presence of not yet discussed transverse splitting parameter  $E$ . The  $E$  parameter arises from interaction with stray electric fields in the lattice and its value varies in from kHz to MHz. Even a slight mixing of  $E$  with excited state orbitals produces a transverse dipole moment in order of  $10 \text{ Hz}/(\text{V/cm})$  (79). Therefore, it is necessary to apply an axial bias magnetic field  $|B_z| \gg E/(g_s \mu_B)$  in order to measure small variations of signal. In high-purity diamond,  $E$  corresponds to kHz and only a moderate  $100 \mu\text{T}$ -scale field is necessary to reinforce magnetometer linearity. Using a current source with a stability of  $\text{ppm}/\sqrt{\text{Hz}}$  would be sufficient to achieve the  $\text{sub-nT}/\sqrt{\text{Hz}}$  required for many applications. In fact, one could get rid of bias field almost entirely if the ODMR linewidths were narrow enough to resolve hyperfine structure of NV, because the  $m_s = \pm 1$  sublevels are insensitive to strain and split linearly with magnetic field (even near zero field) (80).

### 3.4.3. Magnetic field sensing schemes

There are three major schemes for measuring magnetic fields, and these are discussed in following chapters. It is the DC magnetometry using both EPR or Ramsey sequence and the AC magnetometry.

### DC magnetometry: EPR

The simplest method to measure magnetic field is to extract the information directly from EPR (or ODMR) spectrum, reading out the difference of resonant frequencies. The Zeeman splitting is proportional to the projection of magnetic field along the NV symmetry axis. A known static field  $B_0$  can be applied to spectrally distinguish the four possible NV orientations. Any additional unknown field  $\delta B$  would result in a shift of EPR resonant frequencies as the total magnetic field  $B_{net}$  changes. If the NV fluorescence occupies at least three of the four possible NV orientations, vector information of the unknown magnetic field can be obtained as well. In addition, EPR can be measured using pulse laser and MW excitation. In this case, the MW power can be lower than in continuous EPR, thus reducing the MW power linewidth broadening and enhancing the sensitivity (23).

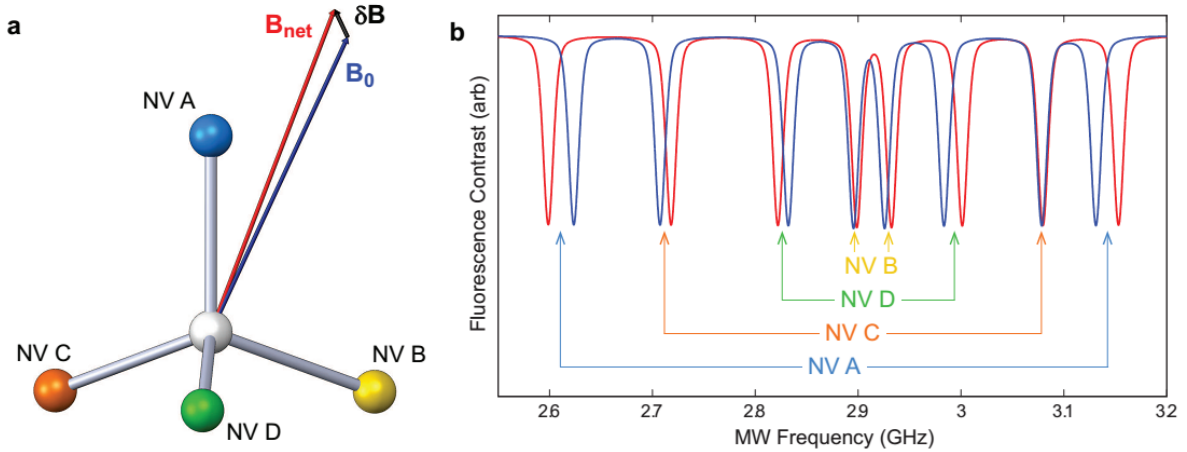


Figure 16: Example of EPR based DC magnetometry. (a) Diagram showing the four possible NV orientation (noted NV A-D) with the relation to the known static field  $B_0$ , unknown field  $\delta B$  and resulting total magnetic field  $B_{net}$ . (b) Modeled EPR spectra in the presence of known static field  $B_0$ , (blue) and the resulting total magnetic field  $B_{net}$  (red). When comparing resonance shifts between the two spectra, the unknown magnetic field  $\delta B$  can be extracted. Taken from (23).

### DC magnetometry: Ramsay sequence

Similarly, DC magnetic fields can be measured using Ramsay sequence. Typically, known static external magnetic field is applied to split  $m_s = \pm 1$  states. In the beginning, short optical excitation pulse is used to polarize the NV spin into the  $m_s = 0$  state. Afterwards, MW  $\pi/2$  pulse prepares the spin into a superposition of  $m_s = 0$  and  $m_s = +1$  states. Here, spin freely precesses for specific time duration  $\tau$ . During this, it accumulates a phase  $\phi = 2\pi\gamma B\tau$ , where  $B$  is the unknown static magnetic field and  $\gamma$  is the gyromagnetic constant of NV. After  $\tau$ , another  $\pi/2$  pulse is applied to project the spin back into either  $m_s = 0$  or  $m_s = +1$ , from which the phase

accumulation can be calculated. Actual measurement can be done by sweeping the free precession time  $\tau$ .

Both the techniques of the DC magnetometry are limited by the linewidths of EPR resonance. Those are fundamentally set by the inverse of the NV dephasing time  $T_2^*$ . In high purity diamonds,  $T_2^*$  is usually in the order of  $\sim 1 \mu\text{s}$ . Better sensitivity can be obtained using high-purity isotopically-engineered sample, where  $T_2^*$  can be in the order of  $\sim 100 \mu\text{s}$  (30). For AC measurement, the sensitivity is limited by NV decoherence time  $T_2$ , rather than by  $T_2^*$  dephasing time. Decoherence times are generally longer ( $\sim 500 \mu\text{s}$  for high purity or even few ms for isotopically-engineered samples) giving higher sensitivity (81).

### **AC magnetometry**

The characteristic time scale of the NV signal decay can be extended from  $T_2^*$  dephasing to  $T_2$  decoherence by employing a spin echo sequence. The spin echo (also known as Hahn echo) sequence is extension of Ramsay sequence. After the spin is prepared by MW  $\pi/2$  pulse to superposition state,  $\pi$  pulses are used to invert the accumulated phase before using second  $\pi/2$  pulse. This, however leads to insensitivity to static magnetic fields because accumulated phase shift is echoed out during the  $\pi$  pulse. Considering AC oscillating magnetic field, spin echo pulse sequence can be applied in a way that the MW pulses coincide with the nodes of magnetic field. Therefore, the phase accumulated in each half of the pulse sequence is additive rather than subtractive. This means that the spin echo enables to measure AC magnetic field, where the frequency range (over which the magnetometer is sensitive) is determined by the full pulse sequence duration  $\tau$  (determining the optimal frequency  $f_{ac} = 1/\tau$ ). In the absence of AC magnetic field, no phase is accumulated and all spins are projected back to  $m_s = 0$  (bright state), whereas when the AC magnetic field of optimal frequency is present, the NV spins accumulate net phase of  $\phi = 4\pi\gamma B\tau$  and have higher chance of falling into the dark state (23). Signal is then detected by measuring the luminescence intensity.

#### **3.4.4. Experimental realizations**

Up-to-date NV-diamond-based magnetometers can be generally (depending on their design principle) divided into four categories: near-field scanning probes, far-field sub-wavelength probes, wide-field array magnetometers, and bulk micro-scale sensors. This chapter describes the state of art of NV-based magnetometers and discusses their design principles.

### Near-field scanning probes

Perhaps the simplest design employs the nanodiamond with single NV centre as the tip for the atomic force microscopy (AFM). See Figure 17. The resonance frequency (or spin echo for AC measurements) is then monitored using ODMR techniques. The system is called “near-field”, because the spatial resolution is limited only by the distance between the sample and the NV centre, not by the diffraction limit of luminescence light. The reach of this method is to detect a small signal from ensemble of nuclear or electronic spins. The ultimate goal would be to detect signal from single electronic spin or even single nuclear spin (82) (83). To improve spatial resolution to potentially single-spin level employment of a large magnetic field gradient is possible, thus encoding spatial information spectrally, as is commonly used in conventional magnetic resonance imaging (MRI). Sensitivity of  $\sim 4 \text{ nT}/\sqrt{\text{Hz}}$  to AC fields and  $\sim 0.5 \mu\text{T}/\sqrt{\text{Hz}}$  to DC fields has been demonstrated (30) for single NV centre in the isotopically pure diamond. Importantly, magnetometer with wide bandwidth (from DC to  $\sim 0.3 \text{ MHz}$ ) was shown possible for NV centre as an AFM tip (84). However, the sensitivity was only few  $\mu\text{T}/\sqrt{\text{Hz}}$ .

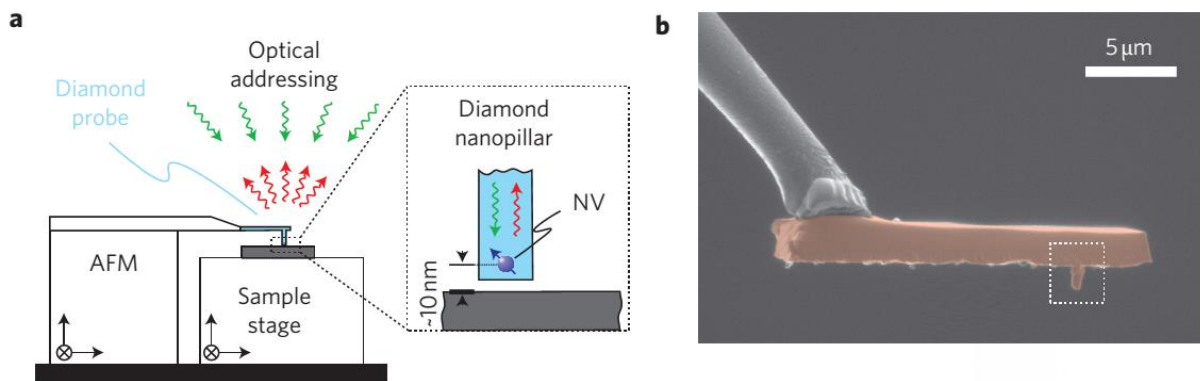


Figure 17: Magnetic sensing design with NV centre as a tip for AFM. (a) Schematics of the setup combining AFM and optical excitation (green arrows) and read out (red arrows) of NV centre. (b) SEM image of a single crystalline diamond nanopillar probe. Taken from (85).

### Far-field sub-wavelength probes

Another way of bypassing the diffraction limit is to use methods of RESOLFT (Reversible Saturable Optical Fluorescence Transitions) or STED (Stimulated Emission Depletion). STED uses an intense, ring shaped laser beam to deplete the excited state via stimulated emission (see Figure 18). Recent nanoscopy measurements using STED on bulk diamond have achieved a spatial resolution below 6 nm (86). In principle, a short ( $< 10 \text{ ns}$ ) green laser pulse (typically 532 nm) is used to excite NV centres, followed by second pulse of laser light, called STED beam, tuned within the phonon sideband (around 700 nm). STED beam

is shaped by a helical phase plate into a doughnut shape with dark region in the centre and depletes the  $\text{NV}^-$  centres back to the ground state by stimulated emission. This leaves only a fraction of the  $\text{NV}^-$  centres in the very center of the STED beam in the  $^3\text{E}$  excited fluorescent state. The dark region of STED is significantly smaller than the wavelength of the light, thus bringing spatial resolution below diffraction limit. STED laser needs to be of higher intensities. For NVs this value could be of  $100 \text{ MW/cm}^2$ , which is still well below the diamond damage threshold (86), and giving fundamental limit of lateral resolution of about 5 nm. However, for some biological application, use of such intensities is not possible due to the sample damaging. Lower intensities can be employed when transferring the  $\text{NV}^-$  centres into the metastable state instead of ground state (87). For instance, spatial resolution of 38 nm has been already demonstrated with technique called “spin-RESOLFT” using microsecond pulses of light with intensity of  $3 \text{ MW/cm}^2$  (88). Another way is to drive  $\text{NV}^-$  centres into a different trapped state using red excitation. This method is still under investigation, but already a 12 nm spatial resolution has been achieved using laser intensity of  $12 \text{ MW/cm}^2$ . It is believed that trapping of  $\text{NV}^-$  centres switches them into  $\text{NV}^0$  (89).

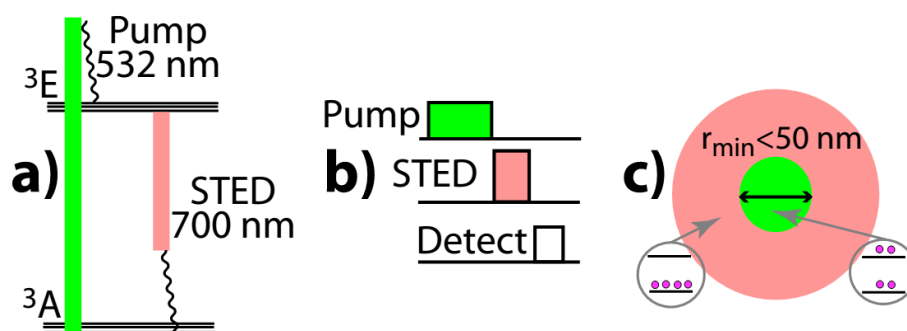


Figure 18: STED principle. (a) Level diagram and optical transitions for the STED scheme. (b) Timing diagram for STED pulse sequence. (c) Spatial diagram of STED doughnut shape (pink) and fraction of NVs remained in excited state (green). Taken from (35).

### Wide-field array detectors

So far we have considered only single  $\text{NV}^-$  centre for magnetic detection, which gives the best spatial resolution. Still, ensembles of  $\text{NV}^-$  centres can be used to image much wider fields of view together with even greater sensitivity. Wide-field fluorescence microscopy uses a thin layer of  $\text{NV}^-$  centres to acquire magnetic image. The thickness of the layer usually matches the desired resolution, which is typically between few hundred nanometers and a micrometer. Same objective is used for both excitation of  $\text{NV}^-$  centres and fluorescence collection. Signal is then spectrally filtered and directed to a charge-coupled device (CCD)

camera (see Figure 19). This principle was recently demonstrated in (90) with field of view of  $\sim 60 \mu\text{m}$  and spatial resolution of  $\sim 500 \mu\text{m}$ .

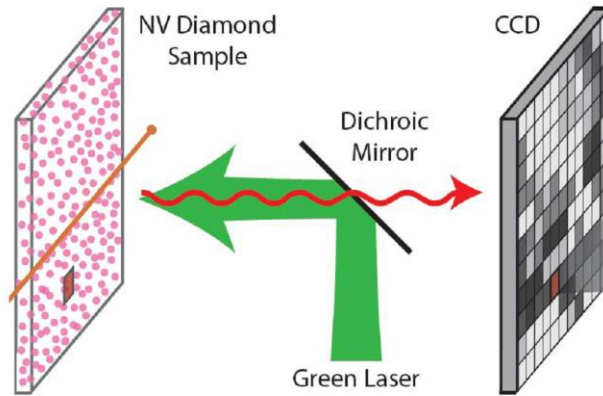


Figure 19: Principle of wide-field fluorescence microscopy used for magnetic imaging, where the sample of the study is placed in close contact with the thin layer of NV<sup>-</sup> rich diamond. Taken from (55).

### Bulk micro-scale sensors

The primary sensitivity limitation for fluorescence-based magnetometers is fluorescence collection efficiency and limited signal contrast. This problem can be circumvented by using infrared transmission detection. As explained before, NV<sup>-</sup> can undergo intersystem crossing via alternative non-radiative decay path through metastable singlet state with 1042 nm transition. Under continuous optical pumping, the population of NV<sup>-</sup> in the metastable singlet state can also be detected by monitoring the transmission of the 1042 nm laser probe (see Figure 20). When microwaves with resonant frequency are present, the population of NV<sup>-</sup> is transferred to the  $m_s = \pm 1$  state resulting in greater population in metastable state and therefore lower 1042 nm probe transmission. Additional readout of the spin polarization of NV<sup>-</sup> ensemble and enhancing sensitivity is then enabled. Using this technique, it was already possible to project photon shot-noise limited sensitivity of 5 pT in one second of acquisition with bandwidth from DC to few MHz (91).

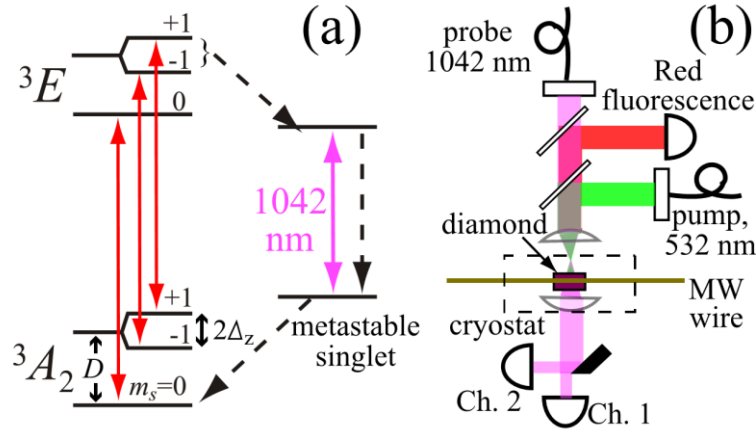


Figure 20: Bulk NV based micro-magnetometry. (a) Level structure of NV<sup>-</sup> centre with allowed optical transitions. (b) Schematics of infrared absorption magnetometer. Taken from (91).

### 3.4.5. NMR and nano-MRI

The fact that the NV spin quantum states can be influenced even by ultra-weak external electric or magnetic fields can be used to probe external spins by the means of NMR or nano-MRI. The NV sensitivity is approaching the sensitivity of SQUIDs and cold atom ensembles ( $\sim \text{fT}\sqrt{\text{Hz}}$ ), but using a single NV centre qubit spatial resolution of single molecule can be reached and moreover, NV operates at room temperature. Some first works have demonstrated single NV qubit sensor as quantum spin-probe for detection of external single electron spin (92), nuclear spins (75), or even 3D nano-MRI (8). By using the NMR-based protocols, the resulting information can be worked out either classically or by using quantum tomography techniques, approaching super-resolution (8). The main principle of such methods is detection of weak magnetic fields originating from the targeted spins by appropriate manipulation of the spins, to affect the precession phase accumulation of the highly coherent NV electronic spin. For instance, electron spin external to diamond can be detected using double electron–electron resonance (DEER), where spin echo MW sequence ( $\pi/2, \pi, \pi/2$ ) is applied to NV centre and a RF pulse tuned to NV  $\pi$ -pulse is scanned to flip the probed spin, therefore the spins dipolar magnetic field is reversed and the equivalence of the NV spin precession is disturbed. Using similar scheme, a single proton NMR (both time-domain and spectroscopic) can be detected sensing nanotesla field fluctuations at room temperature (75). Current quantum methods using optical readout of single NV lead to voxel volume of approximately  $5 \text{ nm}^3$  (93). This is a significant application of the NV sensor, since the conventional coil-based induction NMR method is insensitive to samples at nanometer scale.

#### 3.4.6. Summary

The negatively charged NV centre in diamond is widely studied due its unique optical and spin properties. It has a paramagnetic ground state with long coherence times ( $> 2$  ms (30)), and spin levels that can be initialized and detected by optical excitation in a broad range of wavelengths (94) and manipulated on sub-nanosecond timescales (95) by microwave excitation. Together with excellent thermal, electrical, and mechanical properties of diamond, NV<sup>-</sup> centre is a promising candidate for ultra-sensitive metrology (55) (65). Recently, many techniques for measuring magnetic fields at the micro- and nanometer scale have emerged based on NV<sup>-</sup> electron spin resonances (96). These magnetometers offer an exceptional combination of sensitivity and spatial resolution rivaling those of superconducting quantum interference devices (SQUIDs) (97) and on top of that, they can operate in a wide temperature range (from 0 K to above room temperature). The NV magnetic sensors could be applied to study biomagnetic systems (e.g., neurons, cardiac cells, nano-scale biological imaging) (98), geomagnetism, microelectronic circuits, novel materials (e.g, graphene), and nuclear magnetic resonance spectroscopy and imaging from organic material at the diamond surface (75). Overall, NV based probes are good alternative to common high-sensitivity sensors that usually require low temperature or extreme vacuum to operate, or have long data acquisition.

## 4. RESULTS

Results described in following chapters deal with the fabrication, application and detection methods of NV -based sensors for molecular diagnostic developing further the current state of art described in the introduction. Two main diamond systems were studied for this purpose; luminescent nanodiamond particles and NV containing single crystal diamonds.

**Chapter 4.1:** Here, the system used for the specific NV detection is described. The optical confocal setup was built for this purpose (at FBME) during the first year of my study. It enables luminescence imaging (with 300 nm resolution) and spectral acquisition with optimization for optical detection of NV centres. Two additional single-photon-counting detectors provide time-correlated single-photon-counting (TCSPC) measurements such as photon antibunching. Setup is already prepared to be enhanced by the methods of ODMR for magnetic sensing and readout of the NV relaxation times. This has been realized during my last year on similar setup (Hasselt University) where such enhancement enabled pulsed detection of magnetic resonances (see chapter 4.8).

**Chapters: 4.2, 4.3, 4.4, 4.5:** Following results study the **ND particles** with aim to facilitate the use of nanodiamonds as a novel sensitive nanoscale probe that can be used for quantum measurements and for diagnostics in medicine. To obtain even better properties of fluorescent NDs, the NV luminescence was studied for different fabrication methods. New scheme based on direct irradiation of nanodiamonds in aqueous colloidal suspension by high-energy protons has been established, leading to a larger fraction of fluorescent particles, more homogenous distribution of nitrogen-vacancy centres per particle and lower lattice damages compared to dry powder irradiation (see **chapter 4.2**). To further boost the NV<sup>-</sup> luminescence, we have developed a new mild and easy fluorination method that is non-destructive and provides high yield production of NDs. We demonstrate increase of NV<sup>-</sup>/NV<sup>0</sup> luminescence ratio with comparison to oxidized NDs together with stabilization of small particles that contains exactly one NV centre (see **chapter 4.3**). Afterwards, we studied internalization processes of NDs in various cell lines and examined the possible detection methods of NDs in cell environment. We have developed a novel method of imaging NV luminescence by Raman confocal microscopy. This enabled us to distinguish between NDs in and out of the cell and to visualize the cell nucleus of living cells clearly without using any additional dye (see **chapter 4.4**). To investigate the uptake rate of NDs by individual cell in time, we employ the atomic

force microscopy (AFM) in imaging and force spectroscopy mode. By measuring a time-consequent force maps and thus obtaining change of the cell membrane Young's modulus, we were able to characterize the internalization process as we observe cell membrane stiffening upon ND uptake (**see chapter 4.5**).

**Chapters: 4.6, 4.7, 4.8:** The last part of the results deals with enhancement of NV sensors based on **single crystal diamond** with aim to provide higher detection rates for NV spin readout. Conventional readout techniques of such sensors are based on optical detection of magnetic resonance and are thus limited by the efficiency of photon collection. We demonstrated a novel method of spin read out by means of photoelectrical detection denoted "Photocurrent Detection of Magnetic Resonance" (PDMR). It avoids the complexity of confocal imaging and would allow for example the detection of NV<sup>-</sup> spin resonance in light-scattering media, which would be an advantage for various sensing applications and may lead to a construction of novel sensitive quantum sensors (**see chapter 4.6**). In following work we have studied detection capabilities of the PDMR. We demonstrated higher contrast for dual beam PDMR where two lasers (green and blue) are used for the NV ionization. The improvement is relevant mainly for sample with high nitrogen defects concentration (**see chapter 4.7**). Finally, we have developed a pulsed protocol that enables low-noise coherent spin manipulation a detection of only few NV centres in focus. We demonstrate this on Rabi and Ramsey spin measurements with high S/N ratio. Predictions for single NV PDMR detection are calculated from the contrast measured on small NV ensembles (down to 5 NVs in focus). **See chapter 4.8.**

All of these results have been either published or presented at international scientific conferences and follow accordingly as described above. My contribution for the particular results is specified in the beginning of each chapter.

#### 4.1. Home-built setup for detection of NV related signals

The optical confocal setup specially designed to readout NV centres was developed and enhanced during the whole duration of my doctoral study. This chapter serves as a short demonstration of its imaging and spectroscopic capabilities. Later, the setup will be enhanced by detection of NV related magnetic resonances and improved to enable coherent spin manipulation and detection. The first results of this work were presented at the **18th International Microscopy Congress (IMC)**, 2014 in form of a poster. As a main author, I was in charge of construction of the optical setup. Co-authors of the work are: J. Hrubý, V. Petráková, Z. Remeš and M. Nesládek. J. Hrubý wrote LabView software for automatization of the measurements and helped with the testing of program functioning. V. Petráková, Z. Remeš and M. Nesládek helped with the designing of the setup and provided useful advices and suggestions. The photograph at Figure 21 shows the constructed setup.

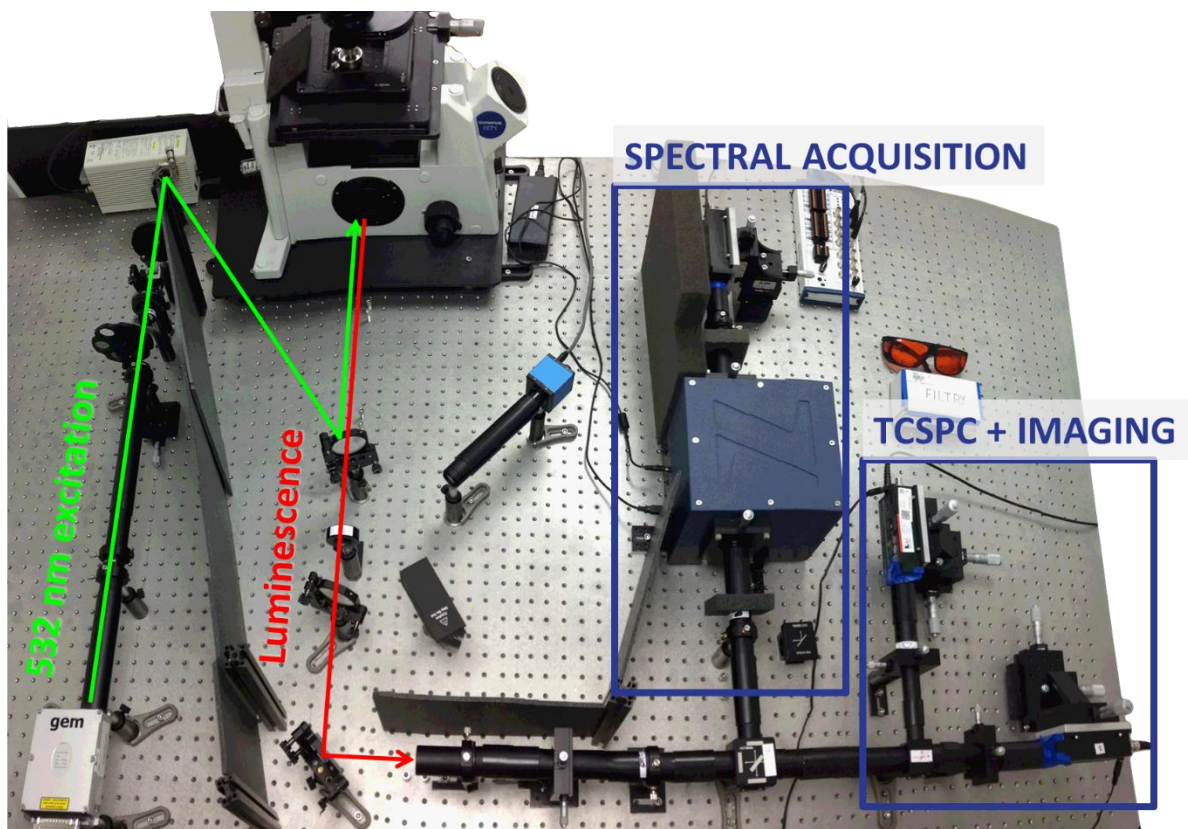


Figure 21: Photo of home-built optical confocal setup. Laser – 532 nm, tunable power <500 mW (Nd:YAG), nanometric XY scanning piezo-stage (P-545.R7 PIInano®), Monochromator - Omni- $\lambda$  150, grating 1200 l/mm with blaze 500nm, detectors - silicone avalanche photodiode (SPCM-AQRH-14).

The green laser 532 nm is used to excite the NV centres and the luminescent signal is detected by the single-photon avalanche photo-diodes (APDs). The schematic interpretation of the setup with all the components is depicted in Figure 22.

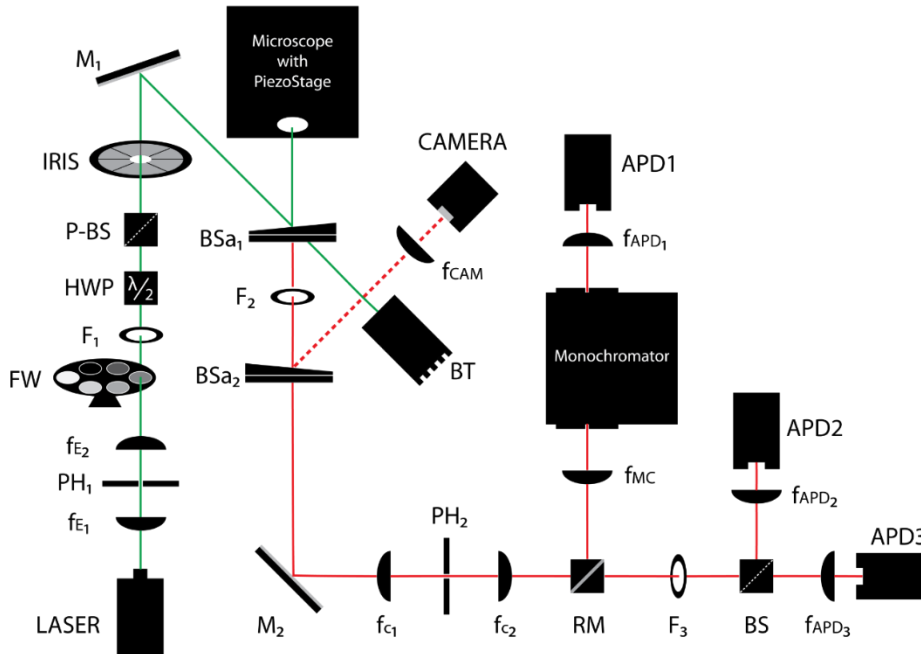


Figure 22: Schematics of the setup;  $f$  – lense,  $PH_1$  – 150  $\mu\text{m}$  pinhole,  $FW$  – filter wheel,  $F$  – filter,  $HWP$  – Half-wave plate,  $P$ -BS – polarizing beamsplitter cube,  $M$  – mirror,  $BSa$  – beam sampler,  $BT$  – beam trap,  $PH_2$  – 25  $\mu\text{m}$  pinhole,  $RM$  – removable mirror,  $BS$  – beamsplitter cube,  $APD$  – avalanche photodiode.

The obtained lateral resolution of the setup reaches  $\sim 300$  nm for the luminescence imaging with possibility of subscans (see Figure 23). The single-photon confocal scanning microscope enables measuring the particle fluorescence with a high resolution allowing to detect single nanocrystals and to measure their spectra. Spectral scans from both NV centres and quantum dots have been obtained with high sensitivity (see Figure 23c). The correlation spectroscopy measurement (anti-bunching) in biological samples allows distinguishing the particle with single NV centres and their specific interaction with the biological environment.

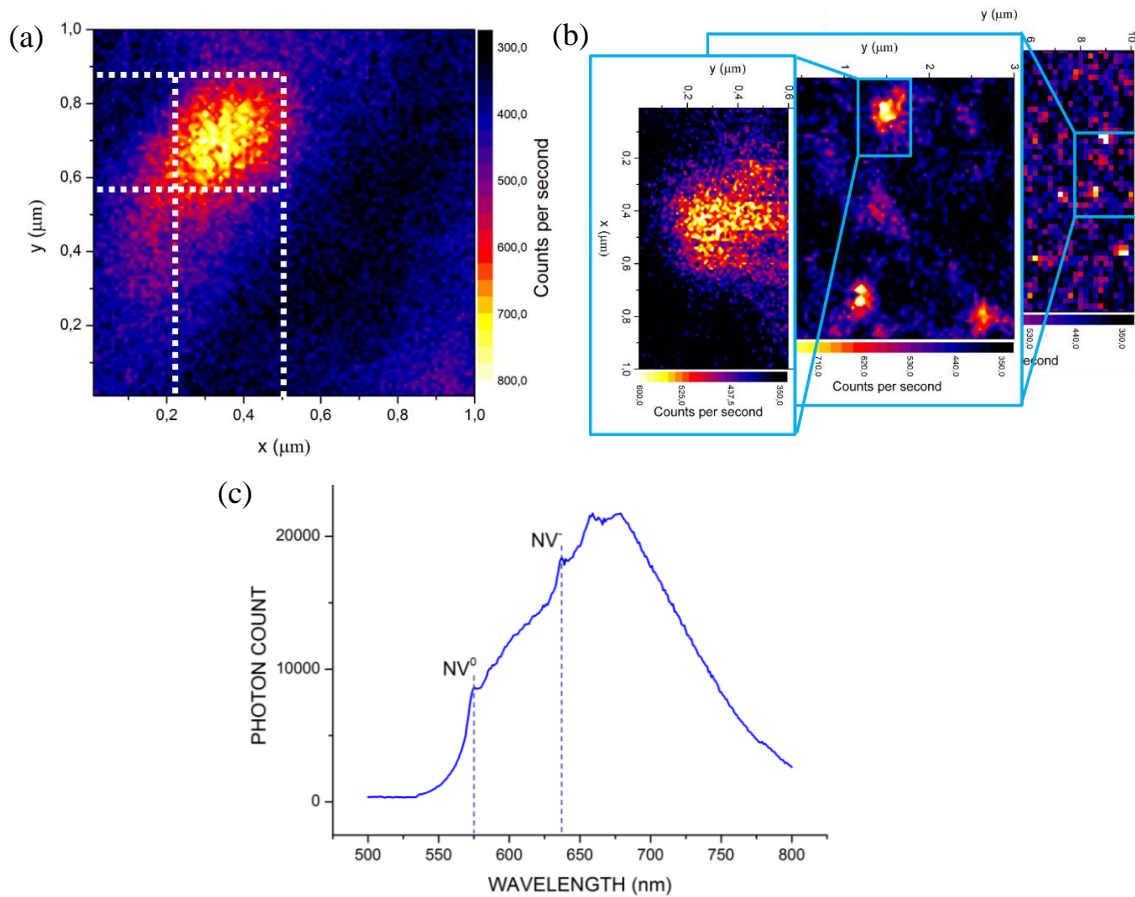


Figure 23: (a) Resolution was measured using quantum dots (QD) of 6 nm in size. On the picture is single QD imaged, determining the setup resolution to be of ~ 300 nm. (b) Demonstration of the possibility of the follow-up subscans (enlarging from right to left). (c) Luminescence spectrum from ND particles deposited on glass substrate. Image shows raw data of single scan.

### Acknowledgment

This work acknowledges support of the following grants: GAČR 14\_05053S and OP VK grant CZ.1.07/2.3.00/20.0306

## 4.2. Production of fluorescent nanodiamonds with a narrower emission intensity distribution

This work has been published in **Carbon** journal (**IF = 6.198**) and parts of the article are reprinted here with changes. Authors of the work are: J. Stursa, J. Havlik, V. Petrakova, M. Gulka, J. Ralis, V. Zach, Z. Pulec, S. A. Zargaleh, M. Ledvina, M. Nesladek, F. Treussart and P. Cigler. The aim of this work is to develop novel irradiation method used to create vacancies in Ib nanodiamonds (after subsequent annealing, these vacancies migrate and form NV center with nitrogen defects). Current methods employ pellet target that creates only a fraction of luminescence particles. Here, by using a liquid target irradiation, particles are continuously agitated due to the thermal convection and thus the irradiation is more homogeneous. My share of work involves optical characterization of the nanodiamonds created by both pellet and liquid target irradiation. Using Raman spectroscopy, I was determining  $sp^2/sp^3$  ratio change to determine which method causes less lattice damage (characterized by the graphitization of the  $sp^3$  diamond). It has been shown that liquid target NDs are better protected from graphitization than pellet target NDs. This can be explained by the fact, that in pellet irradiation, diamond lattice damage is caused by local sample overheating, whereas in aqueous irradiation, this effect is decreased due to the water solution and particle agitation. Further, I was evaluating the spectral and intensity change of NV-related photoluminescence. I have demonstrated that liquid and pellet target irradiations yield identical ensemble photoluminescence spectra with the same ratio of the negatively charged  $NV^-$  over the neutral form  $NV^0$  as identified from their zero-phonon lines. All other work was done by remaining authors of the paper. ND irradiation was executed at Nuclear Physics Institute AS CR, v.v.i., Rez near Prague and chemical modification of ND was carried out at Institute of Organic Chemistry and Biochemistry AS CR, v.v.i., Prague without my contribution.

### 4.2.1. Abstract

Fluorescent diamond nanocrystals attract a growing interest for a broad range of applications, from biolabeling and single particle tracking, to nanoscale magnetic field sensing. Their fluorescence origins from nitrogen-vacancy (NV) color centres created within synthetic diamond nanoparticles by the association of pre-existing nitrogen impurities and vacancies through high-temperature annealing. Vacancies are generated by high-energy particle (electron, proton, or helium ion) beam irradiation. Up to now, diamond nanocrystals were irradiated as dry powder in a container or deposited as a thin layer on a flat substrate depending on the type

of irradiating particles and their energy. However, these techniques suffer from intrinsic inhomogeneities: the fluence may vary over the whole sample area, as well as the thickness and density of the nanodiamond layer. Here a novel approach based on direct irradiation of nanodiamonds in aqueous colloidal suspension by high-energy protons is presented. This approach results in a larger fraction of fluorescent particles, with a more homogenous distribution of nitrogen-vacancy centres per particle and lower lattice damages compared to dry powder irradiation.

#### 4.2.2. Introduction

Nanodiamond (ND) is a cellpatible carbon nanomaterial recently introduced as very useful platform for construction of various types of nanoprobes and quantum nanosensors for optical (99) and biomedical (14) applications. ND can accommodate lattice point defects, the negative nitrogen-vacancy ( $NV^-$ ) centres having an electronic spin resonance between the triplet ground state sublevels that can be detected optically (100). The energies of these sublevels being sensitive to external magnetic fields, the NV centres in ND has prospects as a nanoscale magnetic field sensor (96). These remarkable properties, together with the perfect photostability of NV centres fluorescence, its absence of photoblinking for nanocrystals with diameters bigger than 5 nm (101) and emission wavelength in near-infrared region (low background in biological environment) (102) enabled high impact applications in particular in biomedical domain (3). Fluorescent ND have been proposed for real-time sensing of voltage-gated ion channels (103) and as chemo-bio sensors in cells (4). They have been also already used as detectors of very low concentrations of paramagnetic ions (104), for drug delivery systems (105) and cell targeting (106).

NV centres are found as rare defects in synthetic diamond owing to the presence of nitrogen impurities at concentration of 100-200 ppm, and of rare vacancies. However, as one goes to nanometer sizes (<20 nm) the fraction of ND naturally containing at least one NV centre becomes smaller than 1% (107). To increase this fraction and/or the concentration of NV centres into them, one needs to generate more vacancies, which is done by irradiation of the diamond with high-energy particles (i.e. alpha particles, protons and electrons). After irradiation, the ND is annealed in inert atmosphere or in vacuum (47). In this process, crystal lattice vacancies created by irradiation thermally recombine with naturally occurring nitrogen impurities (7). Despite the fact that demand for fluorescent NDs is rapidly growing, the available procedures for creating NV centres in materials are limited to solid state techniques,

which produce characteristic non-homogeneous distribution of fluorescence centres among individual ND particles (108). Here a novel approach based on direct irradiation of NDs in aqueous colloidal solution by high-energy protons is presented. It is shown that fluorescent NDs prepared this way contain a larger fraction of fluorescent particles, with a more homogenous distribution of NV centres per particle and lower lattice damages compared to NDs irradiated in the ND pellet state.

High-energy particles interact with the solid matter in two main ways: they knock atoms off their lattice positions, and if they are charged, they also ionize the material by scattering the electrons. Displaced atoms with sufficient energy may also collide with surrounding atoms causing a cascade of damages of the lattice. At higher, relativistic, energies the accelerated particles may exceed Coulombic barrier of the nucleus and interact in a non-elastic ways (109). Particles with larger mass, such as protons or alpha-particles, are scattered by the nuclei transferring enough energy to cause a cascade of collision events which result in creation of lattice vacancies (110). The number of vacancies created in the diamond increases as the hadron particles slow down. Most of the damage is therefore caused at the end of the particle path. The particle range in the material is determined by their energy, mass and charge, and by the composition of the material and its density. The number of vacancies modeled for irradiation of NDs in a compressed ND pellet are depicted in Figure 24.

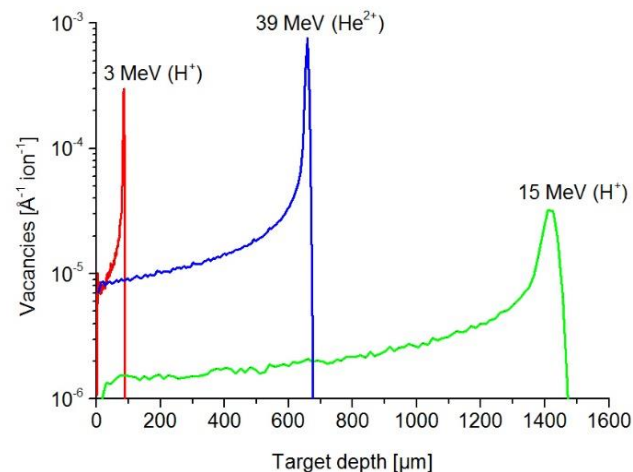


Figure 24: Number of lattice vacancies produced by  $H^+$  and alpha particles of various energies in the compressed ND pellet with the density  $2.00 \text{ g/cm}^3$ . The simulation was performed using SRIM (Stopping and Range of Ions in Matter) software.

The defect production rate for irradiation of diamond depends on the type of particles, their energy and irradiation temperature. Experimental defect production rate for electron irradiation of 1 MeV energy is 0,1-0,25 vacancies  $\text{cm}^{-1}$  per particle at room temperature (111). Calculated defect production rates for heavier particles are generally higher (1,1  $\pm$  0,5 vacancies  $\text{cm}^{-1}$  for proton of 1 MeV energy and 9  $\pm$  4 vacancies  $\text{cm}^{-1}$  for  $\alpha$ -particle) (112). On the other hand, the lattice damage production efficiency of gamma irradiation is 100 times lower compared to electron irradiation (113). The amount of produced vacancies also strongly depends on particles energy. The number of produced vacancies by energy = 10 MeV electrons is about 20 times higher compared to energy = 1 MeV electrons (110).

#### 4.2.3. Methods and materials

Commercially available synthetic NDs produced by high pressure high temperature method with size <50 nm (MSY 0e0.05, Microdiamant, Switzerland) were used. The particles were oxidized in air at 510 °C for 5 hours in a tube furnace (Thermolyne 21100). The NDs were subsequently treated with a mixture of  $\text{HNO}_3$  and  $\text{H}_2\text{SO}_4$  (85 °C, 3 days).

ND pellet target was prepared by pressing NDs powder into the target backplate using purpose-made press. The backplate is a duralumin disc with a hollow part in the middle, into which the ND powder is molded at the pressure of 5.88 MPa. The NDs layer thickness is chosen to optimally stop accelerated particles in the material. The average density of the material after molding is 2.0  $\text{g}/\text{cm}^3$ . Targets were molded with a 150 mg portion for proton irradiation. Samples were irradiated with a 14.9 MeV proton beam extracted from the isochronous cyclotron U-120M for 125 min (fluence  $5.0 \cdot 10^{16} \text{ H}^+/\text{cm}^2$ ). The overall dose of protons for the pellet target was  $2.52 \cdot 10^{16}$ .

For liquid ND irradiation, the chamber was filled with 2.4 ml of 5% weight ND aqueous colloidal solution. Filling and processing of the irradiated solution was remote-controlled. The sample was irradiated with a 16.0 MeV proton beam extracted from the isochronous cyclotron U-120M for 270 min (fluence  $6.6 \cdot 10^{17} \text{ H}^+/\text{ml}$ ). The overall dose of protons recalculated for 5% of ND particles present in liquid target was  $7.93 \cdot 10^{16}$ . During irradiation, there was a pressure increase in the chamber. To avoid exceeding the maximal system operating pressure during lengthy irradiation with high currents, the solution was degassed before irradiation and the system was filled with helium gas. After irradiation, the ND solution was pushed out of the chamber with helium gas.

All samples (pellet and liquid target ones) were annealed at 900 °C for 1 hour in argon atmosphere followed by air oxidation at 510 °C for 4 hours at atmospheric pressure in a furnace tube (Thermolyne 21100) calibrated with an external thermocouple (Testo AG 1009).

Before Raman and photoluminescence measurements, all samples were lyophilized from water and diluted in deionized water to a concentration of 10 mg/ml with a high-power ultrasonic horn (Hielscher UP400S, Sonotrode H3) using 400 W at a 1:1 (on/off) cycle for 30 min under liquid cooling. The samples were prepared by drop-casting of the aqueous dispersion of NDs on the polished silicon wafer. Raman and luminescence spectra were measured using a Renishaw InVia Raman Microscope; the excitation wavelength was 514 nm (luminescence measurements) and 325 nm (Raman measurements) with 15 mW laser power, x20 objective. The exposure time was 6 s, 10 accumulations. Twenty measurements were taken for each sample. The Raman and luminescence spectra were taken at room temperature.

The sizes of the spincoated NDs were estimated with an atomic force microscope (MFP e 3D-BIO, Asylum Research, USA) placed on top of a homemade fluorescence confocal microscope used to locate fNDs (more details in Ref. [58]). The AFM enabled us to measure the height (i.e., the vertical dimension) of the ND with a resolution of approximately 1 nm, but the lateral resolution was practically limited to about 80 nm due to the finite radius of the curvature of the AFM tip. The confocal inverted fluorescence microscope has a single NV color center sensitivity, and therefore provides a means to determine whether each ND observed by AFM contains at least one NV center.

#### 4.2.4. Results and discussions

The irradiation of a ND pellet target introduces serious technological challenges related to target surface irradiation homogeneity and the particle range uncertainty. Problems with inhomogeneous surface irradiation dose are caused mainly by the shape of the radiation beam. After acceleration and extraction from the cyclotron the ions are directed on the target by ion-optical elements. In order to scale up the mass of irradiated NDs, uniform irradiation of ND pellet with a diameter of 8 - 10 mm is needed. For that reason the particle beam is defocused and consequently collimated just before hitting the target. Despite this beam adjustment the particle density on the target surface may vary in the range of 20% due to beam distribution of particle density in the beam cross-section.

The uncertainty in the range of particles is mainly caused by inhomogeneous material density and by particle energy spread. The ND pellet is prepared by mechanical pressing the ND powder, which cannot secure the strictly homogeneous density of the layer. Moreover, the cyclotron beam is not monoenergetic. The energy spread of the  $H^+$  beam with mean energy 15 MeV is approximately  $\pm 0,25$  MeV, which corresponds to difference in particle ranges from 1,37 mm to 1,45 mm. Due to these uncertainties the accelerated particles are not stopped at the same depth during penetration of the ND layer and some of them can leave the ND layer. These problems have been identified from radiograms recorded after ND pellet irradiation. Indeed the inhomogeneities result in a complex spatial distribution of stopping powers and subsequently of the amount of the created vacancies. Although it is possible to repeat irradiation procedures several times with homogenization and re-deposition steps on the target between every irradiation (3), this approach lengthens the whole preparation.

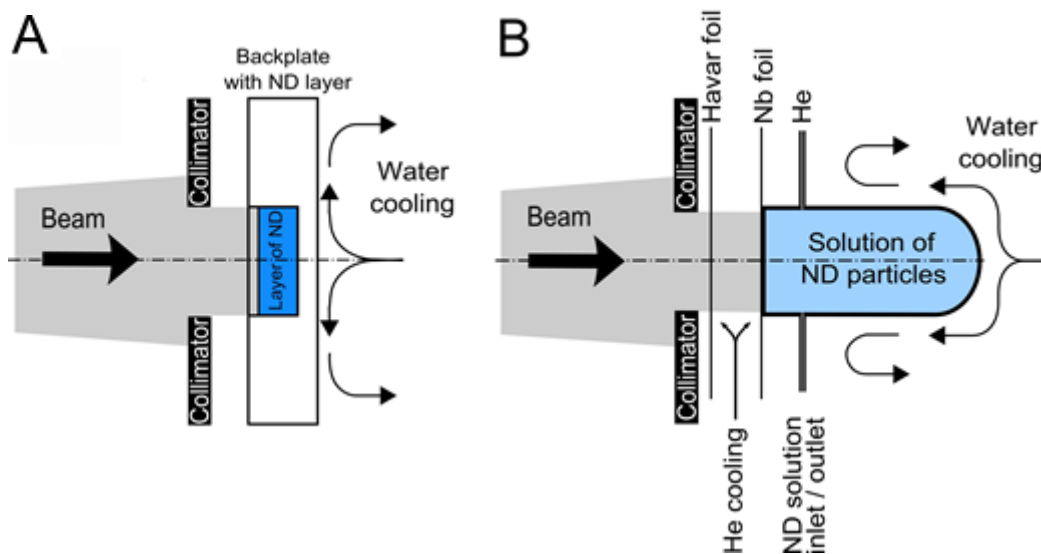


Figure 25: Schematics of ND pellet target (A) and liquid target (B).

In order to limit the influence of inhomogeneous irradiation and sample preparations, a target enabling direct irradiation of ND aqueous colloidal solution was constructed. The main part of target assembly is a water-cooled niobium chamber with niobium entrance foil cooled with helium and an integrated collimator at the beam entrance (Figure 25). The target is separated from the ion-beam line by a thin Havar foil. Unlike in the ND-pellet target case, the inherent thermal convection contributes here to continuous agitation of the particles during the irradiation which is reflected in better irradiation homogeneity. Moreover, the irradiated

material is diluted in water which reduces the local heat accumulation. It is expected that both these factors will contribute to decrease of the diamond lattice damage caused by local sample overheating followed typically by strong surface graphitization.

I have focused on revealing the different irradiation damages of the diamond lattice for both types of targets. From the lower G band intensity of Raman spectra (Figure 26) I infer that liquid target NDs are more protected from graphitization than pellet target ones. After high temperature annealing which naturally causes a strong graphitization of NDs, the content of  $sp^2$  carbon in both samples is almost the same. However, after air oxidation at 510 °C the sample from liquid target has finally a slightly better  $sp^3$  purity.

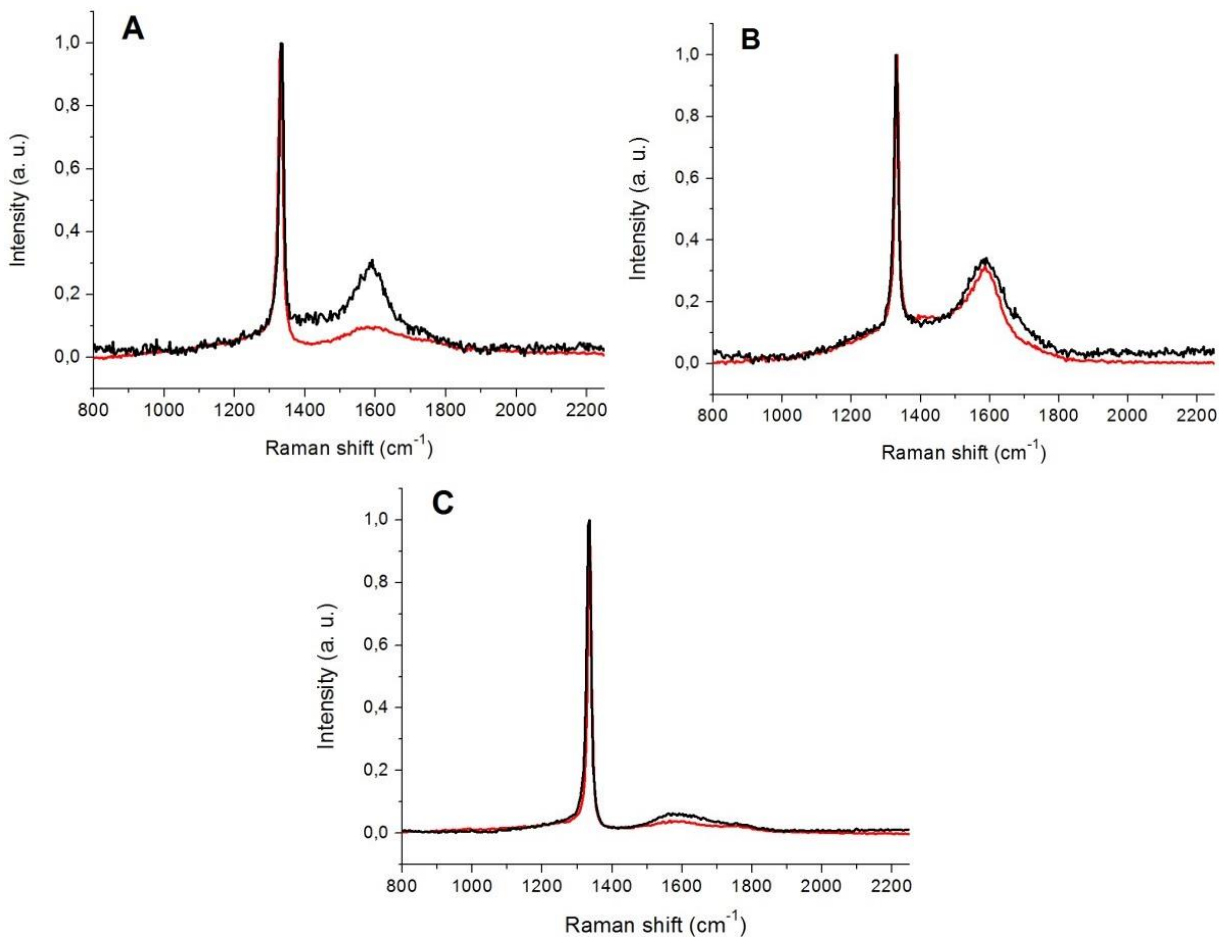


Figure 26: Raman spectra of NDs from pellet target (black) and liquid target (red). Spectra were measured after irradiation (A), after annealing (B) and after oxidation (C). The intensity of spectra is normalized to the diamond Raman band ( $1332\text{ cm}^{-1}$ ). The G-band ( $1583\text{ cm}^{-1}$ ) originates from graphite-like inclusions consisting of  $sp^2$ -hybridized carbon atoms and shows the presence of defective graphite structures (114).

The average fluorescence intensity of produced NDs depends on several factors: the fraction of fluorescence nanodiamonds (FND), the number of NV centres created in

nanodiamonds, and the purity of the ND surface considering the fact that surface graphitic shell reduces luminescence intensity (47). Fluorescence spectra shown in Figure 27 represent the normalized average fluorescence intensity of the of FND solution (not individual particles) as measured with a Raman microscope. The intensity was normalized to the diamond Raman peak. Both samples, NDs from pellet target and from liquid target, show  $NV^-$  (ZPL at 638 nm) and  $NV^0$  (ZPL at 575 nm) luminescence followed by typical phonon side bands structures. The average intensity is comparable in both samples. As both sets of samples were treated with exactly the same post-annealing oxidative procedure, I can neglect the effect of surface purity to the overall luminescence intensity.

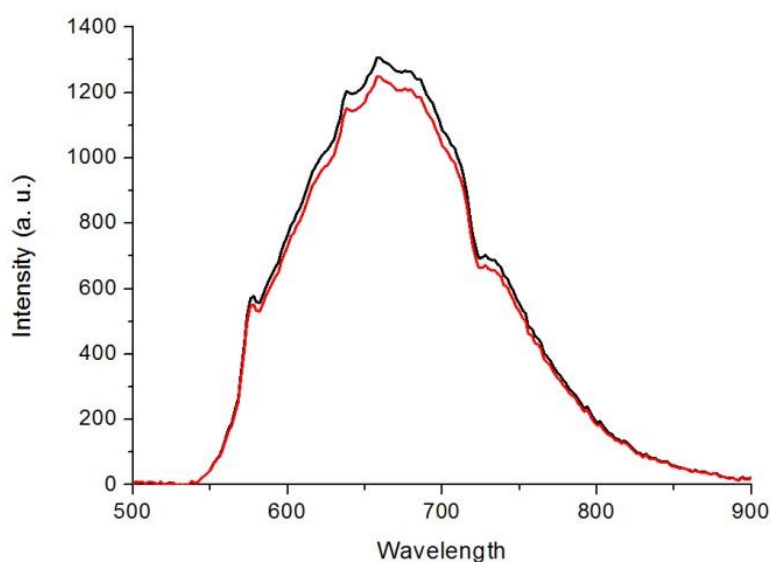


Figure 27: Luminescence spectra of FNDs normalized to diamond Raman peak for pellet (red) and liquid target (black).

In order to determine the fraction of fluorescent particles in the two types of irradiated samples, measurements at the single particle level of both the size and fluorescence intensity of each ND were performed. For that ND suspensions were first spin-coated on a quartz coverslips after appropriate dilution to achieve a surface density of about one ND per micrometer square. The samples were then raster scanned and the NDs heights was measured with an atomic force microscope (AFM) installed on a homemade confocal microscopy allowing to simultaneously record the fluorescence intensity of each ND. From these data, a fraction of 77% (135 FNDs among a total of 175 NDs detected by AFM) of fluorescent NDs in the liquid target sample,

and only 24% (225 FNDs among a total of 950 NDs detected by AFM) fluorescent particles in the solid-state target was determined (Table 1).

Table 1: Single particle analysis of the fluorescence intensity for pellet and liquid target sample.

	Pellet target	Liquid target
Fraction of FND (%)	24	77
Mean fluorescence intensity (kcounts/s)	$122 \pm 8$	$66 \pm 7$
Median intensity (kcounts/s)	75	38
Standard deviation (kcounts/s)	123	80

The fluorescence intensity distributions of individual fluorescent NDs in both samples is shown in Figure 28. The solid target has higher mean brightness compared to the liquid target and a larger standard deviation too. This can be explained by the fact that some stationary particles of the pellet target experience a larger radiation dose compared to non-stationary particle in solution, leading to the creation of a larger concentration of vacancies for some NDs. On the contrary, in the liquid target the effective dose per particle for the same irradiation conditions is smaller but also more homogeneous, owing to random thermal motion of particles in the solution, leading to a smaller mean fluorescence intensity value together with a narrower distribution (see standard deviations in Table 1).

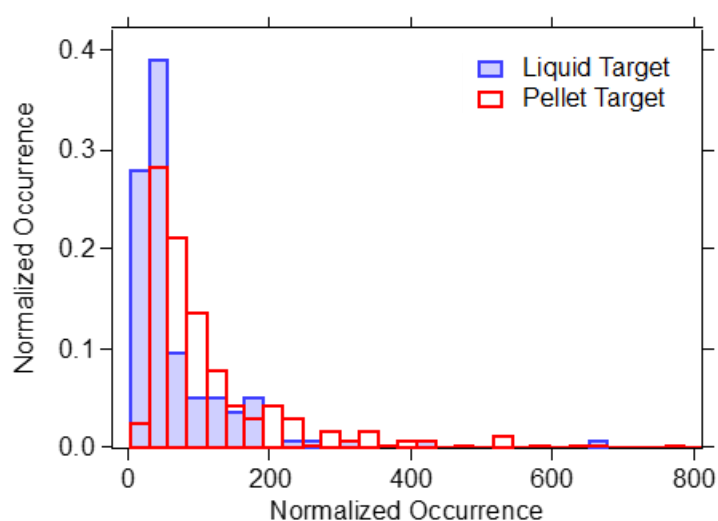


Figure 28: Normalized distribution of single FND fluorescence intensity as measured by confocal fluorescence microscopy for solid-state target (red) and liquid target (blue plain bars). Excitation laser wavelength: 532 nm, laser power: 200  $\mu$ W.

To confirm that the single particle fluorescence intensity distribution do correspond to different fluorescent nanodiamond populations, a two samples Wilcoxon-Mann-Whitney rank test was performed, which tests the null hypothesis that two sets of data are from the same population against an alternative hypothesis. Such a test is well adapted to compare non normal distributions. The test yielded a very low two-tail probability of  $P = 1.8 \times 10^{-15}$  (two sets of data are usually considered with a very high confidence from different population when  $P < 0,001$ ). Therefore, the hypothesis that the two sets of fluorescence intensity data are from the same FND population is rejected.

#### 4.2.5. Conclusion

It has been shown that irradiation of diamond nanocrystals in aqueous suspension yields a more homogeneous distribution of NV color centre per particles than solid phase pellet irradiation with a three-fold larger fraction of fluorescent ND, which is important for most applications, e.g. bioimaging. Moreover, it is foreseen that lower fluence irradiation in a liquid target followed by high temperature annealing and air oxidation can also be used to produce fluorescent nanodiamonds containing exactly one NV centre with a high yield, improving recently reported approach based solely on annealing and air oxidation (115). Such particles are essential for magnetic field sensing relying on the optical detection of electron spin resonance of  $NV^-$  color centre.

#### **Acknowledgement**

The work was supported by GAČR project P108/12/0640. Irradiations of NDs were carried out at the CANAM infrastructure of the NPI ASCR Rez supported through MŠMT project No. LM2011019.

### 4.3. Benchtop Fluorination of Fluorescent Nanodiamonds on a Preparative Scale: Toward Unusually Hydrophilic Bright Particles

This work has been published in **Advanced Functional Materials** journal (IF = 11.38) and is reprinted here with changes. Authors of the work are: J. Havlik, H. Raabova, M. Gulka, V. Petrakova, M. Krecmarova, V. Masek, P. Lousa, J. Stursa, H.-G. Boyen, M. Nesladek, and P. Cigler. The goal of this work is a creation of fluorescent NDs with fluorinated surface. It has been shown that fluorination stabilizes the NV luminescence by shifting the relative Fermi level for the near-surface NVs. However recent approaches are harsh and complex and yield hydrophobic interfaces with difficult dispersibility in aqueous environments. Here, mild fluorination method is presented, which produces a highly hydrophilic NDs. I have contributed to this work by optical characterization of the nanodiamonds, determining  $sp^2/sp^3$  ratio change and evaluation of the spectral properties and intensity change of NV-related photoluminescence. In the process of development of the fluorination method, this was an important step as I was able to demonstrate, whether the proposed fluorination procedures damaged the ND lattice and whether the surface coverage with Fluor was sufficient to boost the NV related photoluminescence. I have shown that the fluorination method presented here is non-destructive and yields fluorinated NDs with increase in fluorescent emission intensity of the  $NV^-$  state. All other work was done by remaining authors of the paper. ND irradiation was executed at the CANAM infrastructure of Nuclear Physics Institute AS CR, v.v.i., Rez near Prague and chemical modification of ND was carried out at Institute of Organic Chemistry and Biochemistry AS CR, v.v.i., Prague without my contribution.

#### 4.3.1. Abstract

A Fluorination of diamonds modulates their optical and electromagnetic properties and creates surfaces with increased hydrophobicity. In addition, fluorination of diamonds and nanodiamonds has been recently shown to stabilize fluorescent nitrogen-vacancy centres, which can serve as extremely sensitive single atomic defects in a vast range of sensing applications from quantum physics to high-resolution biological imaging. Traditionally, fluorination of carbon nanomaterials has been achieved using harsh and complex experimental conditions, creating hydrophobic interfaces with difficult dispersibility in aqueous environments. Here, a mild benchtop approach to nanodiamond fluorination is described using selective  $Ag^+$ -catalyzed radical substitution of surface carboxyls for fluorine. In contrast to other approaches, this high-yielding procedure does not etch diamond carbons and produces a highly

hydrophilic interface with mixed C–F and C–OH termination. This dual functionalization of nanodiamonds suppresses detrimental hydrophobic interactions that would lead to colloidal destabilization of nanodiamonds. It is also demonstrated that even a relatively low surface density of fluorine contributes to stabilization of negatively charged nitrogen-vacancy centres and boosts their fluorescence. The simultaneous control of the surface hydrophilicity and the fluorescence of nitrogen-vacancy centres is an important issue enabling direct application of fluorescent nanodiamonds as nanosensors for quantum optical and magnetometry measurements operated in biological environment.

#### 4.3.2. Introduction

In the past two decades, fluorinated carbon nanomaterials (CNMs) have attracted considerable interest because of their potential applications in electronic and optical devices. Introduction of a C F bond confers a new quality to CNMs by changing and shifting their optical, electromagnetic, and mechanical properties (116), specifically by opening of a bandgap (117). Moreover, a fluorine-terminated surface can serve as an intermediate for subsequent modification by other reagents (118) and for structural control during synthesis, such as cutting of nanotubes (119). Fluorination of graphene (118), carbon nanotubes (120), and nano-onions (121) has been achieved using elemental fluorine. Alternative techniques, such as CF<sub>4</sub> plasma treatment and reaction with XeF<sub>2</sub>, have been used to fluorinate carbon nanotubes (122) and graphene, (116) respectively. However, fluorination of nanodiamonds (NDs) is a special chemical challenge because of the fundamentally different chemical nature of NDs and the low reactivity of the sp<sup>3</sup>-diamond surface compared to sp<sup>2</sup>-based CNM relatives.

Here, a preparative and high-yielding method for one-step fluorination of NDs is described that can be performed on a benchtop using modest synthetic equipment. Our interest in fluorination of NDs arose from recent studies (123; 124) showing that fluorination of the diamond surface can be used to stabilize negatively charged nitrogen-vacancy (NV<sup>-</sup>) centres located close to the surface. These atomic defects in the diamond lattice have been thoroughly studied in the past two decades due to their unique applications as single photon emitters (125), ultrasensitive magnetic, (65) and electric (80) field sensors, chemical probes (5), and qubits (126). NV centre fluorescence depends on the electron spin state, which enables coherent manipulation of single NVs (55) and measurement of optically (127) or photoelectrically (128) detected magnetic resonance of single spins. The NV<sup>-</sup> state is the actual “sensing species” and stabilization and boosting of its photoemission thus represent a critical milestone in all the

above-mentioned applications. Covalent attachment of highly electronegative fluorine can serve as a pathway to bend the conduction and valence bands in the diamond downward, changing the position of the ground state of NV centres relative to the Fermi level. This leads to stabilization of the  $NV^-$  charge state and in turn boosts the brightness of diamond nanoparticles. Highly bright and stable NDs are indeed essential for high-resolution biomedical imaging applications.

The current fluorination approaches for  $sp^3$ -diamond surfaces typically involve handling of highly corrosive gases (atomic or molecular fluorine, HF,  $ClF_3$ ) under harsh treatment conditions (129) and utilize technically demanding and potentially hazardous setups, such as a fluorine line (129), fluorine containing plasmas (e.g.,  $CF_4$ ,  $SF_6$ ) (130), ultrahigh-vacuum fluorine atomic beams (131), and X-ray irradiation (132). In addition to the  $sp^3$ -diamond-directed procedures, the  $sp^2$ -structures on so-called detonation NDs have been fluorinated similarly - using molecular (133) or plasma-generated fluorine (134). Our approach is based on a mild fluorination procedure that can be performed on a multigram scale at a benchtop without special equipment and safety requirements. The procedure involves  $Ag^+$ -catalyzed selective substitution of diamond carboxyls for fluorine using Selectfluor reagent (135). Here, fluorination of oxidized carboxylated fluorescent NDs (FNDs) is described and a detailed characterization of the fluorinated FNDs is presented. Moreover, I demonstrate that this type of fluorinated ND surface manipulates the electronic structure of the surface of diamond nanocrystals, which results in changes to the fluorescence of nitrogen-vacancy centres present in NDs.

#### 4.3.3. Methods and materials

NDs containing  $\approx 100$ – $200$  ppm of natural nitrogen impurities were supplied by Microdiamant Switzerland (MSY 0-0.05). NDs were oxidized by air in a Thermolyne 21100 tube furnace at  $510$  °C for 5 h and subsequently treated with a mixture of  $HNO_3$  and  $H_2SO_4$  ( $90$  °C, 3 d),  $1$  M NaOH ( $80$  °C, 1 h), and  $1$  M HCl ( $80$  °C, 1 h). Between treatments, NDs were separated by centrifugation at 5000 rcf for 20 min. After HCl treatment, diamonds were centrifuged four times (5000 rcf, 20 min; 7000 rcf, 30 min; 20 000 rcf, 30 min; 30 000 rcf 30 min) with deionized water to obtain a stable colloid and freeze-dried. Purified ND powder (160 mg) was pressed in an aluminum target holder and irradiated with a 14.8 MeV proton beam extracted from the isochronous cyclotron U-120M for 125 min (fluence  $5.02 \times 10^{16} \text{ cm}^{-2}$ ), as previously described (7). The irradiated material was annealed at  $900$  °C for 1 h in argon

atmosphere and subsequently oxidized in air for 5 h at 510 °C. The NDs were then treated with a mixture of HNO<sub>3</sub> and HF in a Teflon beaker on a hotplate (160 °C, 2 d), washed with water, 1 M NaOH, water again, and 1 M HCl. The precipitate was washed five times with water and freeze-dried.

Oxidized FND particles (250 mg) were dissolved in water (250 mL) and sonicated with a probe (ColeParmer, 750 W) for 30 min. The colloidal solution was placed in a 500 mL flask with a septum. The flask was evacuated and blown through with argon for 30 min. AgNO<sub>3</sub> (425 mg) and Selectfluor (8.85 g) were placed in 500 mL flask with a septum and evacuated and refilled with argon three times. A deaerated FND solution (250 mL) was then added under inert atmosphere via cannula, and the reaction mixture was stirred in various conditions (see Table 2) under an argon atmosphere. The resulting mixture was cooled to room temperature and separated by centrifugation (4000 g, 20 min) and washed with water. The sediment was dispersed in aqueous KCN (1%, 500 mL) slowly stirred overnight. The suspension was separated by centrifugation. The KCN-containing supernatant was disposed of by adding it to an H<sub>2</sub>O<sub>2</sub> solution (30%, 500 mL). Sedimented FNDs were dispersed in ammonia solution (24%, 500 mL) and precipitated by addition of brine (25 mL). The precipitate was washed once with 1 M HCl and five times with water and freeze-dried, providing 216 mg of the fluorinated FND.

*Table 2: Reaction conditions, results of elemental analysis of NDs, and calculated reaction conversions of fluorination.*

<b>Reaction temperature</b> (°C)	<b>Fluorine content</b> (wt. %)		<b>Reaction conversion</b> (%)	
	1 day	2 days	1 day	2 days
55	0.09	0.11	65	80
95	0.11	0.13	80	94

X-Ray Photoelectron Spectroscopy (XPS) was performed by drop-casting aqueous FND solutions onto Si wafers and loading them immediately after drying into a commercial electron spectrometer (PHI 5600LS). Samples for TEM were prepared similarly as described elsewhere (136). TEM Image Analysis: Analysis of particle size distributions was performed with ImageJ software using a previously described procedure (136). The content of fluorine was determined by ion-exchange chromatography and the data were evaluated with CSW32 (Dataapex) chromatography software. DLS and zeta potentials were recorded with a Zetasizer Nano ZS

system (Malvern instrument) at room temperature. Sample concentrations were  $1 \text{ mg mL}^{-1}$  in deionized water.

The ensemble fluorescence spectra of NDs were measured using Raman iHR320 imaging spectrometer (HORIBA JOBIN YVON) with  $600 \text{ gr mm}^{-1}$  grating and paired with liquid nitrogen-cooled  $2048 \times 512$  pixel CCD detector Symphony (HORIBA JOBIN YVON). Verdi V5 (Coherent) 532 nm DPSS laser served as the source of excitation radiation. The radiant power on the sample was 50 mW. Solutions of NDs diluted in deionized water were sonicated using high-power ultrasonic horn (Hielscher UP400S, Sonotrode H3) set to 400 W and 1:1 (on/off) cycle for 30 min under liquid cooling. Stable colloidal solutions ( $1 \text{ mg mL}^{-1}$ ) were sonicated in a bath for 1 min before each measurement. For each spectral window 16 accumulations with 200 ms integration time were acquired. For each sample three independent measurements were done and averaged.

The photoluminescence maps were measured on luminescence-free quartz cover slips cleaned in ethanol before the use. Droplet of colloidal solutions of oxidized and fluorinated nanodiamond particles ( $1 \text{ }\mu\text{L}$ ,  $0.1 \text{ mg mL}^{-1}$ ) was applied using micropipette to a cover slip and dried under infrared lamp. The ND particles were dispersed rather homogeneously over the spot after drying the microdroplet with accumulation of particles at the edges of the microdroplet dried-up spot. Luminescence measurements were performed in the centre of the dried microdroplet spot. 20 microdroplets from suspension of each oxidized ND and fluorinated ND were produced. To measure photoluminescence (PL), a home-made confocal setup designed specifically for studying NV color centres in diamond was made. The PL was excited with 500 mW Gem laser from Laser Quantum producing 532 nm CW excitation, directed by Gaussian beam optics to Olympus 40 $\times$  UPLSAPO 40 $\times$ 2 air objective with N.A. 0.95 and working distance of 180 micrometers. The lateral resolution of the confocal setup was 350 nm. The laser power was adjusted to 2.5 mW. The PL counts were detected using Excelitas single photon counter. The number of counts corresponding to a single NV centre under laser power saturation was determined using single NV centres in quantum grade single crystal diamond (Element Six) located 15 micrometer from the surface of diamond and located in the crystal bulk. The number of PL counts corresponding to a single NV centre in ND on the quartz surface was recalculated using the geometry of the objective and the index of refraction of diamond. The maps were recorded by scanning the stage on the area of  $10 \times 10 \text{ }\mu\text{m}$ . From the detected intensity, it was established that the PL counts corresponding to ND particles exhibited counts corresponding digital multiples of single NV centre count, matching also to the correction factor for NV counts in the bulk of single crystal diamond and ND on a surface of quartz.

#### 4.3.4. Results and discussions

##### **Fluorination procedure**

Fluorination causes significant changes in solvation of the diamond interface (137). Fluorine bound to diamond carbon atoms acts as a poor hydrogen-bond acceptor (in contrast to fluoride anions in solution) and weakens the overall hydrogen bonding network formed at the solid–liquid interface (138). Hydrophobicity caused by a high level of surface diamond coverage with fluorine can be even higher than for hydrogenated surfaces (as quantified by contact angle measurements) and typically results in increased solubility of fluorinated NDs in organic solvents (137). For biological applications, hydrophobicity and poor solvation in water are unwanted; the nanobiointerface should ideally be hydrophilic. For example, cells cannot adhere either to hydrogenated or highly fluorinated diamond surfaces, whereas oxidized diamond surfaces promote their adhesion (135). To circumvent these drawbacks of fluorine chemistry, it was focused on preparing a diamond surface with dual functionality involving both fluorine and hydrophilic oxygen-containing groups. Oxidized bulk diamond single crystals and NDs prepared by high-pressure high temperature (HPHT) or by the chemical vapor deposition approach predominantly bear hydroxy or ether moieties, while carbonyl-containing groups (including carboxyls) are much less frequent. In a recent study (139), the range of molar fraction of surface carboxyls obtained by air oxidation of these materials was estimated to be  $\approx$  2% - 3%. Although treatment with mineral acids can further increase the fraction of carboxyls, the highest reported values are 4.7% and 7% (140; 141).

For partial fluorination of the oxidized diamond surface, advantage of a recently described selective substitution of carboxyls for fluorine was used (135). It was expected to reach maximally  $\approx$  7% coverage of surface carbons with fluorine, while the rest of the surface would remain predominantly covered with hydroxy or ether moieties. It was hypothesized that this controlled amount of introduced fluorine can affect the electronic behavior of the nanocrystal and influence the population of  $NV^-$  centres. The hydroxy groups and unreacted carboxyls would keep the fluorinated NDs hydrophilic and colloidally stable in an aqueous environment. The silver-catalyzed decarboxylative fluorination procedure uses the electrophilic fluorinating reagent 1-chloromethyl-4-fluoro-1,4-diazoniabicyclo[2.2.2]octane bis(tetrafluoroborate) ( $F-TEDA^+ BF_4^-$  or Selectfluor). Compared to other fluorodecarboxylative approaches, this procedure is unique in its ease, mild reaction conditions, chemoselectivity, and extensive substrate scope (including extremely sterically hindered structures). According to the recently described reaction mechanism (142), Ag(I) is oxidized to Ag(II) by  $F-TEDA^+$  to generate  $TEDA^{+\bullet}$  radical cation (Figure 29a). The resulting Ag(II)

intermediate oxidizes the carboxyl ligand to produce a tertiary alkyl radical on the diamond. Fluorine abstraction from another F-TEDA<sup>+</sup> cation yields the product. To ascertain factors influencing decarboxylative fluorination in a deaerated aqueous dispersion of NDs, the reaction was performed at different temperatures for various reaction times (Table 2).

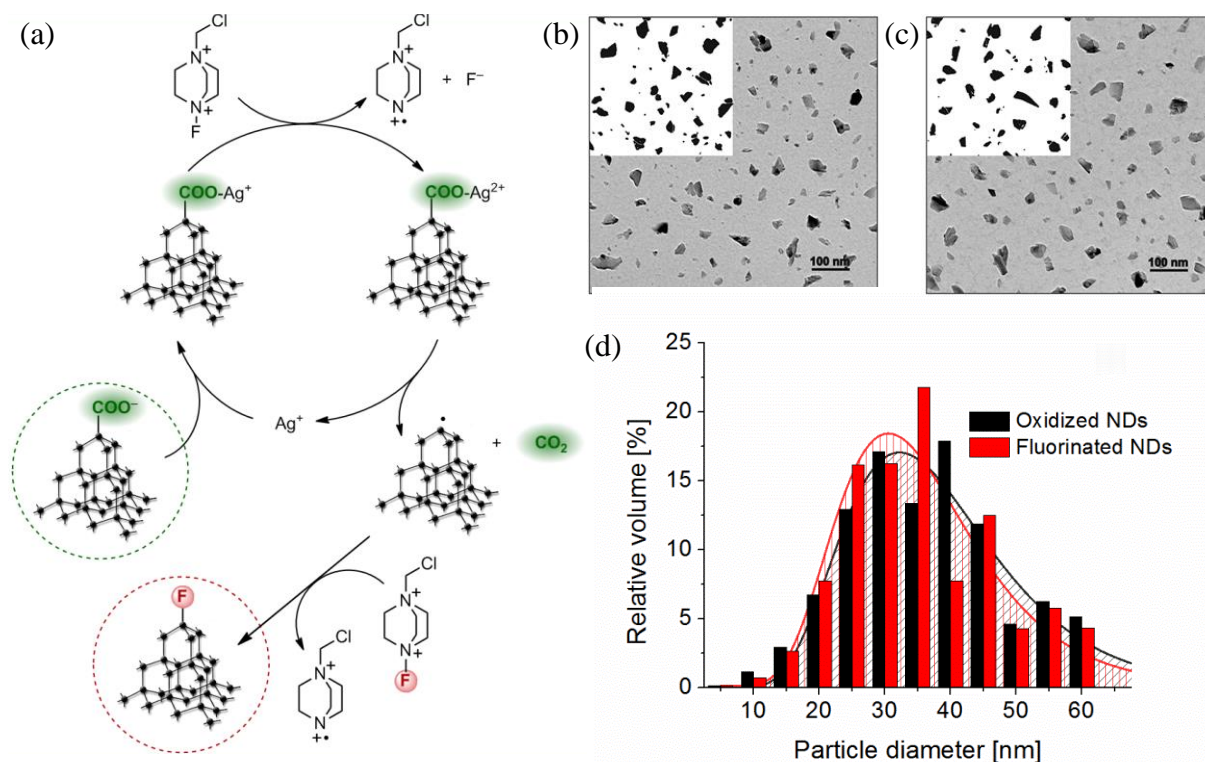


Figure 29: (a) A simplified scheme of the catalytic cycle for decarboxylative fluorination of NDs. The ND is represented by a fragment of the diamond lattice. (b) TEM images of HPHT NDs on carbon coated grids with oxidized surfaces and (c) after fluorination treatment. For illustration, the upper left corner of each image is shown in the binary mode used for image analysis. (d) Volume-weighted distribution histograms of ND sizes. The histograms are fitted with lognormal distribution functions. The estimated modes are at 32 and 31 nm for oxidized and fluorinated NDs, respectively.

### Chemical particle analysis

To analyze the fluorination yields, the samples were combusted in an oxygen atmosphere and analyzed them for fluoride anion content using ion exchange chromatography with suppressed conductivity detection (for an example of a chromatogram). Within the range of conditions tested, it was observed that fluorination is best accomplished after 2 d at 95 °C (Table 2). Extrapolation of the weight percent of fluorine in the material to surface coverage can be based on various models, taking into account the different shapes of particles, their size distribution, and the original surface coverage with carboxyls. For estimation of the maximal theoretical load of fluorine on a perfluorinated surface, it was assumed that the [111] diamond surface and every terminal carbon atom occupied by a carboxylic group are available for

fluorination. The total number of available carbon atoms can be calculated from the size distribution obtained by precise image analysis of transmission electron microscopy (TEM) images of NDs, a method that has been recently developed (136). From volume-weighted histograms of a polydisperse mixture of particles (see Figure 29b-d), it was obtained 3.7 mmol g<sup>-1</sup> surface carbon atoms or theoretically exchangeable carboxyls. For comparison, a similar calculation using a simple spherical model and hydrodynamic radius of 38 nm obtained from dynamic light scattering (DLS) measurements provides a value of 2.7 mmol g<sup>-1</sup>, which underestimates the value obtained from TEM by 27%.

Considering the experimentally determined coverage of NDs with carboxyls as 2% of all [111] surface functionalities (139) and the findings from the TEM image analysis, a maximal total theoretical fluorine content of  $\approx 0.14$  wt % was obtained. The best reaction conversion achieved (calculated for a fluorine content of 0.13 wt%) is therefore 94% (Table 1). Although this calculated yield is indeed affected by the accuracy of the input value of carboxyl content, it nevertheless shows that the fluorination proceeds with a high conversion. For chemical analysis of the near-surface region of the most fluorinated sample (reacted for 2 d at 95 °C), X-ray photoelectron spectroscopy (XPS) was performed. In addition to estimating the efficiency of the surface functionalization route, XPS provides information about the chemical environment of the atomic species by establishing binding energy shifts of appropriate core levels (“chemical shifts”). Figure 30A presents the F1s core level spectrum (open symbols) as acquired on fluorinated NDs. Based on a line shape analysis using a least-squares fitting routine, a single line centered at 687.3 eV is sufficient to describe the experimental data (solid curve). This value agrees well with the position observed earlier for covalent C-F bonds (687.5 eV) (143), thus providing evidence for the stable attachment of fluorine atoms to the nanoparticle surface.

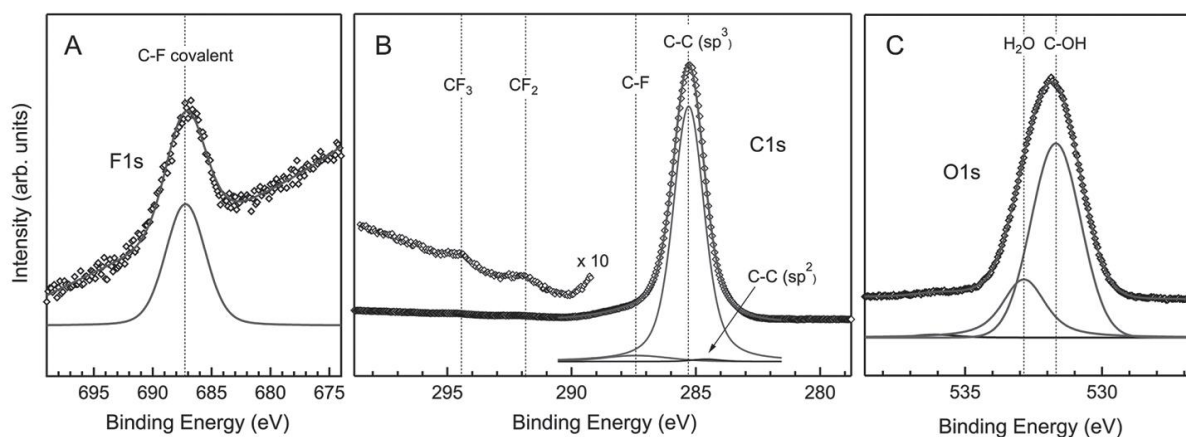


Figure 30: (A) F1s, (B) C1s, and (C) O1s core level spectra (open symbols) of diamond nanoparticles fluorinated according to Scheme 1. Solid lines are the result of a line shape analysis.

In order to derive a more quantitative picture of the successful fluorination, the C1s core level region was analyzed in more detail (Figure 30B). The main peak observed at a binding energy of 285.3 eV can be assigned to photoemission from carbon atoms localized within the diamond lattice. On the high binding energy side, an additional component (shoulder) can be detected at 287.4 eV, representing 4.3% of the total C1s line intensity in the near-surface region. This is followed by very weak components at 291.8 and 294.5 eV, each contributing  $\approx 0.1\%$  to the C1s photoelectron intensity. While the latter two components can be assigned to the presence of negligible amounts of CF<sub>2</sub> and CF<sub>3</sub> at the sample surface, the contribution at 287.4 eV can be attributed to carbon atoms forming C-F covalent bonds (287.2 eV) (143), thus giving additional support for a successful fluorination procedure. On the low binding energy side of the main photoemission line, an additional component at 284.6 eV is required to achieve a reasonable fit, thereby contributing 0.8% to the total C1s line intensity. This weak signal arises from a small amount of sp<sup>2</sup>-bound species at the sample surface.

After establishing the spectral weight of the different carbon species present in the near surface region, the surface coverage of C-F moieties can be estimated using a very simplified model. Assuming the particles to be spherical, the intensity ratio between the main line (representing diamond) and the shoulder at 287.4 eV (representing carbon atoms within C-F bonds) can serve as input for a core/shell model simulation. Briefly, the nanoparticle is divided into a large number of identical cells, each contributing to the photoelectron current an intensity that is affected by the attenuation in cells closer to the surface according to the mean free path within these cells. Taking a mean free path value of 1.9 nm for C1s photoelectrons travelling through both the bulk diamond and the layer of surface carbon atoms covalently bound to fluorine atoms, an effective shell thickness of the affected carbon atoms can be estimated. This

yields an effective thickness of 0.05 nm, which considering the size of carbon atoms in the diamond (0.18 nm), results in the formation of C-F bonds by about 28% of all terminal carbon atoms on the diamond surface. This finally translates into fluorine surface coverage of 9% of the monolayer (assuming each C-F moiety is attached to three C atoms, as shown in Figure 29a) thereby confirming that only part of the surface was functionalized with fluorine as has been aimed for.

To finally prove the nature of dual functionality induced by our procedure (fluorine & hydrophilic oxygen-containing groups), the O1s core level region has been characterized as well (Figure 30C). Here, a line-shape analysis of the experimental spectrum reveals the presence of 2 major components, one positioned at 532.8 eV which can be assigned to adsorbed water and one located at 531.7 eV. This line clearly represents C-OH functionalities. Signals of other types of oxygen-containing groups were not found in the spectra, indicating a predominant fraction of hydroxy groups. Both elemental and XPS analyses provide an evidence for the successful dual functionalization of the ND surface. It was found that decarboxylative fluorination performed under mild conditions proceeds efficiently on a highly sterically hindered substrate, such as ND surface. The achieved fluorine surface coverage corresponds fairly well to the experimentally determined content of carboxylic moieties in starting material (oxidized HPHT NDs), indicating a high conversion of the reaction. The surface termination consists of a smaller fraction of C-F groups, while the rest is covered by C-OH moieties.

### **Colloidal characterization**

The fluorodecarboxylation proceeds solely on carboxyls (142), and it can therefore assumed that the hydroxy groups remain intact during the reaction. Because hydroxy groups are the predominant oxygen-containing moieties on our surfaces (see above), it was tested whether they can ensure the overall hydrophilicity of the partially fluorinated surface and compensate for the hydrophobicity of the terminal C-F groups. The colloidal behavior of oxidized and fluorinated particles in water was investigated using DLS and zeta potential measurements (Figure 31a). Both samples had an average particle diameter of 38 nm with a size distribution characteristic of HPHT NDs (7). Because DLS is extremely sensitive to signs of association and/or aggregation of the scattering particles, and both samples were found indistinguishable with DLS, it can be assumed that the colloidal stability of the oxidized ND is not affected by the fluorination. The zeta potential of fluorinated NDs was  $-46$  mV and showed a strong coulombic stabilization of the fluorinated surface by the remaining unreacted carboxyls. Interestingly, the value measured for oxidized NDs ( $-48$  mV) is very similar,

showing that a relatively low surface coverage with negatively charged groups in a fluorinated sample can still lead to highly charged surfaces (note that only a few percent of remaining unreacted carboxyls was considered).

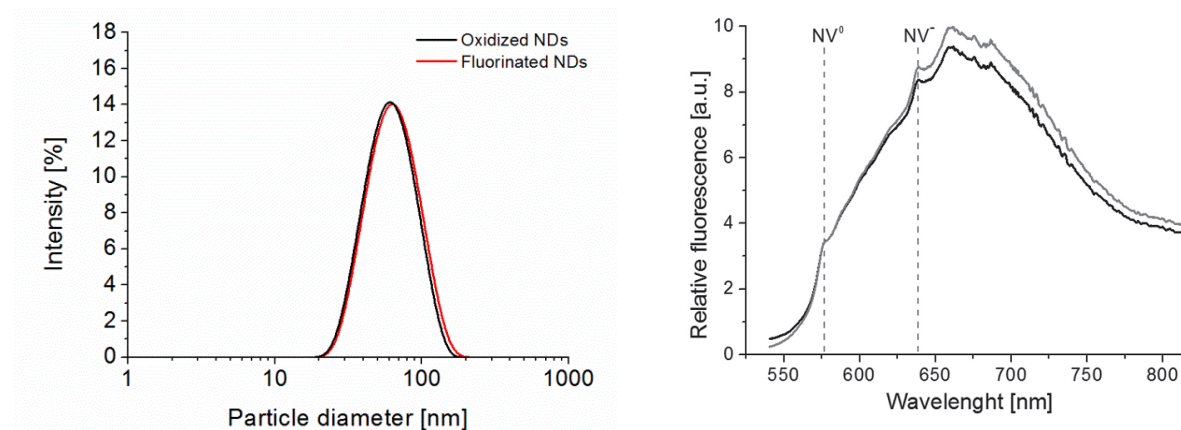


Figure 31: (a) The intensity-weighted size distribution of NDs obtained from DLS. (b) Fluorescence spectra of oxidized (black) and fluorinated (gray) NDs measured in aqueous colloidal solutions and normalized to  $NV^0$  intensity. ZPL of the  $NV^0$  and  $NV^-$  states are shown by dashed lines.

### Structural and morphological analysis using TEM

Chemical modifications of diamonds under harsh conditions, such as oxidative gas treatments at high temperatures (e.g.,  $O_2$ ,  $F_2$ ,  $H_2O$ ), plasma treatment, mineral acid digestion, and treatment in molten  $KNO_3$ , lead to a significant surface etching (144). This results in changes in particle size distributions and in some cases particle shape as well. During such treatments, the surface carbon atomic layers are typically converted into gases (e.g.,  $CO_2$ ,  $CO$ ,  $CF_4$ ) that escape from the surface, consecutively removing the diamond lattice. The decarboxylative fluorination introduced in this work is based on a localized and selective radical mechanism, which is fundamentally different from nonspecific etching. The substitution of carboxyl with fluorine is fixed on the reaction site and stops immediately after the carboxyl has been reacted. It was therefore expected that the particles would not change their original size and shape distribution upon fluorination. For comparison of the particles' size and shape distribution before and after fluorination, the TEM images were analyzed (Figure 29b-c). For each sample, nearly 1300 particles were analyzed, acquired their equivalent circular diameters, and recalculated them to volume-weighted histograms (Figure 29d). To compare the samples' size distributions, the Wilcoxon–Mann–Whitney rank test nonnormal distributions was used, which test the null hypothesis that two sets of data are from the same population against an

alternative hypothesis. The resulting two-tailed probability was  $P = 0.84$ , which does not indicate different distribution of the particle volumes.

The shape of particles in each sample was characterized by particle. The average circularities were  $0.71 \pm 0.15$  and  $0.73 \pm 0.13$  for oxidized and fluorinated NDs, respectively. Comparison of the samples' circularities was performed using two sample t-test with unequal variances; this test showed that the circularities are equal at a significance level of  $\alpha = 0.0001$ . Based on both size distribution and shape analysis, it was concluded that the fluorination procedure has no significant impact on particle morphology. This finding is also an indirect confirmation that the radical fluorination proceeds on the terminal surface layer of carbons and that loss of particle mass observed typically under harsh etching conditions does not take place.

### **Fluorescence properties of NV centres**

Surface engineering of diamond is crucial for achieving high quantum yield of NV centres and for suppressing nonradiative recombination channels. The surface termination has also an influence on the spectral shape of fluorescent NV centres, as shown in studies (4; 47; 123; 145) comparing hydrogenated, oxidized, fluorinated, and nitrogen-terminated surfaces. NV centres exist in two electronic states: Neutral ( $NV^0$ ) and negatively charged ( $NV^-$ ). The  $NV^0$  state emits orange luminescence with zero phonon line (ZPL) around 575 nm; the  $NV^-$  state emits in the red region with ZPL at 637 nm. Both ZPLs are followed by broad phonon replica side band luminescence (Figure 31b). In general, highly electronegative atoms (O, F) covalently attached to the surface shift the Fermi level at the surface and make the  $NV^-$  charge state predominant, while hydrogenation contributes to its depletion. In addition to direct atomic modification, noncovalent surface interactions can also modulate the NV emission (5). Nevertheless, C-F termination is currently considered the most powerful surface termination for stabilization and precise control of the  $NV^-$  charge state (123), which is essential for most measurements and applications of NDs related to detection of chemical, electrical, and magnetic changes occurring within the ND nanoenvironment.

To ascertain the influence of decarboxylative fluorination on the behavior of NV centres in fluorescent NDs, their fluorescence spectra measured in colloidal aqueous solution were compared quantitatively before and after fluorination. A  $\approx 5\%$  increase in emission intensity of the  $NV^-$  state upon fluorination of oxidized NDs was observed (Figure 31b). This change is important, considering that the starting oxygen termination already causes strong inversion of polarity of the surface dipole and the respective band-bending. Despite its low surface coverage the fluorine can contribute distinctly to the downward band-bending. For evaluation of the

effects of fluorination on emission at single particle level, the photoluminescence of ND particles dispersed on quartz cover slip surface after drying up 1  $\mu$ L ND colloidal solution was measured. By analyzing the NV centre distribution in 20 photoluminescence intensity maps (10 for oxidized and 10 for fluorinated particles), local extrema points of the photoluminescence were determined and were analyzed statistically. To exclude influence of singularities of the noise only the points with NV luminescence  $>8$  kilocounts per second (kcps), i.e. 5 kcps above the background (which was  $\approx 3$  kcps for 2.5 mW laser power) were counted. The cover slips prepared from suspension of oxidized diamond showed higher agglomeration for ND crystals, displayed as local maxima with high number of counts. In contrast, the fluorination significantly promoted luminescence in ND particles with weakest fluorescence, presumably the smallest particles in the ensemble. Due to this effect, the total counts for particles or particle clusters containing 1–10 NV centres was 29% higher for fluorinated than for oxidized NDs.

The smaller NDs containing NV centres have been shown as more sensitive to the surface-related effects (101). It is anticipated that the fluorine-induced stabilization of  $NV^-$  state applies preferably to the shallow NV centres present in smaller particles, similarly as observed in oxidized NDs (47). Nevertheless, the fraction of such particles in the whole ensemble is relatively low (Figure 29) and the corresponding increase in  $NV^-$  emission intensity from bulk colloidal solutions upon fluorination is therefore only modest ( $\approx 5\%$ ; see above). Our data show that fluorination further boosts the fluorescence intensity of  $NV^-$  centres and can potentially awake some of the NV centres present in optically inactive states. The possible reasons for NV awakening are the shift of the Fermi level at the surface induced by presence of electronegative fluorine atoms (123) and the compensation of the charge traps that are providing nonradiative recombination channels (47). Our findings correspond fairly well to results from a fluorination study of the oxidized [100] surface, where changes in  $NV^-/(NV^0 + NV^-)$  were also small ( $<0.04$ ) (146). A very different situation occurs during comparison of hydrogenated and fluorinated surfaces (146). In these cases, the detrimental upward band-bending caused by C-H termination is completely inverted and the change in  $NV^-/(NV^0 + NV^-)$  ratio is extensive, causing robust changes in spectral shape.

#### 4.3.5. Conclusion

A synthetic pathway leading to selective  $Ag^+$ -catalyzed substitution of ND surface carboxyls with fluorine using selective  $sp^3$ -based radical chemistry has been developed. It was focused on NDs because fluorination of this carbon nanomaterial leads to surface band-bending that stabilizes shallow fluorescent NV centres. In addition, it was aimed to prepare a mixed

oxygen-fluorine termination preserving the hydrophilic behavior of oxygen-containing groups and introducing the electronic properties of fluorine. In contrast to the harsh fluorination procedures used for diamonds (for example, treatments using molecular fluorine in a fluorine line, fluorine-containing plasmas, and X-ray irradiation), our one-step approach proceeds at mild conditions in an aqueous dispersion of NDs and can be easily performed on the benchtop without special safety precautions. The procedure is robust enough to proceed with high yields on extremely sterically demanding substrates such as NDs and results in the mixed C-F and C-OH termination. Thanks to the overall hydrophilic surface, the particles form a stable colloid in an aqueous environment, as has been demonstrated by DLS. Moreover, using precise TEM image analysis, it was found that the particles retain their size and shape, which supports our assumptions regarding the unique, nonetching nature of the decarboxylative fluorination. The resulting surface was characterized using XPS and elemental analysis and spectrally analyzed the effect of fluorination on stabilization of negatively charged fluorescent NV centres in NDs. Consistent with recent fluorination approaches achieved under harsh conditions (146; 123), it was found that decarboxylative fluorination also positively influences the NV centres, boosting their overall fluorescent intensity. In our opinion, this finding significantly extends the current approaches to diamond surface engineering (20), which has major implications for important quantum physical and bioimaging applications that require bright and stable NV centres.

Finally, it can be expected that decarboxylative fluorination of a diamond surface bearing a higher number of carboxyls may lead to correspondingly higher surface coverage with fluorine. This can be used for controlled high-yield fluorination of diamonds, which is essential for applications such as a recently described quantum simulator (147) and represents one possible pathway to stabilized ultrabright single-digit-sized ND probes relevant for bioimaging and quantum sensing. Substantially exceeding the current highest surface coverage of carboxyls ( $\approx 7\%$ ) (141) using *de novo* chemical approaches is therefore an important goal for further development of  $sp^3$  chemistry on diamonds, not only from a fluorination perspective.

### **Acknowledgement**

The authors acknowledge the support of the Grant Agency of the Czech Republic Project No. 16-16336S and the Ministry of Health of the Czech Republic, Grant No. 15-33094A. Irradiations of NDs were carried out at the CANAM infrastructure of the NPI ASCR Rez supported through MŠMT Project No. LM2011019. Financial support from specific university research (MSMT No. 20/2015) and EU-FP7 Research Grant DIADEMS, Grant Agreement No. 611143 is acknowledged.

#### 4.4. Label free visualization of near-IR probes in cells using Raman imaging

I have presented this work at the **Fifth Annual International SLAS Conference & Exhibition**, January 2016, in the San Diego in a form of a poster. Co-authors are: H. Salehi, B. Varga, T. Cloitre, F. J. G. Cuisinier, P. Cígler, M. Nesládek and C. Gergely. This work deals with a detection of fluorescent NDs in cell environment using Raman imaging technique. As a main author of this work I have carried out all experiments (except TEM measurements) of which the results are presented here (including K-mean cluster analysis). I have grown and incubated the cells for the experiments at Laboratoire de Bioingénierie et Nanosciences, Montpellier. Raman images were taken during my stay there with help and assistance of H. Salehi. Outcomes of this work are in preparation for the scientific article in Journal of Biophotonics (**IF = 3.82**). Following chapter contains to-date results.

##### 4.4.1. Abstract

I demonstrate a Raman imaging method as a novel way to detect small (~ 10 nm) nanodiamond particles (ND) with high sensitivity within the living cells. The Raman signal is processed using K-mean cluster analysis of the obtained spectra from the image pixels. By mapping the intensity of specific part of the cell C-H Raman peak, I was able to visualize the cell nucleus clearly. This original method provides an easy way to detect any near-IR probes with respect to the cell nucleus without any additional dyes.

##### 4.4.2. Introduction

Fluorescent nano-diamonds are becoming increasingly attractive tools for nanoscale biological cellular imaging allowing both photoluminescence and magnetic resonance imaging (148). Recent technological developments enable to fabricate bright fluorescent nanodiamond (ND) particles of various sizes with high content of nitrogen-vacancy (NV) centres (7). NV centres exhibit a bright luminescence in red and near infrared spectrum with different zero-phonon lines depending on the NV centre charge state (575 nm for NV<sup>0</sup> and 636 nm for NV<sup>-</sup>) and a broad red-shifted phonon sideband (PSB) of 640-800 nm. ND particles can be grafted with various surface ligands for specific recognition by the cell receptors, allowing targeted delivery of NDs. NDs enter the cell via clathrin-mediated endocytosis (149) and their cellular fate depends on the morphology of the nanoparticles (150). Sharp-shaped NDs penetrate the membranes of endosome and escape to the cytoplasm. Thanks to the stable non-bleaching fluorescence, NDs can be visualized in cell by the means of luminescence microscopy.

However, to localize their position with respect to cell organelles (e.g. cell nucleus), often labeling with an additional fluorescence dyes or fixation of the cells is necessary, which can alter the outcomes of studied processes.

Here I present novel method to visualize the ND in cells using Raman imaging and thus having an additional information from cell Raman signal. This method enables detection of even small ND particles (~ 10 nm) with high sensitivity and distinguishing directly the NDs inside or outside the cells. Also, having Raman spectrum from each pixel, I was able to develop a method of visualizing the cell nucleus of non-fixed cells by imaging the change of intensity of only specific part of C-H Raman to create contrast between lipid and protein contribution to the signal. I demonstrate this method on breast cancer (MCF7) cell line and dental pulp stem cells (DPSC) using luminescent NDs (detecting mainly the PSB of NVs), but it can be apply to any near-IR probe. Some of the works have already shown ND detection in cells using Raman (151; 152; 153; 154; 155). However, this was demonstrated only on 100 nm size NDs or larger (presumably due to the low Raman signal), limiting thus its application. In (151; 152; 153; 154) blue laser (488 nm) is used and NDs are imaged using diamond Raman signal at  $1332\text{ cm}^{-1}$  whereas in (155) coherent anti-Stokes Raman scattering (CARS) at the  $sp^3$  vibrational resonance of diamond is employed to detect 150 - 300 nm large NDs. Our method allows to detect any near-IR luminescence probes and thanks to the green laser (532 nm) excitation, detection of the characteristic NV spectra and readout out the Raman information from cells C-H bond peak at the same time is possible.

#### 4.4.3. Methods and materials

Luminescent ND particles of size range from 5 to 50 nm were used, prepared from Ib synthetic diamond. Particles were electron irradiated, annealed and plasma oxidized to create stabilized NV centres. Cells used for the experiments were breast cancer (MCF7) and dental pulp stem cells (DPSC). Cells were grown on  $\text{CaF}_2$  substrate in Dulbecco's modified eagle's medium (DMEM) at  $37\text{ }^\circ\text{C}$  and  $5\% \text{ CO}_2$  for couple days to obtain the desired confluency. NDs diluted in distilled deionized water (4 mg/ml) were filtered through 200 nm filter to exclude bacteria or larger clusters of nanoparticles. Resultant concentration of NDs after the filtration was confirmed by gravimetric analysis and the solution was further diluted in distilled deionized water to obtain ND concentration of 1 mg/ml. Bovine serum albumin (BSA) was gradually added to the NDs solution to prevent aggregation of NDs in cell medium. Lastly, this mixture was diluted in DMEM to obtain a concentration of  $30\text{ }\mu\text{g/ml}$  NDs in DMEM with BSA concentration of 10 %. NDs in DMEM were heated up to  $37\text{ }^\circ\text{C}$  prior to incubation and the

original cell medium was completely removed and replaced by ND-containing medium. Incubated cells were kept at 37 °C and 5% CO<sub>2</sub> for 1 hour. Afterwards, samples were rinsed 5 times in Dulbecco's Phosphate-Buffered Saline (DPBS) and were kept in DPBS for the Raman measurements.

The Raman spectra were collected using a Witec Confocal Raman Microscope System alpha 300R (Witec Inc., Ulm, Germany). The excitation for the confocal Raman microscope was provided by a frequency doubled Nd:YAG laser (Newport, Evry, France) at the wavelength of 532 nm, with 50 mW laser output power. The signal was detected by the electron multiplying charge-coupled device (CCD) camera (DU 970 N-BV353, Andor, Hartford, USA). The spatial resolution of the system is calculated by the formula  $d = 1.22 \cdot \lambda_{\text{laser}} / 2 \cdot \text{NA}$ , which for our system is 325 nm. The data acquisition and processing were performed using the Image Plus software from Witec.

The data analysis was based on two steps. First, I utilized integrated Raman vibration mode intensities of the C-H stretching mode, which is one of the vibrational modes of the C-H groups and one of the most intense Raman mode found in cells. C-Hs are abundant in protein, lipid, and carbohydrate, and the image based on the intensity of this band provides a pseudo map of protein, lipid, and carbohydrate concentration in cells (156). Cell image was then created by mapping the intensities of the C-H peak. Also, here for the first time, I demonstrate visualization of the cell nucleus by mapping only a specific part of the C-H peak. The second part is a K-mean cluster analysis of the obtained spectra, which is an unsupervised algorithm that solves the clustering problems (157). The procedure follows a way to classify a given data set through a certain number of clusters (assume k clusters). Five clusters in total were created: 1 cluster without NV luminescence and 4 NV clusters divide by the presence on C-H peak to “inside” and “outside” NDs and by the intensity of the detected luminescence to “high” and “low”. Great care was taken when selecting the threshold for NV luminescence to prevent false positive detection of NDs.

#### 4.4.4. Results and discussions

I report on accomplishing to successfully internalize oxidized ND particles in both cell lines. It is shown that this ND internalization can be followed by Raman imaging method using K-mean cluster analysis to detect the NV luminescence. Commonly used spectral detection window for cell imaging using 532 nm Raman is roughly from 100 to 3600 cm<sup>-1</sup> (158), which

corresponds to  $\sim 535$  and  $\sim 658$  nm respectively (see Figure 32a). The region from 700 to 1700  $\text{cm}^{-1}$  contains specific cell peaks that can be analyzed to determine whether the signal comes from cell nucleus, cytoplasm or mitochondria (159). The band from 2800 to 3000  $\text{cm}^{-1}$  corresponds to the C-H stretching mode and the peak at 3400  $\text{cm}^{-1}$  corresponds to Raman signal of water present in DPBS. First, the ND internalization was imaged keeping common detection window with the central wavelength of Raman grating at 600 nm (see Figure 32b). This yields however low recognition of the NDs, as a main part of NV luminescence is undetected (due to the spectral range up to 658 nm, whereas NV emits with maximum around 700 nm) and rest of the NV luminescence interferes with the C-H band and with the water Raman peak. Therefore, the central wavelength of the grating was moved to 680 nm and the measurement was repeated on the same cells. The resulting spectra can be seen in Figure 32c. This way, I still detected the C-H band and also the majority of the NV luminescence. However, the characteristic cell peaks from 700 to 1700  $\text{cm}^{-1}$  region were lost as a consequence. The detected spectra that contained NV luminescence were sorted into four cluster depending on whether the signal comes from the cells (by the presence of the C-H peak) and whether the luminescence signal was high or low (see Figure 32c). NDs outside the cells with low intensity were marked light blue (both spectrum and image) and dark blue for those with high intensity (both spectrum and image). NDs inside the cells with low intensity were marked yellow (both spectrum and image) and those with high intensity black (spectrum) or white (image). Detecting over larger spectral range of NV luminescence improves the sensitivity dramatically, as can be seen in the retake image at Figure 32d, where several times more NDs are detected. Still, the threshold level for determining whether there is a NV signal in the spectrum of particular pixel was set too strictly neglecting weak luminescence signals. The measurement on control cell sample without ND incubation (Figure 32d) proves that no signal is detected at around 700 nm. Thus enabling us to lower the threshold for detection and reach the ultimate sensitivity demonstrated in Figure 32e. The detection capability of Raman method to image NDs is here demonstrated on MCF7 cell line, however comparable results were obtained for DPSC.

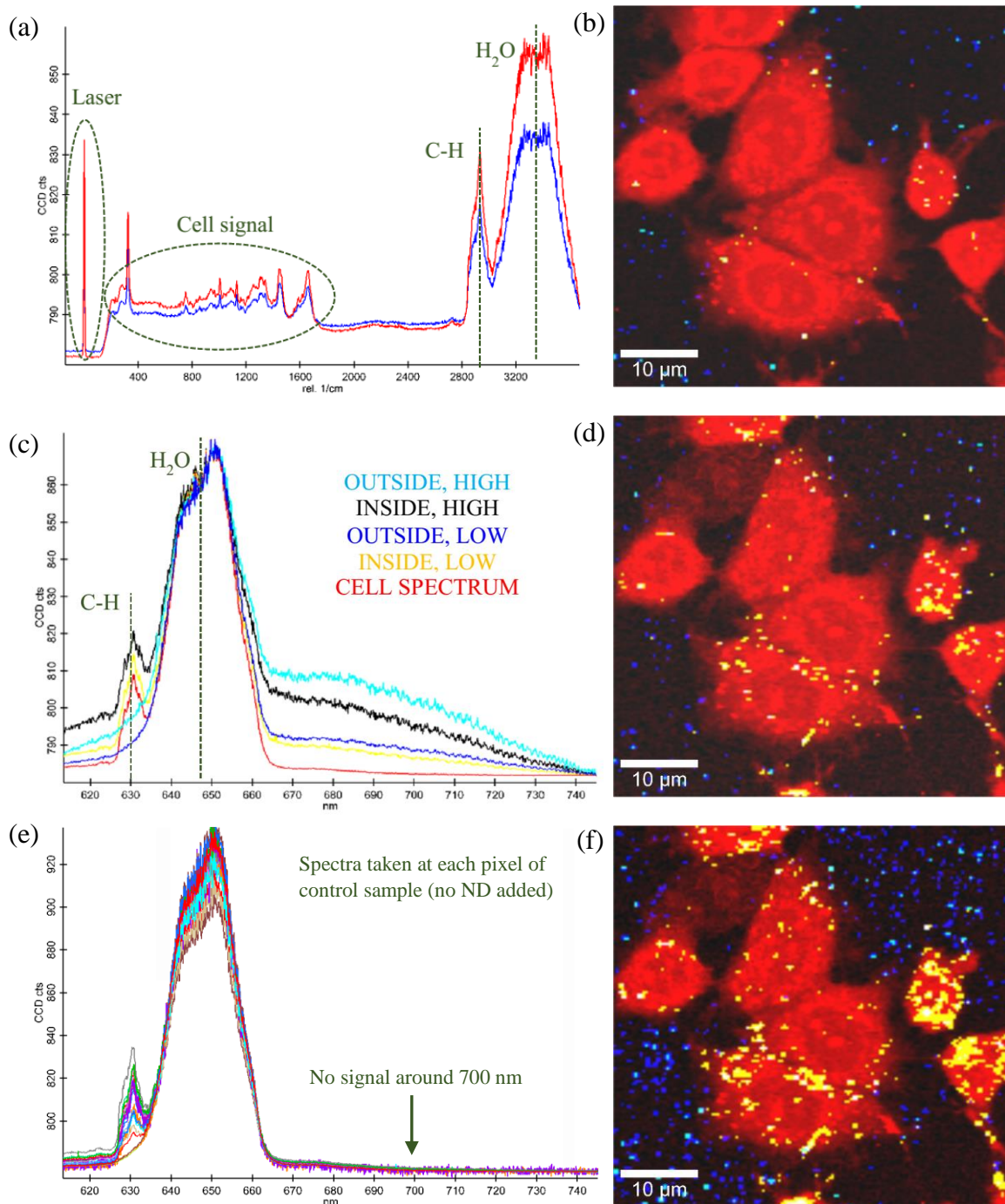
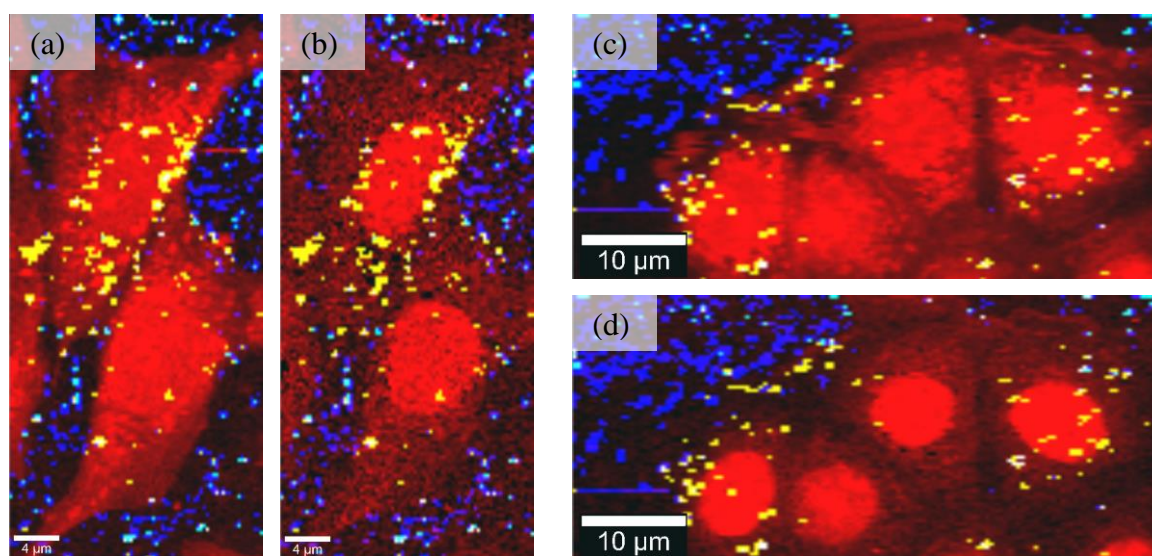


Figure 32: Raman imaging method demonstrated on MCF7 cell line. (a) The exemplary spectra obtained with the central wavelength of Raman grating at 600 nm (common setting for Raman cell imaging) and (b) the corresponding Raman image created by merging the distribution map of Raman signal locked on C-H peak (in red) with image of detected NDs (in light blue, dark blue, yellow and white – see methods). (c) The exemplary spectra obtained with the central wavelength of Raman grating at 680 nm for enhanced detection showing the average spectrum of five created clusters (see methods) and (d) the corresponding Raman image (colors of clusters are same for spectra and the image only black spectrum corresponds to the white color in the image for clarity). (e) Spectra from all the pixels obtained by Raman imaging of the control cell sample with no ND incubation. Lack of any signal at around 700 nm enables to lower the threshold for detection of NV luminescence and providing thus better sensitivity as demonstrated at the reanalyzed image (f) of the measurement (d).

These results prove applicability of cell Raman imaging together with high sensitivity for detection of the luminescent NDs. It, however, requires to shift the position of Raman grating to longer central wavelength and thus losing the characteristic peaks from cell sites. To utilize the remaining Raman cell signal, I exploit the possibilities of C-H band visualization. The Raman signal of C-H stretching mode comes mainly from proteins, lipids, and carbohydrates within the cells (124). However the exact shape and position of this peak differs for different concentrations of these molecules in the detected confocal volume. I have found out that by visualizing only part of the C-H band, a contrast between the cell nucleus and the rest of the cell can be created. I believe that this contrast arises from the lack of lipids and high content of proteins in the nucleus. Specifically, the intensities of C-H band in the range  $2929\text{ cm}^{-1}$  to  $3012.5\text{ cm}^{-1}$  (corresponding to  $\sim 630.2\text{ nm}$  and  $\sim 633.5\text{ nm}$ ) are mapped in comparison to standard mapping where the whole peak from  $2800\text{ cm}^{-1}$  to  $3000\text{ cm}^{-1}$  is employed. The demonstration of such nucleus visualization in MCF7 is shown in Figure 33 with comparison to standard image.



*Figure 33: Demonstration of Raman visualization of MCF7 cell nucleus by mapping the specific range of C-H peak. The images (a) and (b) are depicted using standard full-range C-H intensity mapping. The corresponding (c) and (d) images (respectively) demonstrate the possibility for nucleus label-free visualization obtained by mapping only the specific part of the C-H peak.*

To prove that the NDs are indeed successfully internalized in the cells and to localize them precisely, the MCF7 incubated cells were studied using Transmission Electron Microscopy (TEM). The incubation procedure, time and ND concentration was kept the same as for Raman imaging. The Figure 34 captures the ND internalization process in the beginning stage of endocytosis demonstrating successful uptake of NDs by the cell.

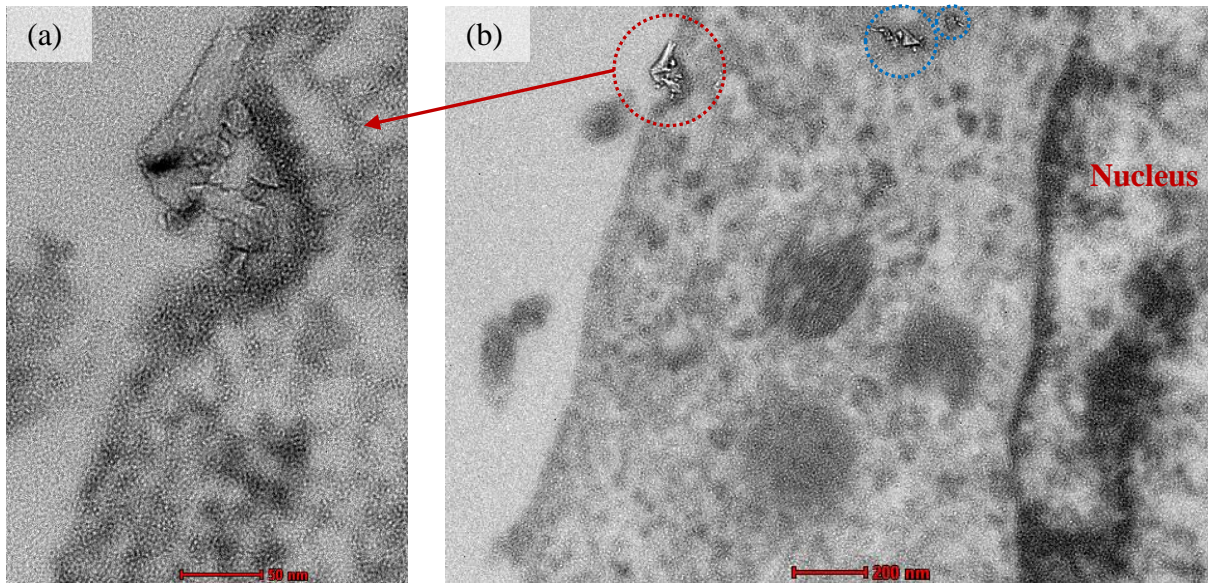


Figure 34: TEM images showing endocytosis of NDs in MCF7 cell (red circle) and particles freely in the cytoplasm (blue circles). Image (a) is a zoom of selected part of image (b).

Most of the ND were localized in the endosomes (see Figure 35), however, many particles were positioned freely in the cell cytoplasm including single NV particles (see Figure 34b). No NDs were found in the cell nucleus.

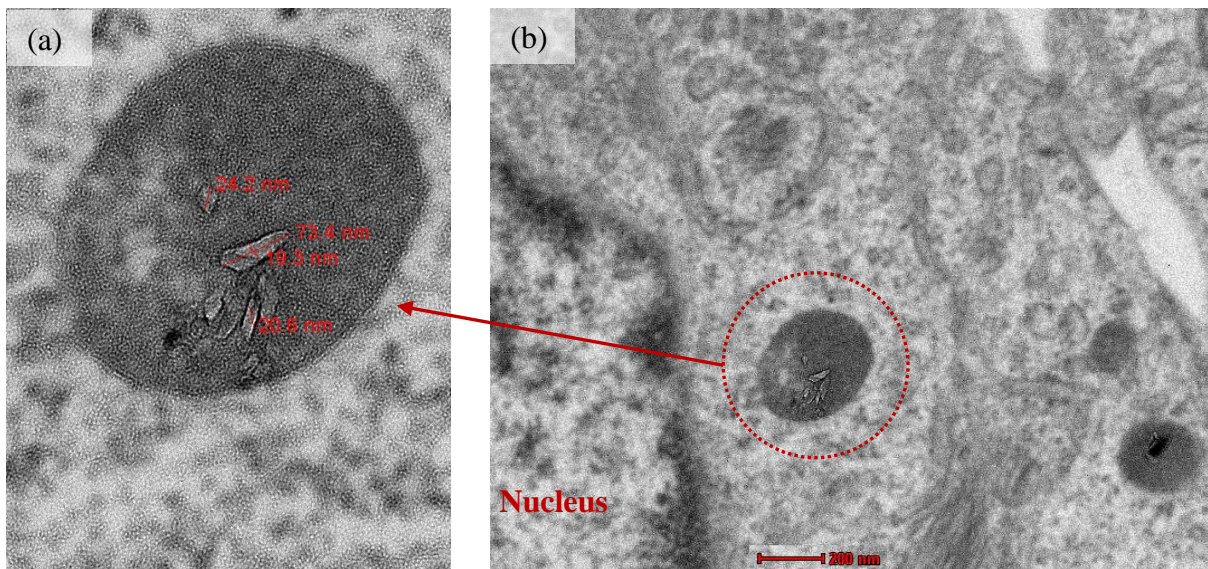


Figure 35: TEM images showing ND particles in endosomes of MCF7 cell. Image (a) is a zoom of selected part of image (b).

#### 4.4.5. Conclusion

I have demonstrated a novel way how to visualize the nucleus of living cells (most of the nucleus labels require fixation) utilizing Raman imaging without using any label that

interferes with the cells. At the same time I detected ND with high sensitivity even for small particles. The successful internalization of plain oxidized NDs (stabilized only with serum) into the MCF7 cells was confirmed by TEM. This method is a simple alternative to visualize any near-IR probes with respect to the cell nucleus. Moreover, by employing wider Raman grating or by scanning the spectral signal from each pixel, one can acquire broader spectrum including the characteristic cell peaks and localize thus the near-IR probes with respect to other organelles (i.e. mitochondria).

### **Acknowledgement**

The work was supported by OP VK grant CZ.1.07/2.3.00/20.0306 and SGS14/214/OHK4/3T/17

#### 4.5. AFM study of diamond particles internalization by monitoring the cell membrane stiffness changes

The first results of this work have been presented on-stage at **AFM BioMed Conference**, Porto, 2016. Co-authors are: M. Martin, B. Varga, H. Salehi, T. Cloitre, P. Cígler, M. Nesládek and C. Gergely. The data presented here study the cell membrane stiffness changes upon NDs' internalization as a way to observe ND uptake rate in time. As a main author of these results I have carried out all the measurements that are presented here. I have grown and incubated the cells for all experiments. The AFM measurements were executed at Laboratoire Charles Coulomb, Montpellier during my stay there with help and assistance of M. Martin. Raman images were taken at Laboratoire de Bioingénierie et Nanosciences, Montpellier during my stay there with help and assistance of H. Salehi. This work is still in progress as additional experiments are being carried out to provide more complex study and conclusive results. Outcomes of this work are in preparation for publication.

##### 4.5.1. Abstract

Atomic Force Microscopy (AFM) imaging and force spectroscopy is applied to study how the NDs internalization processes into the breast cancer MCF7 cell line influence the cell membrane elasticity. Changes of cells stiffness were detected by AFM force measurements after introducing the NDs into the cell medium. Variations of cell membrane Young's modulus were observed as the cells became stiffer in time. It is believed that uptake (release) processes of NDs are responsible for these mechanical changes. The trend of cell membrane hardening can be utilized to determine the nanoparticles internalization rate in time. Moreover, the results suggest that studies of NDs uptake should consider the cell cycle, as in a cell population the dose of internalized nanoparticles varies for each cell.

##### 4.5.2. Introduction

Common methods to study NDs' behavior within the cells employ the light source as an excitation mean for luminescence microscopy (6), Raman detection of diamond  $sp^3$  (155; 153) signal or in differential interference contrast microscopy (160). Here I present an alternative method to study particles internalization using Atomic Force Microscopy (AFM), which provides detailed in-time analysis of uptake rate of individual cells and can be moreover combined with the standard optical methods.

### 4.5.3. Methods and materials

Luminescent ND particles of size range from 5 to 50 nm were prepared as in the previous work (see chapter 4.4.3). For the experiments I used breast cancer (MCF7) cells grown on a collagen coated Petri dish lid. The collagen coating provides better cell adhesion and was prepared in following way. First, the collagen solution (150 $\mu$ g/ml) was created by dissolving cold (4°) 1 mg/ml collagen stock solution in the sterile phosphate buffer solution (PBS, pH = 5.8, ionic strength 160 mM) and consequent filtering with a 0.45  $\mu$ m filter. This solution was further diluted in PBS to obtain final concentration of 7  $\mu$ g/ml. Petri dishes were then filled with 2 ml of the 7  $\mu$ g/ml collagen solution and placed into the incubator (37 °C and 5% CO<sub>2</sub>) for 2 hours. Residual solution was removed by pipette and the Petri dishes were left in the incubator for at least 3 days to dry out completely. Cells were grown in Dulbecco's modified eagle's medium (DMEM) at 37 °C and 5% CO<sub>2</sub> for couple days to obtain the desired confluency.

NDs diluted in distilled deionized water (4 mg/ml) were filtered through 200 nm filter to exclude bacteria or larger clusters of nanoparticles. Resultant concentration of NDs after the filtration was confirmed by gravimetric analysis and the solution was further diluted in distilled deionized water to obtain ND concentration of 1 mg/ml. Bovine serum albumin (BSA) was gradually added to the NDs' solution to prevent aggregation of NDs in cell medium. Lastly, this mixture was diluted in DMEM to obtain concentrations of 10 and 30  $\mu$ g/ml NDs in DMEM with BSA concentration of 10 %. NDs in DMEM were heated up to 37 °C prior to incubation and the original cell medium was completely removed and replaced by ND containing medium. Cells were measured prior to incubation and immediately after it.

The AFM experimental system used for both cell imaging and force mapping was the Asylum MFP-3D head coupled to the Molecular Force Probe 3D controller (Asylum Research, Santa Barbara, CA, USA), and mounted on an Olympus inverted microscope. Triangular silicon nitride cantilevers (MLCTAUHW, Veeco) with a nominal spring constant of 10 pN/nm and half-opening angle of 35°, and Bio-levers (BL-RC150VB, Olympus) with a nominal spring constant of 30 pN/nm and half-opening angle of 45° were used. Prior to each measurement, the spring constant of cantilevers was determined using the thermal noise method within the supplied software. A time-consequent force maps of the cells were performed to analyze the changes of Young's modulus in time. The data were processed individually for each cell (for more details see (161)).

#### 4.5.4. Results and discussions

Changes of cells stiffness were detected by AFM force measurement after introducing the NDs into the cell medium. The measured time-consequent force maps of MCF7 incubated with 10 and 30  $\mu\text{g/ml}$  NDs in DMEM are shown in Figure 36. Individual cells were identified on height and deflection AFM image, though the cell position is also apparent from the force map itself (as collagen is much stiffer than cell). Each cell was then analyzed individually for each force map. The average value of individual cell membrane Young's modulus is plotted with respect of the measurement time showing a clear trend of cell membrane stiffening after NDs incubation. This cell hardening effect is expectably greater for the experiments with higher ND concentration.

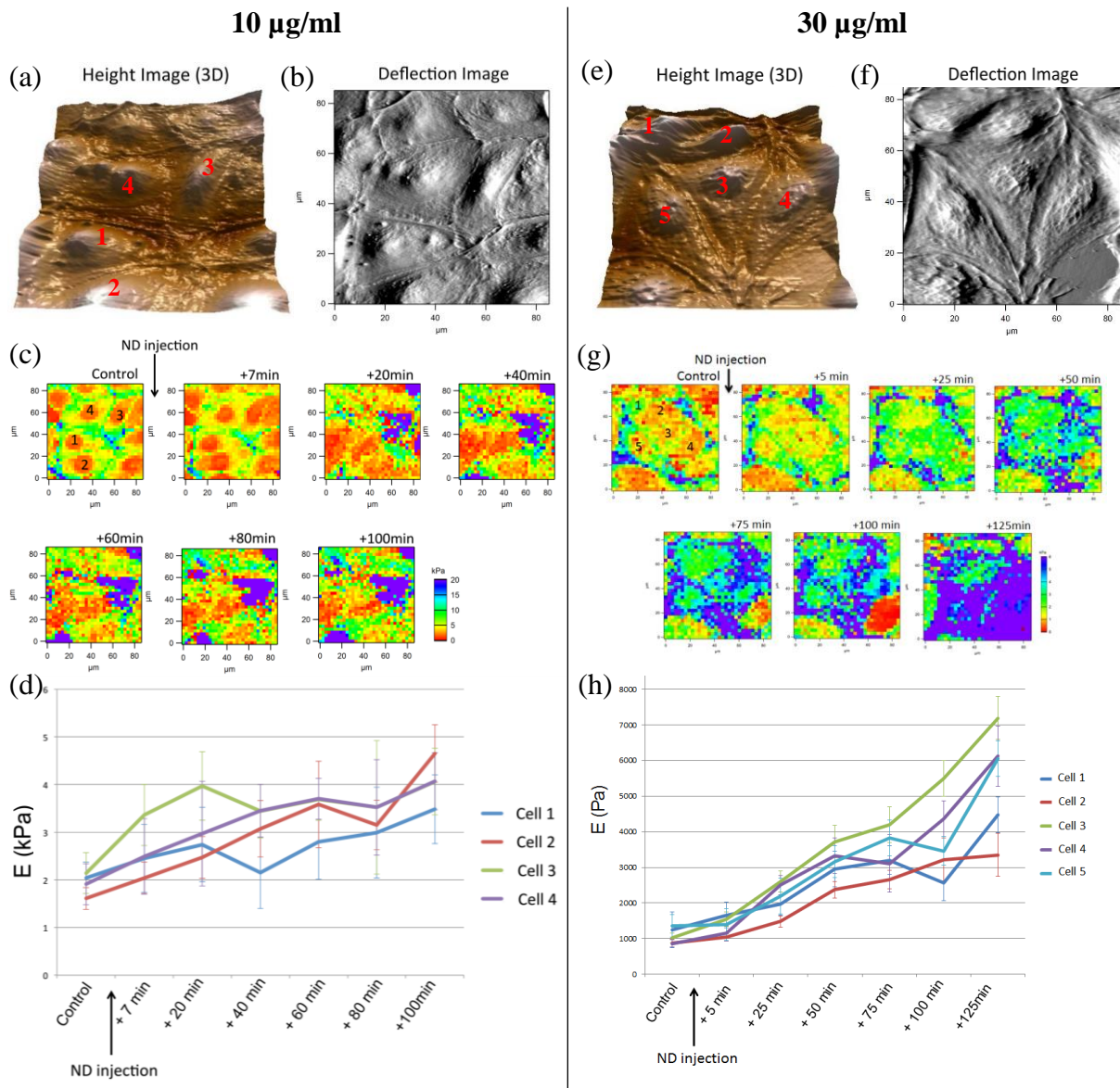


Figure 36: Study of cell membrane mechanical changes upon ND incubation. (a) AFM height image of MCF7 cells before incubation with 10 µg/ml of NDs and (b) corresponding height image. (c) Time-consequent force maps of the cells before and after incubation with 10 µg/ml of NDs. (d) Resulting graph of average cell membrane Young's modulus for each individual cell for 10 µg/ml ND incubation. (e) AFM height image of MCF7 cells before incubation with 30 µg/ml of NDs and (f) corresponding height image. (g) Time-consequent force maps of the cells before and after incubation with 30 µg/ml of NDs. (h) Resulting graph of average cell membrane Young's modulus for each individual cell for 30 µg/ml ND incubation.

I assume that NDs' uptake processes of NDs are responsible for these mechanical changes. To explore this idea further, I repeated the experiments using cells grown for longer time (few days) as it has been shown that cell confluency and age can play role in endocytosis rate (162) and suppress the uptake. As confirmed by AFM morphology image (see Figure 37a), the cell confluency used for the measurements was high. The cells are closely packed and growing tall on their borders. I thus repeated the force spectroscopy experiment with 10 µg/ml

ND incubation (Figure 37). Compared to the experiments in Figure 36, more confluent MCF7 cells did not show any significant change in Young's Modulus (Figure 37d) as expected.

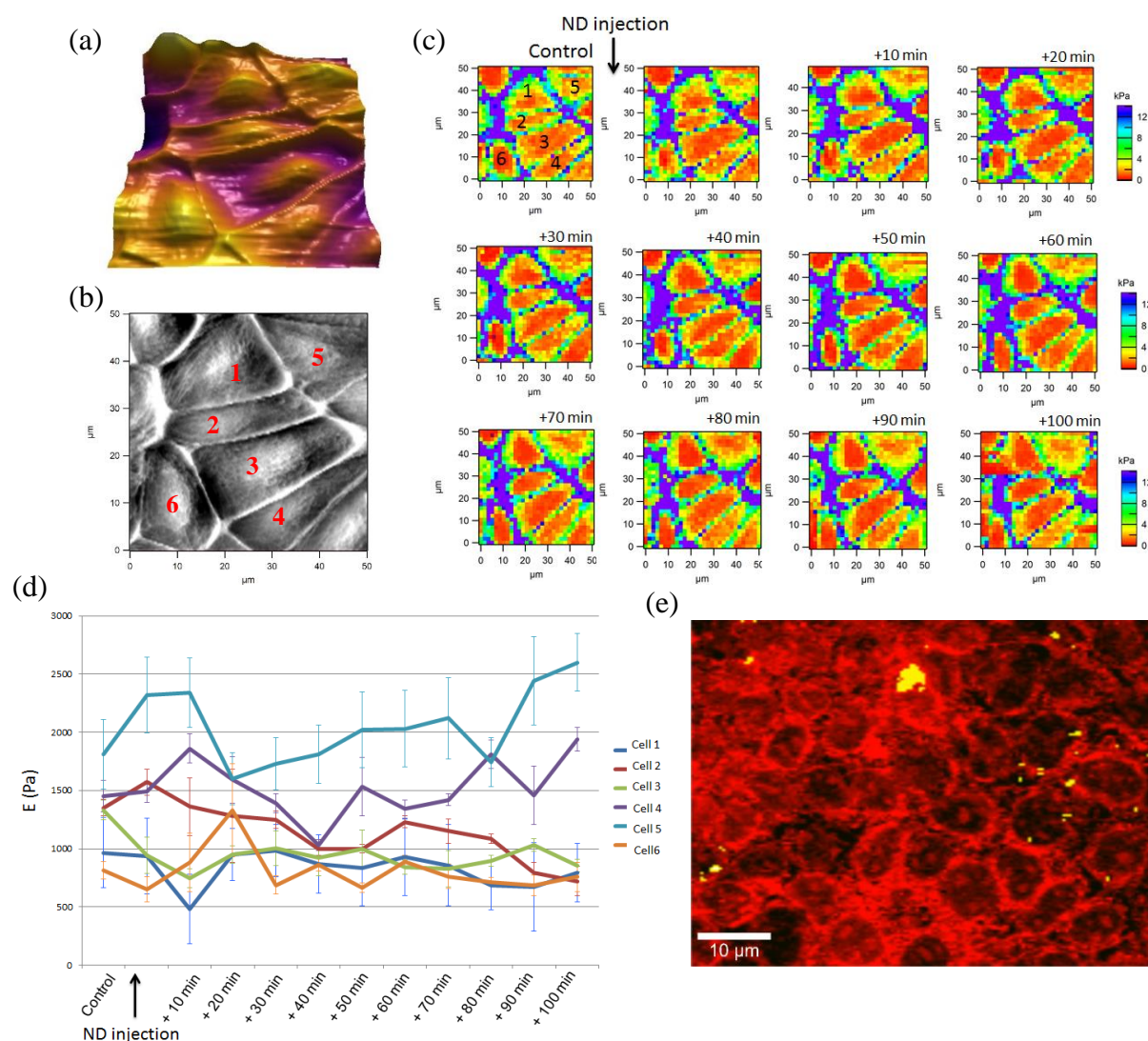


Figure 37: Study of confluent cell membrane mechanical changes upon 10  $\mu\text{g/ml}$  ND incubation. (a) AFM height image of MCF7 cells before incubation and (b) corresponding height image. (c) Time-consequent force maps of the cells before and after incubation with NDs. (d) Resulting graph of average cell membrane Young's modulus for each individual cell for 10  $\mu\text{g/ml}$  ND incubation. (e) Raman image of cell C-H peak intensity merged with luminescence image of NDs confirming the uptake suppression of confluent cells (incubated with 30  $\mu\text{g/ml}$  ND for 1 hour).

To confirm that closely packed cells do not internalize particles, I took another confluent cell sample (prepared simultaneously) and measured the Raman image (using method developed previously, see chapter 4.4) after incubation with 30  $\mu\text{g/ml}$  of NDs for 1 hour. The result (Figure 37e) confirmed the suppression of uptake for confluent cells, supporting the

presumption that the ND internalization processes are responsible for cell membrane mechanical changes rather than merely the presence of NDs in the medium.

#### 4.5.5. Conclusion and future work

I have studied cell membrane elasticity changes upon internalization with nanodiamonds in time. By analyzing the time-consequent force maps I was able to determine mechanical changes of cell membrane stiffness for individual cells. Results suggest that cells are hardening upon NDs' uptake. Moreover, one should consider the cell cycle, as in a cell population, the dose of internalized nanoparticles in each cell varies as the expression of membrane proteins vary during the cell cycle (163; 164). The cell cycle is a series of events that lead to cell division and replication, consisting of four phases: G1 (when the cell increases its size), S (the cell synthesizes DNA), G2 (the cell synthesizes proteins for cell division) and M (the cell divides and the two daughter cells enter the G1 phase). During each event, cellular processes can vary; meaning that the rate at which a cell takes up foreign material, as for instance nanoparticles, may depend on the phase the cell is in (165; 166), modifying accordingly their elasticity. Therefore, the further plan is to resolve how the state of the different cells affects the uptake of NDs by measuring the cell stiffness changes.

#### **Acknowledgement**

The work was supported by OP VK grant CZ.1.07/2.3.00/20.0306 and SGS14/214/OHK4/3T/17

## 4.6. Photoelectric detection of electron spin resonance of nitrogen-vacancy centres in diamond

This result has been published in **Nature Communications** journal (**IF = 11.470**) and parts of the article are reprinted here with changes. Authors of the work are: E. Bourgeois, A. Jarmola, P. Siyushev, M. Gulka, J. Hruby, F. Jelezko, D. Budker and M. Nesladek. In this chapter, novel method for reading out the spin state of negatively charged NV centre was developed. Common methods employ optical readout (photon detection), here we detect photocurrent originated from ionization of the NV centres. The proposed scheme overcomes many drawbacks limiting the optical readout. As a co-author I was building and testing the ODMR setup, acquiring first ODMR signal, designing and developing hardware PDMR method, enhancing photocurrent setup by ODMR means to enable PDMR detection, testing the PDMR software, developing PDMR measurement scheme and acquiring first measurements of PDMR signal. All other work was done by remaining authors of the paper. Final PDMR measurements that are presented in the paper were done at Institute for Materials Research, Hasselt University, Belgium and at Institute for Quantum Optics and IQST, Ulm University, Germany.

### 4.6.1. Abstract

The readout of negatively charged nitrogen-vacancy ( $NV^-$ ) centres electron spins is essential for applications in quantum computation, metrology and sensing. Conventional readout protocols are based on the detection of photons emitted from  $NV^-$  centres, a process limited by the efficiency of photon collection. We report on a novel principle for detecting the magnetic resonance of  $NV^-$  centres, allowing the direct photoelectric read-out of  $NV^-$  centres spin state in an all-diamond device. The photocurrent detection of magnetic resonance (PDMR) scheme is based on the detection of charge carriers promoted to the conduction band of diamond by two-photon ionization of  $NV^-$  centres. Optical detection of magnetic resonance (ODMR) and PDMR are compared, by performing both types of measurements simultaneously. The minima detected in the measured photocurrent at resonant microwave frequencies are attributed to the spin-dependent ionization dynamics of  $NV^-$ , originating from spin-selective non-radiative transitions to the metastable singlet state.

#### 4.6.2. Introduction

Reading out the electron spin of the negatively charged nitrogen-vacancy ( $\text{NV}^-$ ) centres in diamond is essential for applications in quantum computing and secure communication (81), as well as for nanoscale magnetic and electric sensing (96) or for non-perturbing sensing and imaging of quantum objects (104).  $\text{NV}^-$  ensembles in bulk diamond are in addition used for high-sensitivity magnetometry, with sub-micrometer resolution (70). At present, the read-out of  $\text{NV}^-$  centres electron spin state is typically performed optically, by detecting photons using confocal microscopy. No all-diamond read-out technique allowing for integration with diamond electronic chips is available. One of the limiting factors for optical detection is the low collection efficiency of photons emitted by  $\text{NV}^-$  centres in bulk diamond, due to the limitations of objective optics and to the diamonds high index of refraction. Reaching an optical detection efficiency higher than a few percents most often requires complex micro-fabrication (167), even though simpler techniques for the fabrication of diamond photonics structures were recently proposed (168). Additionally,  $\text{NV}^-$  centre based quantum computing involves positioning adjacent  $\text{NV}^-$  centres at a distance of approximately 10 nm (169). The individual optical read-out of such proximal  $\text{NV}^-$  centres is difficult, since it requires a resolution below the diffraction limit.

In this report a novel non-optical technique consisting in direct photoelectric read-out of the electron-spin resonance of  $\text{NV}^-$  centres is described. This scheme is denoted as photocurrent detection of magnetic resonance (PDMR). Similarly to the read-out method presented in (170), our detection technique is based on the spin-dependence of  $\text{NV}^-$  ionization dynamics. However, while in (170) spin detection relies on an optical read-out of  $\text{NV}^-$  charge state, our technique is based on direct electric detection of charge carriers excited from  $\text{NV}^-$  centres to the diamond conduction band, which can be performed electrically on a chip. Contrary to a recently proposed scheme, in which electronic read-out of  $\text{NV}^-$  centres spin state is performed by monitoring non-radiative energy transfers to graphene (171), PDMR detection can be performed in an all-diamond device, without the indirect energy transfer to another material. Photoelectric detection of spin resonances only requires the fabrication of electrodes on the diamond chip by standard lithography. It avoids the complexity of confocal imaging and would allow for example the detection of  $\text{NV}^-$  spin resonance in light-scattering media.

The PDMR technique is demonstrated on  $\text{NV}^-$  ensembles, however it may be developed to be used for the read-out spins of single  $\text{NV}^-$  centre. By further downscaling the inter-electrode

distance to 10 nm gaps (172), PDMR has the potential to reach the independent read-out of NV<sup>-</sup> centres situated closer than the diffraction limit. Another peculiar feature of the photocurrent detection principle is the photoelectric gain mechanism (173), which might lead to high detection efficiency since every photon has the ability to generate more than one electron-hole pair.

#### 4.6.3. Methods and materials

The samples characterized by ODMR and PDMR were prepared by electron-irradiating a high-pressure high-temperature type-Ib single-crystal diamond (2.9×2.9×0.5 mm<sup>3</sup> plate from Element Six) with an initial concentration of approximately 200 ppm of N<sub>s</sub><sup>0</sup> (sample E2) and a chemical vapour deposited optical grade type-IIa single-crystal diamond (2.8×2.8×0.28 mm<sup>3</sup> plate from Element Six) with an initial concentration of N<sub>s</sub><sup>0</sup> below 1 ppm (sample E7). Electron irradiation at 14 MeV with doses of 10<sup>18</sup> and 10<sup>16</sup> cm<sup>-2</sup> for type-Ib and type-IIa samples, respectively, was performed at the Mainz Microtron. After electron irradiation, the samples were annealed for four hours at 700 °C in vacuum, leading to a concentration of NV<sup>-</sup> centres of around 20 ppm in E2 and around 10 ppb in E7. Before the fabrication of electrodes, the diamond crystals were cleaned and oxidized for 30 minutes in an acidic mixture of H<sub>2</sub>SO<sub>4</sub> and KNO<sub>3</sub> at 250 °C, and rinsed with ultra-pure water. Coplanar interdigitated electrodes with a distance of 15 or 100 μm were then prepared on one of the faces of the diamond crystals by lift-off photolithography and sputtering of 20 nm of titanium topped by 80 nm of aluminum. After metal sputtering, the samples were annealed in vacuum at 510°C for 3 hours to form Ohmic contact between diamond and electrodes.

For ODMR and PDMR measurements, the 532 nm illumination is produced by a linearly polarized single-mode Nd:YAG Laser (Gem 532 from Quantum Laser). For measurements on sample E2, this light is pulsed by an acousto-optical modulator (3200-146 from Crystal Technology) with a diffraction efficiency of 80 % and a contrast ratio of 1000:1. Except for the study of the influence of light pulse duration on ODMR and PDMR signal, all the measurements were performed with a pulsing frequency of 531 Hz. The pulsed light beam is focused onto the diamond surface using a 10X air objective with a numerical aperture of 0,28 and a working distance of 33,5 mm, resulting in a light spot with a diameter around 7 μm. This 7 μm light spot is positioned in the 15 or 100 μm gap separating the coplanar electrodes. Photoluminescence is measured in a non-confocal configuration. Photoluminescence light is

collected by the same objective and filtered using a dichroic mirror with a cut-on wavelength of 552 nm and a sharp-edge long-pass filter with a cut-on wavelength of 550 nm (optical density  $>5$  in the rejection region). The photoluminescence light is focused onto a pyroelectric detector. The output voltage of the pyroelectric detector is measured with a lock-in amplifier (7260 DSP from EG&G), referenced to the AOM pulsing (time constant: 50 ms). For measurements on sample E7, the 532 nm light is pulsed at a frequency of 531 Hz using a chopper wheel. The pulsed light beam is focused onto the diamond surface using an air objective with a numerical aperture of 0,82 and a working distance of 400  $\mu\text{m}$ , resulting in a light spot with a diameter around 0,8  $\mu\text{m}$ . This light spot is positioned in the 15  $\mu\text{m}$  gap separating the coplanar electrodes. The photoluminescence light is measured by an avalanche photodiode.

For photocurrent measurements on samples E2 and E7, the photo-carriers generated upon green illumination are driven towards electrodes by applying a DC voltage between coplanar contacts. For light pulses between 10 and 940  $\mu\text{s}$ , the photocurrent is amplified by a low-noise current to voltage preamplifier (SR570 from SRS, gain: 20 nA/V), and measured using a lock-in amplifier (SR830 from SRS) referenced to the AOM or chopper wheel frequency (time constant: 30 ms). The settings of the lock-in amplifier are chosen so that the magnitude of the signal vector (which does not depend on the phase between the signal and lock-in reference) is recorded. Therefore the photocurrent intensity is measured, independent of the sign of the photocurrent. Lock-in amplification leads to high signal-to-noise ratio. The photocurrent measured in our experiments was in the range of 10 pA to 1 nA and was detected with a four-digit precision. For fast photocurrent measurements (light pulses between 50 and 400 ns), the photocurrent is amplified using a charge sensitive preamplifier with a rise time of 2.5 ns and a sensitivity of 4 V/pC (A250CF CoolFET from AMPTEK INC.). The high sensitivity of this amplifier allows the detection of 48 electrons in a single pulse. The output signal of the preamplifier is measured using a digital real time oscilloscope (TDS 620B from Tektronix, Bandwidth: 500 MHz). The DC offset of the charge sensitive preamplifier was subtracted from the measured signal to obtain the data.

Microwaves of controlled frequency are produced with a 200-4000 MHz RF-signal generator (TEG4000-1 from Telemakus) with an output power of 1 mW. The microwave power is set to 40 mW, 1W or 5 W using an attenuator (TEA4000-3 from Telemakus) and a broadband amplifier with a gain of 45 dB (ZHL-16W-43+ from Mini-circuits). The microwave field is

applied using a metal wire pressed across the diamond surface and connected to a 50  $\Omega$  terminator. The metal wire is insulated from coplanar electrodes by a polymer coating. For ODMR and PDMR measurements, the microwave frequency is swept in the range 2800-2940 MHz with a step of 1 MHz. For each measurement, 100 to 200 spectra are recorded and averaged.

The static magnetic field is applied using a permanent neodymium magnet. Based on the relation between the splitting between ODMR resonances and the magnetic field magnitude, the magnitude of the magnetic field applied along the [100] is estimated to be 0,50 mT and the amplitude of the magnetic field applied along the [111] direction to be 2,0 mT.

#### 4.6.4. Results and discussion

A schematic representation of the PDMR setup is depicted in Figure 38. The principle of PDMR is demonstrated on  $NV^-$  centres ensembles, by characterizing an irradiated and annealed type-Ib single-crystal diamond plate of [100] crystallographic orientation (sample E2), containing both  $NV^-$  centres ( $\sim 20$  ppm) and substitutional nitrogen centres ( $N_s^0$ ,  $\sim 200$  ppm). Optical detection of magnetic resonance (ODMR) and PDMR were performed simultaneously on this sample. For this, the intensity of photoluminescence and photocurrent were measured simultaneously while scanning the microwave frequency in the absence and in the presence of an external magnetic field (Figure 39). Minima in the photoluminescence intensity are observed at microwave frequencies inducing resonant transitions between the  $|0\rangle$  and the  $|\pm 1\rangle$  spin sublevels of the  $NV^-$  spin triplet ground state ( $^3A_2$ ). Minima in photocurrent are clearly detected at identical frequencies, demonstrating that photocurrent measurements can be used to detect the spin resonances of  $NV^-$  centres.

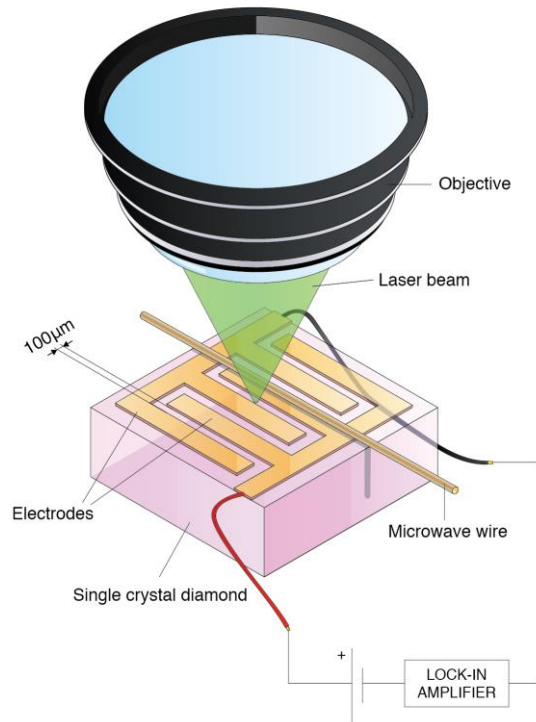


Figure 38: Schematic representation of the setup used for PDMR.

The two resonances observed in ODMR and PDMR spectra in the absence of an external magnetic field indicate the existence of a zero-field splitting (ZFS) between linear combinations of the  $|+1\rangle$  and  $|-1\rangle$  spin sublevels of  $NV^-$  (hereafter referred to as “ $|\pm 1\rangle$  spin manifold”), induced by local strain in the material (70) and, in the case of PDMR measurements, by the externally applied electric field. In the presence of an external static magnetic field applied by a permanent magnet, a further splitting of resonant frequencies is observed in both ODMR and PDMR spectrum, reflecting the perturbation of the  $|\pm 1\rangle$  spin manifold of  $NV^-$  ground state due to the Zeeman effect. As expected (174), two magnetic resonances are observed when the magnetic field is applied along the  $[100]$  direction of the diamond crystal and four when it is applied along the  $[111]$  direction (Figure 39).

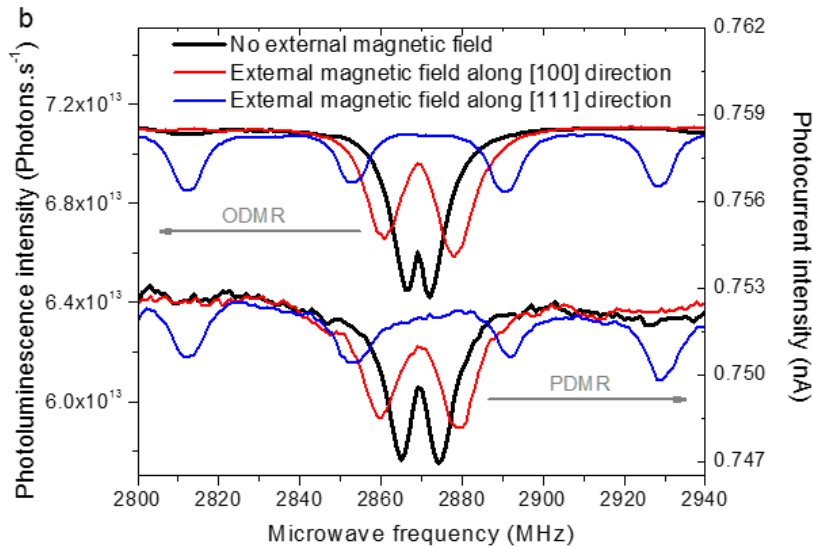


Figure 39: Comparison of ODMR and PDMR spectra recorded simultaneously (Sample E2, green light power: 100 mW, applied electric field:  $5 \times 10^4$  V/cm, light pulse duration: 940  $\mu$ s, distance between contacts: 100  $\mu$ m, magnitude of the magnetic field: 0,50 mT along the [100], 2,0 mT along the [111] direction).

To investigate the photoionization mechanism inducing the photocurrent minima at  $NV^-$  spin-resonance frequencies, the intensity of the photocurrent detected on sample E2 was measured as a function of the green light power (Figure 40). A good fit to the experimental data is obtained using the sum of a linear and a quadratic function, indicating that the measured photocurrent results from the combination of a one-photon and a two-photon ionization processes (175). In previous experiments (175) and in theoretical studies (176) it has been demonstrated that a photon energy higher than 2,6 eV is necessary to induce the photoionization of  $NV^-$  via a one-photon process, i.e. to directly promote an electron from the ground state of  $NV^-$  to the conduction band. Based on this argument and on the quadratic power dependence of the photocurrent, one can conclude that a two-photon absorption process is responsible for the  $NV^-$ -related part of the photocurrent induced by green light (2,33 eV).

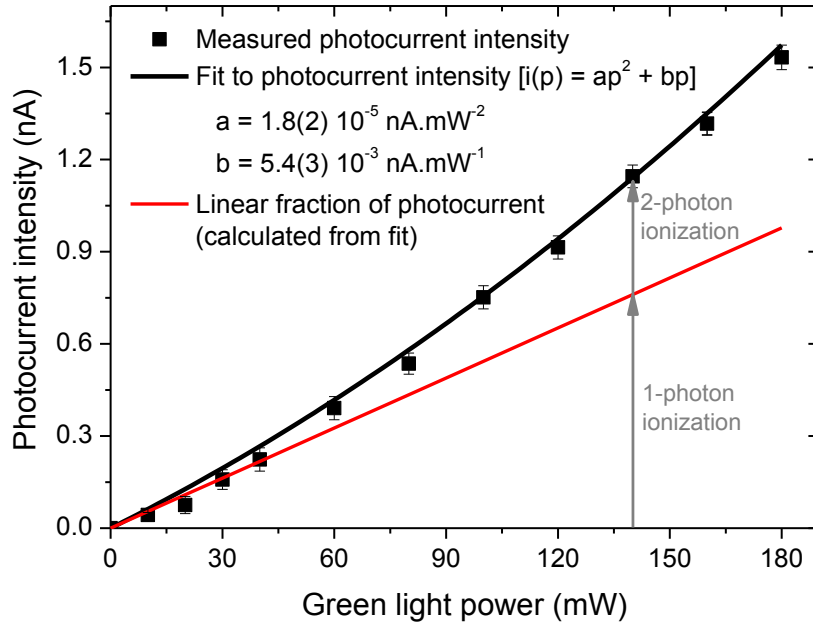


Figure 40: Photocurrent as a function of the 532 nm light power, measured on irradiated and annealed type Ib diamond (Sample E2, applied electric field:  $5 \times 10^4$  V/cm, light pulse duration: 940  $\mu$ s, distance between contacts: 100  $\mu$ m).

The mechanism for the two-photon ionization of  $NV^-$  centres in diamond has been experimentally established and modelled (177). In this process, the absorption of a first photon promotes an electron from the  $^3A_2$  triplet ground state of  $NV^-$  to its  $^3E$  triplet excited state (Figure 41a) and a second photon excites this electron to the conduction band of diamond (Figure 41b), which results in the conversion of the NV centre to its neutral state  $NV^0$  and in the promotion of an electron into the conduction band (Figure 41c). To ensure the charge neutrality in the PDMR detection circuit, the  $NV^0$  centres formed by ionization of  $NV^-$  have to be subsequently converted back to the  $NV^-$  state, either by capturing an electron from a donor defect (in particular from  $N_s^0$ , present in high concentration in the type Ib sample under study) (27) or by two-photon conversion from  $NV^0$  to  $NV^-$  (Figure 41d). In the latter process, the absorption of a first photon excites the  $NV^0$  centre, while a second photon promotes an electron from the valence band to the vacated orbital of  $NV^0$ , leaving a hole in the valence band (175). This photo-induced process does not require the presence of electron-donor defects in the diamond crystal. The linear contribution to the measured photocurrent (Figure 40) is likely associated with one-photon ionization of  $N_s^0$ .  $N_s^0$  is indeed the dominant point defect in the E2 sample, and the threshold energy for the photoionization of this defect is well below the 2,33 eV excitation energy used in our experiment (178).

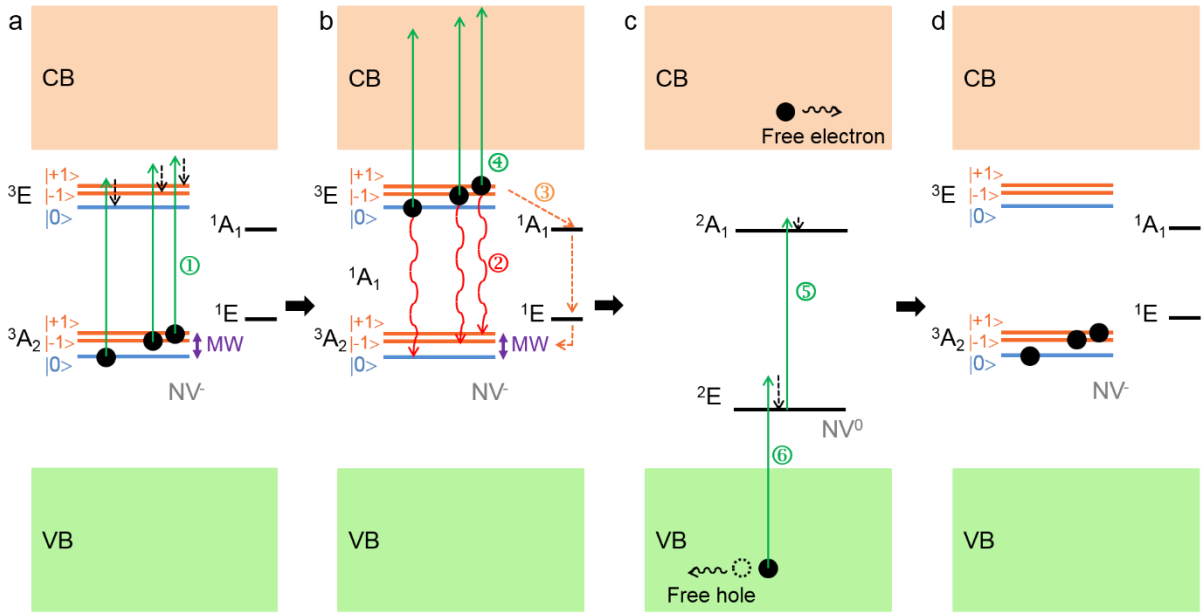


Figure 41: Simplified electronic energy level scheme of the  $NV^-$  centre at room temperature (not to scale) and description of the mechanism proposed to explain PDMR measurements. (a) The absorption of a first photon promotes an electron from the  $^3A_2$  ground state to the  $^3E$  state of  $NV^-$ . From  $^3E$ , electrons can radiatively decay back to  $^3A_2$  or be excited to the diamond conduction band (CB) by the absorption of a second photon. (b) The spin-selective non-radiative decay of electrons to the metastable singlet state  $^1A_1$  enables PDMR and ODMR. (c) The two-photon ionization of  $NV^-$  results in the formation of a  $NV^0$  centre and a free electron in the CB. (d) By a two-photon process the  $NV$  centre can finally be converted back to its negatively charged state.

The mechanism proposed to explain the photoelectric detection of  $NV^-$  magnetic resonances is presented in Figure 41. The minima observed in the photocurrent at resonant MW frequencies inducing transitions from the  $|0\rangle$  to the  $|\pm 1\rangle$  electron spin sublevels of  $NV^-$  ground state ( $^3A_2$ ) indicate that the photoionization dynamics of  $NV^-$  is spin-dependent. In ODMR, electrons are initially pumped into the  $^3A_2 |0\rangle$  spin state under the effect of green illumination, from which they are coherently driven to the  $^3A_2 |\pm 1\rangle$  spin sublevels by the resonant microwave field (179). Photoluminescence originates from the radiative decay of electrons from the excited state ( $^3E$ ) to the ground state. Due to spin-selective intersystem crossing, electrons in the  $^3E |\pm 1\rangle$  sublevels can decay non-radiatively to the  $^1A_1$  singlet state (lifetime  $\leq 1$  ns (38)) from which they further fall into the  $^1E$  metastable singlet state (electron shelving). This non-radiative decay path induces a difference between the brightness of the transitions associated with the different  $NV^-$  spin sublevels, which provides the contrast monitored by ODMR.

For PDMR, it is expected that electron shelving is also the dominant mechanism explaining the observed contrast. Electrons excited to the  $^3E |\pm 1\rangle$  sublevels have a non-zero probability to undergo the shelving transitions via the  $^1A_1$  and  $^1E$  states. For the time during

which an electron initially in the  $^3A_2 |\pm 1\rangle$  state undergoes these non-radiative transitions, it does not contribute to the photocurrent. Specifically, the  $^1E$  metastable state has a lifetime of 220 ns at room temperature (38). For that period, the  $^1E$  state stores the electron which leads to a temporary decrease in the occupation of  $NV^-$  ground state and reduces the rate of two-photon ionization (proportional to the occupation of  $^3A_2$ ). This process probably induces the observed magnetic resonances in photocurrent. An alternative photoionization path would be the direct promotion of electrons from the  $^1E$  metastable state to the conduction band. This ionization path would lead to a positive sign of PDMR, since electrons in the  $^1E |\pm 1\rangle$  sublevels have a higher probability to decay non-radiatively to the singlet state, which leads to a higher occupation of the  $^1E$  metastable state. However, the negative resonances observed in PDMR spectra suggest that the contribution of this photoionization process to the total photocurrent at the resonant microwave frequency is significantly lower than the contribution of direct transitions from the excited state  $^3E$  to the conduction band.

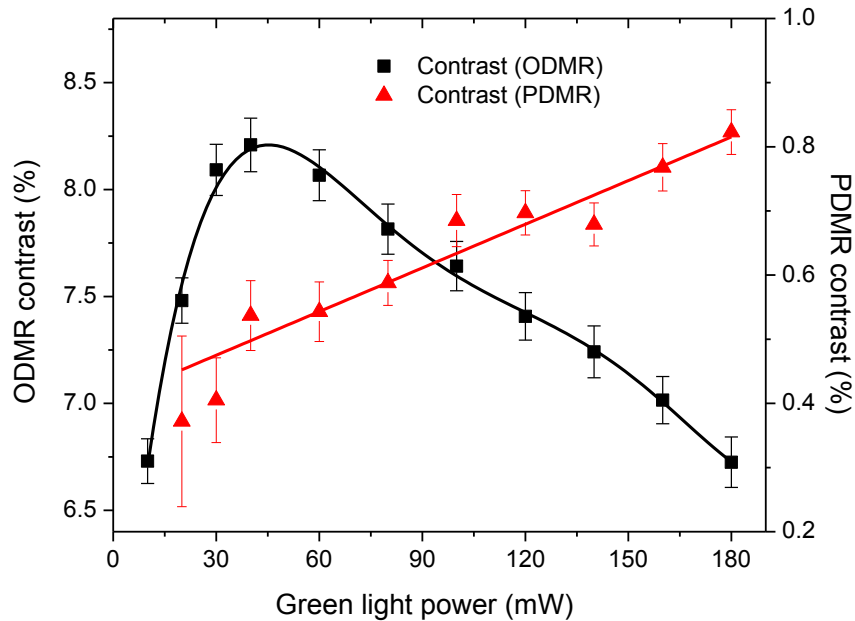


Figure 42: Dependence of the ODMR and PDMR contrast on 532 nm light power (Sample E2, applied electric field:  $5 \times 10^4$  V/cm, light pulse duration: 940  $\mu$ s, distance between contacts: 100  $\mu$ m). Solid lines are a guides for the eye.

Figure 42 depicts the dependence of the ODMR and PDMR contrasts measured on sample E2 on the green light power. The maximal observed contrasts are  $\sim 0.8$  % for PDMR and 8.2 % for ODMR. This is partly due to the fact that only the two-photon fraction of the photocurrent (associated with the ionization of  $NV^-$ ) gives rise to detectable electron spin resonances, while its linear fraction is not affected by the microwaves. In the case of PDMR

measurements performed on type-Ib diamond, a monotonous increase of the PDMR contrast with the light intensity is observed. However, under strong optical pumping, shelving transitions to the  $^1E$  singlet state should saturate, which probably explains the decrease in the ODMR contrast observed for green light powers above 45 mW. The absence of saturation detected in the PDMR contrast can be explained by the fact that increasing the light power leads to an increase in the quadratic fraction of the photocurrent (associated with ionization of  $NV^-$  centres) with respect to the linear fraction (associated with ionization of  $N_S^0$ ). However, while the quadratic fraction of the photocurrent increases by a factor four between 30 mW and 180 mW (Figure 40), the PDMR contrast only increases by a factor of two, which seems to reflect the saturation of shelving transitions to the  $^1E$  singlet state, as discussed above. For a quantitative evaluation of this phenomenon, the shelving rate and the two-photon ionization rate have to be further investigated.

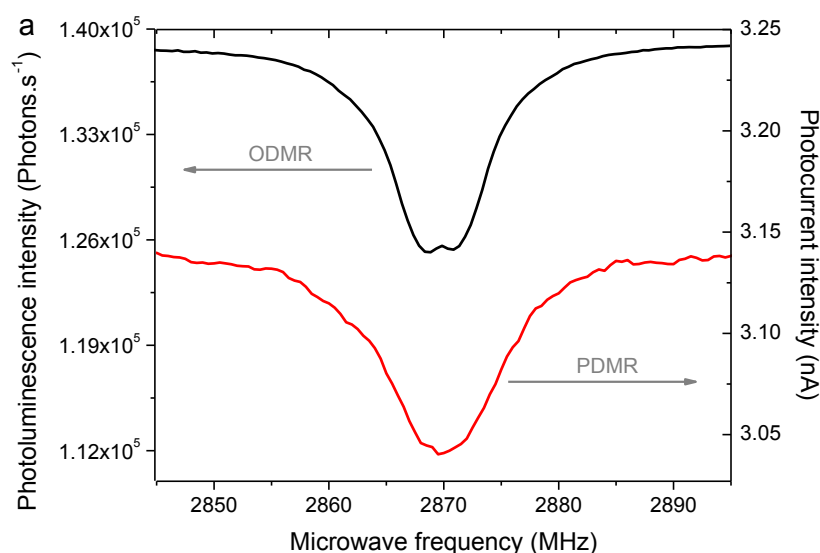


Figure 43: Comparison of ODMR and PDMR spectra measured simultaneously in the absence of magnetic field on irradiated and annealed type-IIa diamond (Sample E7, light pulse duration: 940  $\mu$ s, applied electric field:  $3,3 \times 10^4$  V/cm, distance between contacts: 15  $\mu$ m, green light power: 6 mW).

An electron-irradiated and annealed optical grade diamond with estimated  $N_S^0$  concentration below 1 ppm and  $NV^-$  concentration around 10 ppb (sample E7) was used, to demonstrate the possibility of performing PDMR with  $NV^-$  ensembles in type-IIa diamond with low  $N_S^0$  concentration. It was possible to detect the  $NV^-$  spin electron resonance in the photocurrent measured on this sample (PDMR spectrum compared with ODMR spectrum in Figure 43). The light power-dependence of the photocurrent detected on this sample is presented in Figure 44. The experimental data can be fitted with the sum of a quadratic function

(corresponding to a two-photon ionization process) and a linear function (corresponding to a one-photon ionization process). By comparing with the photocurrent measured on type-Ib diamond (Figure 40), it appears that the ratio between the linear and quadratic pre-factors  $b$  and  $a$  (Figure 44) is about 300 times lower for type-IIa diamond than for type-Ib diamond. This suggests that in the volume of sample E7 contributing to the photocurrent, the concentration of  $N_s^0$  defects is low and that a nearly pure two-photon ionization process occurs, without major contribution from the ionization of  $N_s^0$  defects to the photocurrent. Correspondingly, a higher PDMR contrast is obtained on type-IIa than on type-Ib diamond. Indeed, a contrast of 3 % was observed on type-IIa diamond in optimal conditions. This result shows that, as expected, the PDMR technique is more efficient on type-IIa diamond than on type-Ib diamond, due to the lower contribution of  $N_s^0$  photoionization to the total photocurrent.

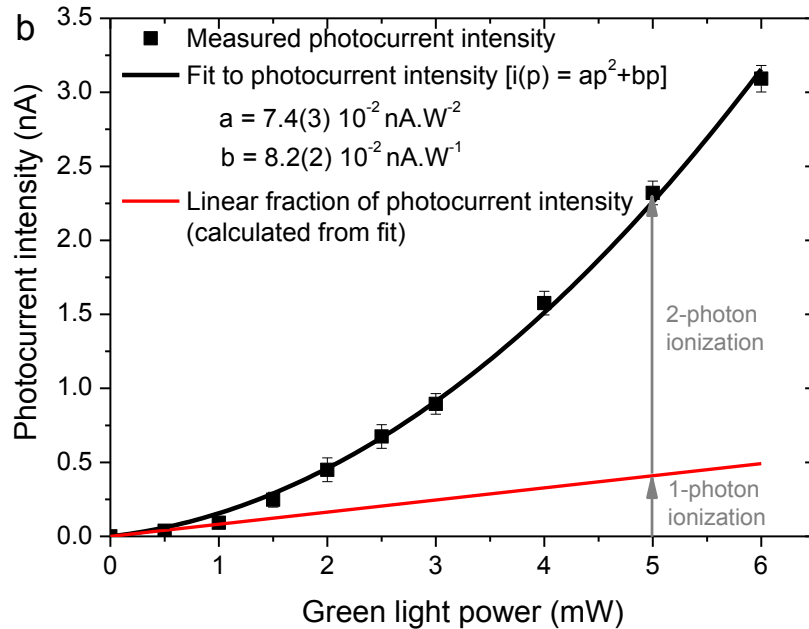


Figure 44: Photocurrent as a function of the 532 nm light power, measured on irradiated and annealed type-IIa diamond (Sample E7, light pulse duration: 940  $\mu$ s, applied electric field:  $3,3 \times 10^4$  V/cm, distance between contacts: 15  $\mu$ m).

To investigate the bandwidth of the photoelectric detection technique and to demonstrate the possibility to employ it for pulsed spin detection experiments (Ramsey or Rabi oscillations, spin-echo experiments, etc.), faster photocurrent measurements were performed with the E2 sample. The photoelectric detection of spin magnetic resonances was achieved using light pulses down to 10  $\mu$ s, with lock-in amplification of the photocurrent. No significant effect of the reduction of light pulse duration on the linewidth and contrast of photocurrent resonances was observed. The detection of the photocurrent induced by light pulses as short as

50 ns was in addition achieved using a charge sensitive preamplifier instead of the lock-in technique. This demonstrates the possibility to perform a fast readout of the photocurrent and shows that the photoelectric detection method may be used for pulsed spin-resonance experiments, for which read-out laser pulses between 200 and 500 ns are typically used (180).

#### 4.6.5. Conclusion

In conclusion, a new principle for the read-out of NV<sup>-</sup> centres spin magnetic resonances in diamond has been demonstrated. By reducing the contact area, this technique has the potential to address single NV<sup>-</sup> centres. This paradigm may lead to a sensitive way for the construction of diamond nanoscale sensors and quantum devices and their read-out, allowing directly performing quantum operation on a chip.

#### **Acknowledgment**

This work was supported by the AFOSR/DARPA QuASAR program, The Research Foundation - Flanders (FWO) (Grant agreement G.088812N), the European Union Seventh Framework Programme (FP7/2007-2013) under the project DIADEMS (grant agreement n°611143), the Ministry of Science and Education of the Czech Republic (Contract CZ.1.07/2.3.00/20.0306), the German-Israeli Project Cooperation (DIP) program and NSF (Grant No. ECCS-1202258). The authors are grateful to P. Kehayias for helpful discussions, to K. Aulenbacher and the MAMI staff for electron irradiation, and to Y. Balasubramaniam and P. Robaeys for electrodes fabrication.

## 4.7. Enhanced dual-beam excitation photoelectric detection of NV magnetic resonances in diamond

This work has been published in **Physical Review B** journal (**IF = 3.718**) and the article is reprinted here with changes. Authors are: E. Bourgeois, E. Londero, K. Buczak, J. Hruby, M. Gulka, Y. Balasubramaniam, G. Wachter, J. Stursa, K. Dobes, F. Aumayr, M. Trupke, A. Gali, and M. Nesladek. Here the dual-beam excitation scheme for PDMR was developed with aim to improve the detection capabilities of PDMR method by enhancing the measured MW resonant contrast and detection rates. This is necessary for implementation of PDMR techniques in quantum sensing and quantum information applications. I have contributed to this study by a thorough analysis of the MW resonance signal strength. By varying the PDMR parameters (including triggering frequency, lock-in time constant, microwave and laser power, applied voltage, detection frequency filters, sensitivity of the pre-amplification etc.), I made it possible to detect PDMR with higher signal-to-noise ratio, thus reducing the measurement times. I was also helping E. Bourgeois with the PDMR measurements. All other work was done by remaining authors of the paper. Final PDMR measurements that are presented in the paper were done at Institute for Materials Research, Hasselt University, Belgium.

### 4.7.1. Abstract

The core issue for the implementation of the diamond NV centre qubits technology is the sensitive readout of NV spin state. Recently the photoelectric detection of NV magnetic resonances (PDMR) was demonstrated, anticipated to be faster and more sensitive than optical detection (ODMR). Here a PDMR contrast of 9 % - three times enhanced compared to previous work - on shallow N-implanted diamond is reported. A novel one-photon ionization PDMR protocol based on ab-initio modelling is demonstrated. This dual-beam scheme is predicted to be significantly less vulnerable to the influence of defects such as substitutional nitrogen.

### 4.7.2. Introduction

The negatively charged nitrogen-vacancy ( $NV^-$ ) centre in diamond has attracted particular attention as a room temperature solid state qubit (181) that can be readout by optical detection of magnetic resonances (ODMR) (99). Numerous applications in the field of solid-state quantum information processing (169) and sensing (107; 70) are being studied, including non-perturbing nanoscale magnetometry with single  $NV^-$  (85) and ultrasensitive magnetometry with  $NV^-$  ensembles (2).

Recently the photoelectric detection of  $NV^-$  electron spin magnetic resonances under green illumination (single-beam PDMR, or s-PDMR) was demonstrated (Figure 45a), based on the electric detection of charge carriers promoted to the diamond conduction band (CB) by the ionization of  $NV^-$  and performed directly on a diamond chip equipped with electric contacts (128). Since the sensitivity of the magnetic resonance (MR) detection is inversely proportional to the product between the MR contrast and the root mean square of the number of detected photons  $N_p$  or electrons  $N_e$  (128; 70), achieving a high photocurrent signal and a sufficient MR contrast is critical for further applications of PDMR in quantum technology. Using s-PDMR, a detection rate of  $\sim 10^7$  electrons. $s^{-1}$  per  $NV^-$  was achieved (N.A. of the objective: 0.95, green illumination: 3.4 mW, electric field:  $2.4 \cdot 10^4$  V  $cm^{-1}$ ), compared to  $2 \cdot 10^4$  photons. $s^{-1}$  per  $NV^-$  using confocal ODMR detection. However, the one-photon ionization of single substitutional nitrogen ( $N_S^0$ ) is one of the factors limiting the PDMR contrast, making a high green illumination power necessary to achieve a sufficient contribution of  $NV^-$  two-photon ionization to the total photocurrent (128). It was observed that under blue illumination, the ionization of  $NV^-$  can be achieved by a more effective one-photon process, enhancing the proportion of the photocurrent associated with  $NV^-$  compared to  $N_S^0$ . Based on this idea, the dual-beam excitation PDMR (d-PDMR) scheme (Figure 45a) was developed, that is anticipated to lead to enhanced PDMR contrast in the case of samples with high  $[N_S^0]/[NV^-]$  ratio and could therefore hold promise for the photoelectric readout of single  $NV^-$  spin (since the proportion of  $N_S^0$  in the detection volume remains substantial even in the case of single  $NV^-$  centres contained in ultra-pure diamond) or for ultrasensitive diamond magnetometry with  $NV^-$  ensembles (for which irradiated type-Ib diamonds containing a high proportion of  $N_S^0$  are used).

To determine the threshold for  $NV$  and  $N_S^0$  one-photon ionization, first the photocurrent spectra of irradiated type-Ib diamonds was measured. Based on the identification of the ionization bands, the d-PDMR scheme was designed, in which pulsed blue light (2.75 eV) directly promotes electrons from  $NV^-$  ground state to the CB and converts the resultant  $NV^0$  back to  $NV^-$ . Simultaneous CW green illumination (2.33 eV) independently controls the MR contrast by inducing spin-selective shelving transitions to  $NV^-$  metastable state (182). By performing ab-initio calculations of  $N_S^0$ ,  $NV^-$  and  $NV^0$  ionization cross-sections, it was possible to explore the photo-physics related to the proposed scheme, relevant for achieving higher MR contrast and photocurrent signal.

### 4.7.3. Methods and materials

The sample used for PDMR measurements (sample TP4) is an electronic grade type-IIa diamond implanted with  $^{14}\text{N}^{4+}$  ions, resulting after annealing in the formation of a shallow  $\text{NV}^-$  layer (density  $\sim 30 \mu\text{m}^{-2}$ , depth:  $12 \pm 4$  nm). For photocurrent spectroscopy, an as-received type-Ib diamond plate (sample R,  $[\text{N}_\text{s}^0] \sim 160$  ppm) was used as a reference, while two others were respectively proton- (sample A,  $[\text{NV}^-] \sim 35$  ppm) and electron-irradiated (sample E2,  $[\text{NV}^-] \sim 20$  ppm) and annealed. Coplanar electrodes with a distance of  $100 \mu\text{m}$  (samples R, E2 and A) or  $50 \mu\text{m}$  (sample TP4) were prepared on the surface of these diamond plates. The type-Ib samples were characterized by photoluminescence, FTIR and UV-visible absorption spectroscopy.

To realize the d-PDMR scheme, a DC electric field ( $2.4 \cdot 10^4 \text{ V cm}^{-1}$ ) is applied in between electrodes. A collimated blue (2.75 eV) laser beam, pulsed at 131 Hz, is focused in between electrodes onto the diamond surface using a 40X air objective (NA: 0.95, light spot diameter  $\sim 600$  nm). CW green (2.33 eV) light produced by a linearly polarized Nd:YAG laser is combined with the blue beam using the same objective. The resulting photocurrent is pre-amplified and measured by a lock-in amplifier referenced to the blue light pulsing frequency, so that the photocurrent induced by CW green light does not contribute to the measured signal. The diamond chip is mounted on a circuit board equipped with microwave antennas (183). For photocurrent spectroscopy, monochromatic light (1 to  $300 \mu\text{W}$ ) pulsed at 12 Hz is focused onto the sample. At each photon energy, the photocurrent is pre-amplified and measured by lock-in amplification (photocurrent detected down to 3 fA). The photocurrent is normalized to the flux of incoming photons.

### 4.7.4. Results and discussions

To gain insight into  $\text{NV}^-$ ,  $\text{NV}^0$  and  $\text{N}_\text{s}^0$  photo-ionization mechanisms, ab-initio Kohn-Sham density functional theory (DFT) calculations was applied. In the photo-ionization process, an electron is excited from an in-gap defect level to the CB or from the valence band (VB) to an in-gap defect level. In our measurements, a bias voltage is applied to the sample, making the resultant electron or hole instantly leave the defects. The photo-ionization probability is then directly proportional to the absorption cross-section that depends on the imaginary part of the dielectric function related to the transition between the initial ground state and the final excited state. This process can be well approximated by the transition of a single electron from/to the in-gap defect level to/from the band edges, thus the imaginary part of the dielectric function can be calculated between the corresponding Kohn-Sham levels. In

summary, the task is to calculate the excitation energies and the corresponding imaginary part of the dielectric function.

To this end, the lowest excitation energy that corresponds to the pure electronic transition [zero-phonon line (ZPL) energy] was calculated by the constraint DFT approach. Based on the previous studies (184), a range-separated and screened hybrid density functional HSE06 (185) was used. The ZPL energies were explicitly calculated only for the band edges, and assumed that the excitations at higher energy follow the calculated band energies with respect to the band edge energy. The imaginary part of the dielectric function is calculated at the ground state geometry, following the Franck-Condon approximation. Optical transitions to the bands require accurate calculation of the electron density of states. Since HSE06 calculations with many k-points in the Brillouin-zone are computationally prohibitive, and given that PBE and HSE06 Kohn-Sham wave functions are very similar for  $N_S$  and NV centres, a generalised gradient approximated functional PBE was applied to calculate their optical transition dipole moments (186). The defects were modelled in a 512-atom diamond supercell.

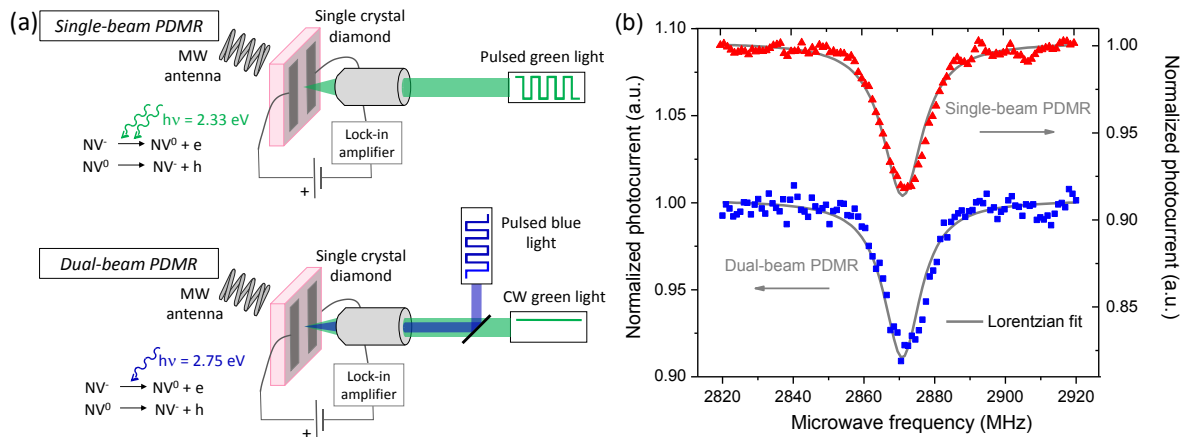


Figure 45: (a) Schematic diagram of the s-PDMR and d-PDMR schemes (b) Comparison between d-PDMR (pulsed blue excitation:  $226 \mu\text{W}$ , CW green excitation:  $9.1 \text{ mW}$ ) and s-PDMR (pulsed green excitation:  $3 \text{ mW}$ ) spectra measured on shallow  $NV^-$  ensembles, in the conditions leading to maximum MR contrast (sample TP4, microwave power:  $1 \text{ W}$ ).

The proposed d-PDMR scheme was tested on shallow  $NV^-$  ensembles implanted in electronic grade diamond (sample TP4). As a reference, s-PDMR was measured on the same sample. At a fixed microwave power of  $1 \text{ W}$ , a maximum s-PDMR contrast of  $8.9 \pm 0.3 \%$  was obtained (Figure 45b), higher than the PDMR contrast previously observed on irradiated type-Ib and type-IIa diamonds (128). Under green illumination the PDMR contrast is limited by the background photocurrent resulting from the ionization of  $N_S^0$  (128). The enhanced s-PDMR

contrast observed on sample TP4 can be explained by the higher contribution of the quadratic NV two-photon ionization to the total photocurrent, which is attributed to the confinement of the defects to the waist of the illumination beam – where the intensity is highest. By contrast, the illumination intensity in bulk samples decreases with depth, leading to a higher proportion of linear  $N_S^0$  ionization in the total photocurrent.

A maximum d-PDMR contrast of  $9.0 \pm 0.4$  % is obtained on sample TP4 (Figure 45b), close to the maximum s-PDMR contrast observed on the same sample at identical microwave power. Measurements of photocurrent as a function of green and blue light power on sample TP4 show in addition that at identical power, blue one-photon excitation induces higher photocurrent than green excitation. For example, the photocurrent measured under 226  $\mu$ W excitation (conditions leading to maximal d-PDMR contrast) is five times higher under blue (800 fA) than under green light (165 fA). Although on shallow implanted  $NV^-$  ensembles the MR contrasts obtained by d-PDMR and s-PDMR are similar, the d-PDMR scheme could potentially lead to higher contrast than s-PDMR in case of samples with high  $[N_S^0]/[NV^-]$  ratio, due to the lower contribution of  $N_S^0$  ionization to the total photocurrent under blue illumination. Indeed, considering the green light power dependence of the photocurrent measured on type-Ib sample E2, under 4 mW green excitation the two-photon ionization of NV (quadratic fraction of the photocurrent) represents only  $\sim 1.5$  % (0.6 pA) of the total detected photocurrent, while ab-initio calculations indicate that under 4 mW blue illumination  $\sim 30$  % (0.6 nA) of the total photocurrent originates from the 1-photon ionization of  $NV^-$ .

To explore the mechanism behind the d-PDMR scheme, the energy dependence of NV and  $N_S$  photo-ionization cross-sections were studied by photocurrent spectroscopy. These measurements were performed on irradiated and annealed type-Ib diamonds, since a high density of defects allows to reach a high dynamic range of detected photocurrent, leading to a precise determination of photo-ionization thresholds. The photocurrent spectrum measured on a type-Ib reference diamond (sample R,  $[N_S^0] \sim 160$  ppm) can be observed in Figure 46a. This spectrum displays a photo-ionization band with a threshold ionization energy of  $\sim 2.2$  eV, obtained by fitting experimental data to Inkson's formula for the photo-ionization cross-section of deep defects (187). This band corresponds to the ionization of  $N_S^0$  to  $N_S^+$  (188). Though its calculated (+|0) pure electronic charge transition level is at  $E_C - 1.7$  eV ( $E_C$ : CB minimum) the giant redistribution of position of the N and C atoms in the core of the defect upon ionization of  $N_S^0$  results in a low ionization cross-section at this energy. Due to very strong electron-

phonon interaction, a photo-ionization band emerges in the phonon sidebands around  $E_C-2.2$  eV (see (189) for further discussion).

Compared to non-irradiated diamond, the photocurrent spectra measured on proton- and electron-irradiated type-Ib diamonds (samples A and E2, in which  $\sim 10\%$  of  $N_S$  defects are converted to  $NV^-$  centres) show a blue shift and the formation of an ionization band with threshold at  $\sim 2.7$  eV (Figure 46a). Photoluminescence, FTIR and optical absorption spectroscopy indicate that the dominant defects in these samples are  $N_S$  and  $NV$ , with some additional spurious defects (possibly associated to Ni) in sample A.

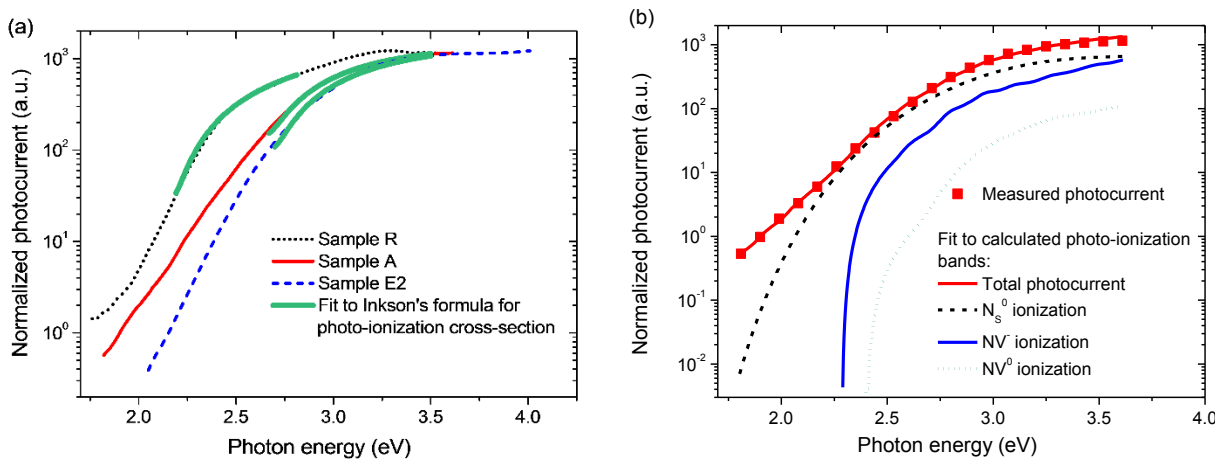


Figure 46: (a) Comparison between photocurrent spectra measured on reference type-Ib diamond (sample R,  $E_i = 2.18$  eV) and irradiated and annealed type-Ib diamonds (samples A,  $E_i = 2.66$  eV; sample E2,  $E_i = 2.69$  eV).  $E_i$ : threshold ionization energy from Inkson's fitting. (b) Fitting of photocurrent measured on sample A using calculated ionization cross-sections. The contributions of  $N_S^0$ ,  $NV^-$  and  $NV^0$  ionizations to the total photocurrent are shown. In the ab-initio calculation it was assumed that  $NV^-$ ,  $NV^0$  and  $N_S^0$  ionization dominates the spectrum, with other parasitic defects contributing to a small extent to the spectrum in the low energy region (not shown).

The ionization cross-sections of  $N_S$  and  $NV$  defects were calculated as a function of the photo-excitation energy and compared the results with the photocurrent measurements (Figure 46b for sample A). In the simulation plots the experimental value of  $[N_S^0]$  was set and  $[NV^0]$  and  $[NV^-]$  was fitted to the experimental data. Using only these two fitting parameters values of  $[NV^-] \approx 31.4$  ppm and  $[NV^0] \approx 1.0$  ppm were obtained in sample A, in excellent agreement with the concentrations determined from photoluminescence measurements ( $[NV^-] \approx 34.0$  ppm and  $[NV^0] \approx 1.1$  ppm). Our ab-initio calculations predicted (190) that the  $(0|-)$  acceptor level of  $NV$  lies just in the middle of the diamond gap, at  $E_C-2.75$  eV. Unlike  $N_S$ ,  $NV^0$  and  $NV^-$  present very similar geometries, thus pure electronic transitions dominate the ionization process. Photons with an energy above 2.7 eV can therefore ionize  $NV^-$  to  $NV^0$  by promoting an electron to the CB, but also convert  $NV^0$  back to  $NV^-$  by direct promotion of an electron from the VB.

Calculations predict in addition that  $NV^0$  has  $\sim 10$  times larger ionization cross-section than  $NV^-$  at 2.75 eV, implying a larger rate for the back-conversion than for the ionization of  $NV^-$ .

Based on the results of photocurrent spectroscopy and ab-initio calculations, the d-PDMR scheme is explained as follows (Figure 47a). Pulsed blue light (2.75 eV) promotes electrons from  $NV^-$  triplet ground state  $^3A_2$  to the CB by a one-photon process (transition 1), and induces also the one-photon back-conversion from  $NV^0$  to  $NV^-$  (transition 4). Simultaneous illumination by CW green laser light (2.33 eV) induces transitions from the ground state  $^3A_2$  to the excited state  $^3E$  (transition 2), followed by spin-selective non-radiative decay from the  $|\pm 1\rangle$  spin manifold of  $^3E$  to the singlet state  $^1A_1$  (transition 3) (182). From there, electrons fall to the metastable state  $^1E$  (220 ns lifetime) (91). At resonant microwave frequency (2.87 GHz), these shelving transitions result in a temporary decrease in the occupation of  $NV^-$  ground state, and thus to a decrease in the photocurrent associated with the one-photon ionization of  $NV^-$ . Here it was assumed that the photo-ionization cross-section from the  $^1E$  shelving state to the CB is low, although the metastable state  $^1E$  state has been recently estimated to be located  $\sim 0.4$  eV above  $NV^-$  ground state (i.e.  $\sim 2.3$  eV below the CB) (191) and could therefore theoretically be ionized by 2.75 eV photons. However, the negative resonances observed in d-PDMR (Figure 45b) indicate that the contribution of this process to the total photocurrent is significantly lower than the contribution of direct transitions from  $NV^-$  ground state to the CB.

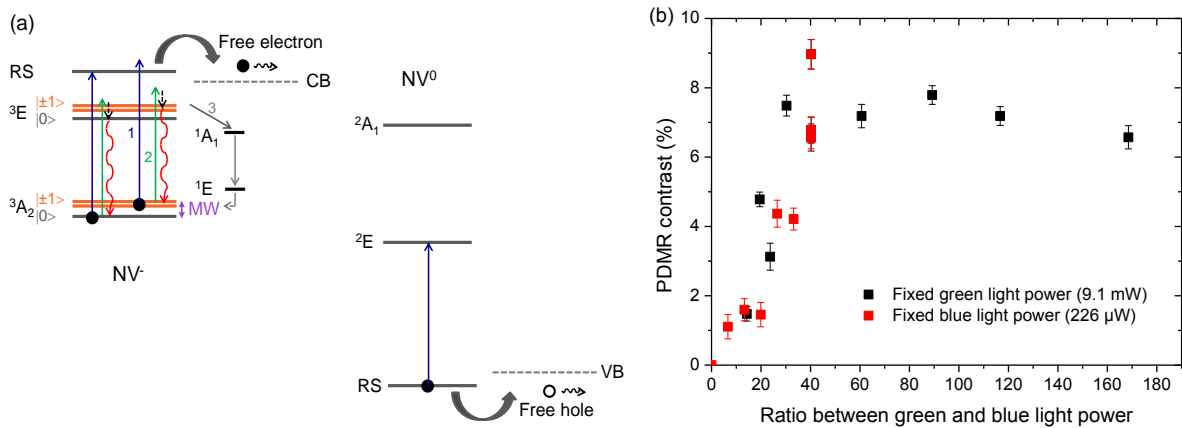


Figure 47: (a) Schematic diagram of the d-PDMR mechanism (not to scale). Left: one-photon ionization of  $NV^-$ . Right: Back-conversion from  $NV^0$  to  $NV^-$ . RS: resonant state. (b) d-PDMR contrast measured on shallow  $NV^-$  ensembles as a function of the ratio  $R_{GB}$  between the green and blue light powers (sample TP4). Error bars represent the standard errors of the fitting parameters.

Our d-PDMR model indicates that the relative rates between the direct ionization, back-conversion and shelving transitions to the metastable state, which can be controlled by varying the ratio  $R_{GB}$  between the green and blue light powers, are dominantly responsible for the PDMR contrast. At a fix microwave power (1 W in the presented experiments), the PDMR

contrasts obtained by varying the green light power at constant blue power and by varying the blue power at constant green power present a similar trend (Figure 47b). In the range of laser power considered here and for  $R_{GB} < 40$ , the d-PDMR scheme allows thus an independent control of the photocurrent intensity (by the blue light power) and the MR contrast (by  $R_{GB}$ ). The initial increase in the d-PDMR contrast with  $R_{GB}$  ( $R_{GB} \leq 40$ ) can be explained by the transfer of an increased proportion of electrons initially in the  $|\pm 1\rangle$  spin manifold to the metastable state. Above  $R_{GB} \approx 40$ , the contrast saturates and slightly decreases. It should be noted that this effect does not result from the saturation of the singlet state  $^1E$ , since it occurs when the blue light power is reduced at fixed green light power.

#### 4.7.5. Conclusion

In conclusion, it was demonstrated that a one-photon ionization scheme can be used for reading out the spin state of  $NV^-$ . Based on this principle, a novel photoelectric scheme for the detection of  $NV^-$  magnetic resonances was designed, in which blue illumination induces the one-photon ionization of  $NV^-$  and converts  $NV^0$  back to  $NV^-$ , while the MR contrast is independently controlled by CW green light. A maximal PDMR contrast of 9.0 % was obtained on shallow  $NV^-$  centres implanted in electronic grade diamond. The d-PDMR scheme is expected to be less sensitive than s-PDMR to background defects in diamond and to lead thus to enhanced MR contrast in the case of samples with high  $[Ns^0]/[NV^-]$  ratio. This robust photoelectric detection scheme could therefore represent an important step toward the photoelectric readout of single  $NV^-$  spin state and be used for the construction of diamond quantum opto-electronics devices with enhanced performances.

#### Acknowledgements

Support from EU (FP7 project DIADEMS, grant No. 611143) is acknowledged. A. G. acknowledges the Lendület program of the Hungarian Academy of Sciences. The authors thank A. Jarmola and D. Budker from the Department of Physics of the University of California (Berkeley, California) for the preparation of the electron-irradiated type-Ib diamond.

## 4.8. Pulsed photoelectric coherent manipulation and detection of NV centre spins in diamond

This work has been accepted in Physical Review Applied journal (**IF = 4.061**) and the article is reprinted here with changes. Co-authors of the work are: E. Bourgeois, J. Hruby, P. Siyushev, G. Wachter, F. Aumayr, P. R. Hemmer, A. Gali, F. Jelezko, M. Trupke, M. Nesladek. Three main issues were examined here; removal of N-related background photocurrent, thus enhancing the detection contrast and S/N ratio, applicability of PDMR method for pulsed measurements, and downscaling of the number of NV centres detected by PDMR. As a main author of this work I have executed all measurements of which results are presented here. I have developed and tested the pulse protocols and the MW-triggering scheme. I have installed new hardware to enable the pulsed excitation and I have carried out the PDMR noise calculations for lock-in detection scheme. The sample used for the experiments was prepared at TU Wien without my contribution.

### 4.8.1. Abstract

I demonstrate hybrid photoelectric pulse protocols for reading the spin states of NV centres in diamond, compatible with coherent spin control and performed on shallow nitrogen-implanted electronic grade diamond. The measurements are carried out on spin ensembles from 1000 to just 5 NV centres, as a first step towards the fabrication of scalable photoelectric quantum chips. Specific MW protocols are developed that suppress background photocurrent related to ionization of NS0 defects and provide a high contrast and S/N ratio. The technique is demonstrated on Rabi and Ramsey sequences.

### 4.8.2. Introduction

Hybrid quantum detection approaches are considered as the most promising towards the realisation of scalable systems for quantum computation (192). Here I demonstrate coherent manipulation and photoelectric readout of nitrogen-vacancy (NV) spin states in diamond as a basic building block for scalable miniaturized electric quantum devices (193). I develop novel spin photoelectric readout protocols compatible with preparation and readout of arbitrary quantum states of NV centres in diamond. By providing MW triggering for lock-in detection of the photocurrent, I suppress photocurrent generated from ionization of single substitutional nitrogen  $N_S^0$ . The presented technique allows for high readout contrast with the offset due only

to the electronic noise - up to high frequencies of  $\sim 20$  MHz. The high sensitivity of the proposed protocols allows to read the spin state of  $\sim 5$  NV centres.

NV solid state qubits in diamond are one of the most studied quantum materials today due to the record spin coherence time at room temperature (30) and are used for quantum sensing application (e.g. magnetometry (85), thermometry (194), single spin nano-MRI (93)). The optically detected magnetic resonance (ODMR) method (127) used as a major technique for NV centres in diamond has important limitations in the scalability and does not provide integration with electrical readout. Recently we have introduced the photoelectrically detected magnetic resonance (PDMR) technique (128) for reading out the electron spin state of negatively charged NV centre in diamond. This method provides a vast enhancement of over 2.5 orders of magnitude in detection rates compared to ODMR measured in similar experimental conditions (see 4.7 for details). Although we have demonstrated the principle of this method, it was only used for CW readout of the  $|0\rangle$  and  $|\pm 1\rangle$  spin states of NV ensembles in lab-grown CVD or HPHT diamonds (128). In order to use the advantages of the PDMR technique in quantum sensing and computational schemes, it is necessary to demonstrate that the photoelectric readout is compatible with the quantum control of individual NV electron spins. Here, I perform coherent operations with PDMR on spin ensembles of just a few ( $\sim 5$ ) NV centres by designing specific readout sequences. I demonstrate these protocols by performing Rabi and Ramsey measurements on shallow NV ensembles implanted in electronic grade diamond, that is, unlike bulk crystals, a material suitable for future quantum devices. The proposed method leads to a significant suppression of background photocurrents, which is one of the main limiting factors for using PDMR for readout of single NV sites (128; 195), and considerably increased signal-to-noise (S/N) ratio compared to CW PDMR measurements (128; 196). By this way I could experimentally verify the S/N ratio that were previously only theoretically predicted (197).

#### 4.8.3. Methods and materials

Figure 48a depicts the hybrid photoelectric quantum chip used in my measurements. Type-IIa single crystal electronic grade diamond was implanted with 8 keV  $^{14}\text{N}^{4+}$  ions and annealed at  $900^\circ\text{C}$  to create ensembles of shallow NV centres (depth:  $12 \pm 4$  nm). The implantation fluence was varied to create in total five regions with different NV densities (from  $\sim 15 \mu\text{m}^{-2}$  to  $10^4 \mu\text{m}^{-2}$ ). The sample was equipped with coplanar Ti-Au electrodes with  $50 \mu\text{m}$  gap and mounted on a circuit board to enable microwave (MW) excitation and photocurrent readout. MW was provided using two printed antennas (183). Green laser illumination induces

the two-photon ionization of NV centres from the  $|0\rangle$  and  $|\pm 1\rangle$   ${}^3A_2$  NV ground state (GS) spin manifolds to the conduction band (CB) (Figure 48b) (177; 174). A DC electric field is applied in between electrodes and the photocurrent is read by lock-in after sensitive pre-amplification.

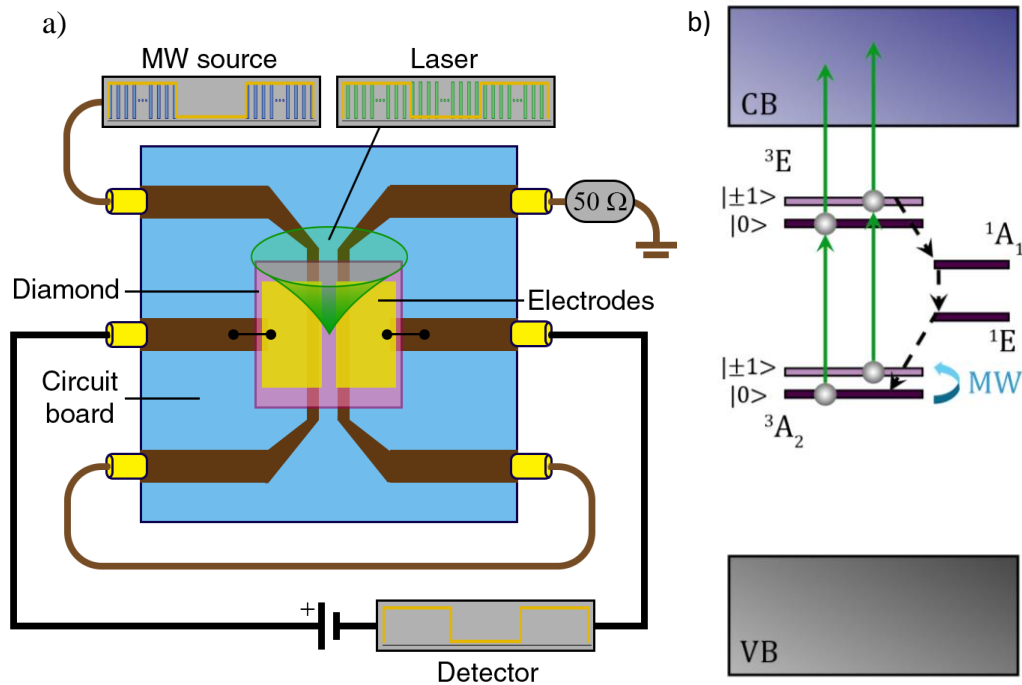


Figure 48: (a) The schematics of the setup used for pulsed PDMR showing a type-IIa nitrogen implanted diamond mounted on the circuit board. (b) A simplified electronic energy level scheme of the NV centre showing two-photon ionization of electron from GS to CB. Spin-selective decay through metastable  ${}^1E$  state enables the PDMR (MW: microwave, VB: valence band, CB conduction band).

#### 4.8.4. Results and discussions

The magnetic resonance (MR) contrast in the detected photocurrent is obtained under resonant microwave excitation (2.87 GHz) inducing transitions from the  $|0\rangle$  to the  $|\pm 1\rangle$  spin sublevels of NV ground state (65). Electrons photo-excited from the  $|\pm 1\rangle$  GS manifold have a non-zero probability to undergo shelving transitions from NV excited state to the metastable  ${}^1E$  state (99; 181). During the time in which the  $|\pm 1\rangle$  spin electron is stored in the metastable singlet state ( $\sim 220$  ns lifetime) (91; 182), it is protected from photo-ionization. This leads to a reduction of the overall photocurrent and thus to a minimum in the photocurrent signal at the resonant MW frequency (128). So far, the photocurrent signal from NV centres was readout either by lock-in technique referenced to the laser pulse frequency (128; 196) or by detecting the DC photocurrent after implementing a laser readout pulse (197). Both proposed methods suffer from a background photocurrent induced by the photo-ionization of other defects such as substitutional nitrogen ( $N_s^0$ ) (196), which reduces the detected MR contrast, preventing the

application of PDMR for single NV detection. Here I perform PDMR readout using pulse sequences and referencing the lock-in signal to the on-resonant MW pulses. By this way, I detect only the proportion of the photocurrent affected by the MW field, i.e. variations in the photocurrent signal  $S$ , related to  $|0\rangle \leftrightarrow |\pm 1\rangle$  transitions. Therefore I obtain a resonance spectrum with a positive contrast, defined as  $(S_{\max} - S_{\min}) / (S_{\max} + S_{\min})$ , where  $S$  is the AC signal detected by the lock-in and its maximum is equivalent to the  $\sim 30\%$  of the total DC off-resonant NV photocurrent. Because the AC off-resonant photocurrent is zero, the detection contrast between off- and on-resonant MW frequencies is  $\sim 100\%$  and is only reduced by the detected noise. As an additional advantage, the background signal from other defects than NV is filtered out when scanning the MW frequency around NV resonant line. By using the on-resonant trigger the signal from substitutional nitrogen is suppressed. Also, the use of MW triggering sequences gives significantly lower electronic noise that is identified to originate from coupling of MW irradiation to photocurrent readout circuits. To quantify the benefit of MW triggering scheme I measured CW PDMR spectra at the same position using both approaches (laser and MW pulse frequency referenced to lock-in amplifier with similar experimental conditions) and I compare the signal-to-noise ratios (S/N) for both cases in. The photocurrent signal  $S$  is determined from a fit of PDMR spectrum. The noise  $N$  is calculated as the standard deviation of the off-resonant (blank) photocurrent signal. The MW triggering yields on average a 7 times improvement in S/N ratio. At highly implanted region of the sample (corresponding to  $\sim 1000$  NVs in focus of the objective) I get a 7.4 times improvement in S/N for the MW-triggering method. The illustrative spectra are shown in Figure 49a. The vast improvement in S/N is visible even for a very fast measurement.

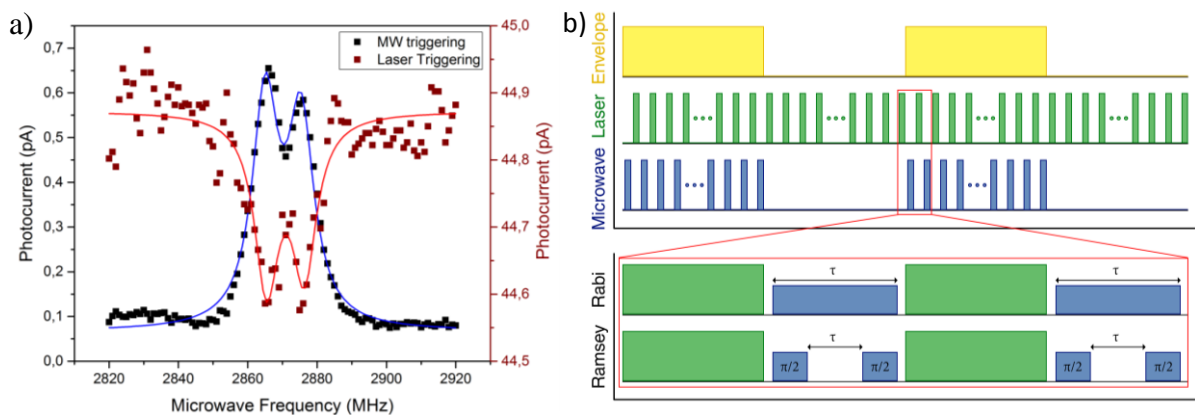


Figure 49: (a) Comparison of the laser (dark red dots) and MW (black dots) triggering CW PDMR method in the case of a fast measurement. Data were measured on a NV ensemble using similar experimental conditions and fitted. (b) PDMR pulse trains that encode high frequency pulse sequences (Rabi, Ramsey) into a low frequency envelope used as a reference for lock-in detection.

To achieve coherent manipulation of spins with photoelectric readout I encode single pulse sequences into a low-frequency envelope (Figure 49b). A continuous series of consecutive laser pulses is used, in which each pulse serves for the spin initialization and spin state readout. Bursts of spin manipulation MW pulses, time-shifted with respect to laser pulses, are added to encode any arbitrary sequence. A MW trigger pulse marks the start of the pulse burst during which the low frequency modulated photocurrent signal is measured. In the off period of the duty cycle, a train of spin polarisation laser pulses maintains the occupation of the  $|0\rangle$  state. I explored envelope frequencies from 30 Hz up to 1 kHz, tuned to obtain the highest S/N ratio. In principle, this method enables encoding any pulse sequence into the low-frequency envelope. Here I demonstrate this technique on Rabi and Ramsey protocols, which are essential for quantum measurements (2).

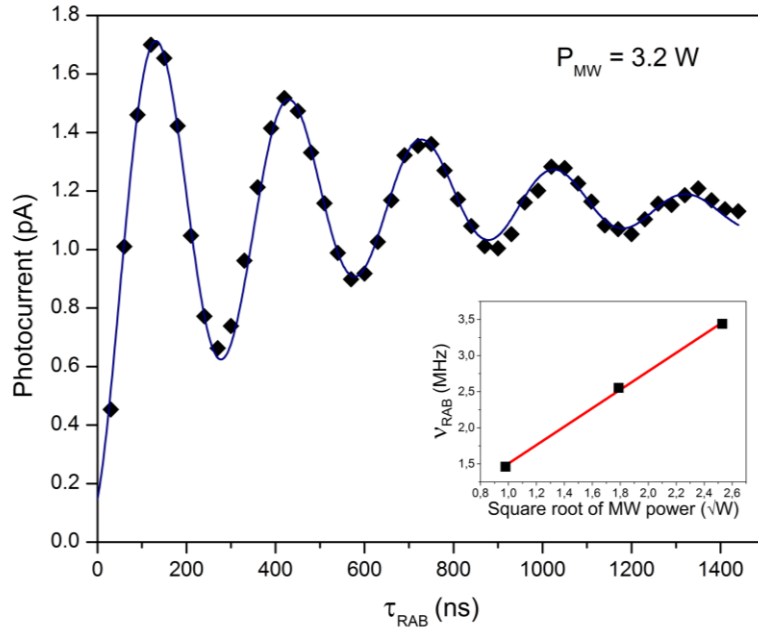


Figure 50: Photoelectric detection of Rabi oscillations using the envelope technique with MW-triggering. The black scatter points are the experimental data for MW power of 3.2 W and the blue line is fitted assuming an exponential damping. Inset shows the dependence of the frequency of Rabi oscillations with respect to the square root of the applied microwave power (red line is the result of linear fit).

Rabi measurements (see Figure 50) were performed first in the region of the sample with an approximate number of 1000 NV centres in the focus of the objective. Static magnetic field is applied perpendicularly to the  $\langle 100 \rangle$  diamond plane to split the  $|\pm 1\rangle$  spin levels. I then vary the duration of resonant MW pulses at constant power (see Figure 49b) to determine the duration of  $\pi$ -pulse. As expected, the Rabi frequencies calculated from the fit (179) of these measurements depend linearly on the square root of the MW power (Figure 50 inset). The

presented measurement proves the possibility of coherent spin readout using MW-triggered PDMR envelope pulse scheme. The measured Rabi oscillations for MW peak power of 3.2 W are plotted in Figure 50, yielding the Rabi decay time of  $\sim 490$  ns on the sample area with the highest  $^{14}\text{N}^{4+}$  ions implantation fluency.

To show the applicability of the designed PDMR protocols, I demonstrate functional Ramsey fringes pulse sequences (Figure 49b), employed to characterize the NV centre free spin dynamics. The measurement is performed at the same position as for the Rabi experiment. By varying the free precession time  $\tau_{\text{RAM}}$  I observe a decay curve consisting of the superposition of three cosine functions with different frequencies  $\delta_i$ . Each frequency corresponds to the detuning of the applied MW frequency from one of the hyperfine  $^{14}\text{N}$  transition such that  $\delta_1 = \nu_{\text{RAM}} - 2.2$  MHz,  $\delta_2 = \nu_{\text{RAM}}$  and  $\delta_3 = \nu_{\text{RAM}} + 2.2$  MHz (198; 199), where  $\nu_{\text{RAM}}$  is the Ramsey frequency. The measurement was performed for different detunings  $\delta_2$  (4, 8, 12, 16, 20 MHz) from the central resonant frequency. The results are shown in Figure 51. As expected I observe a linear dependency of the Ramsey frequency on the detuning values (Figure 51 inset).

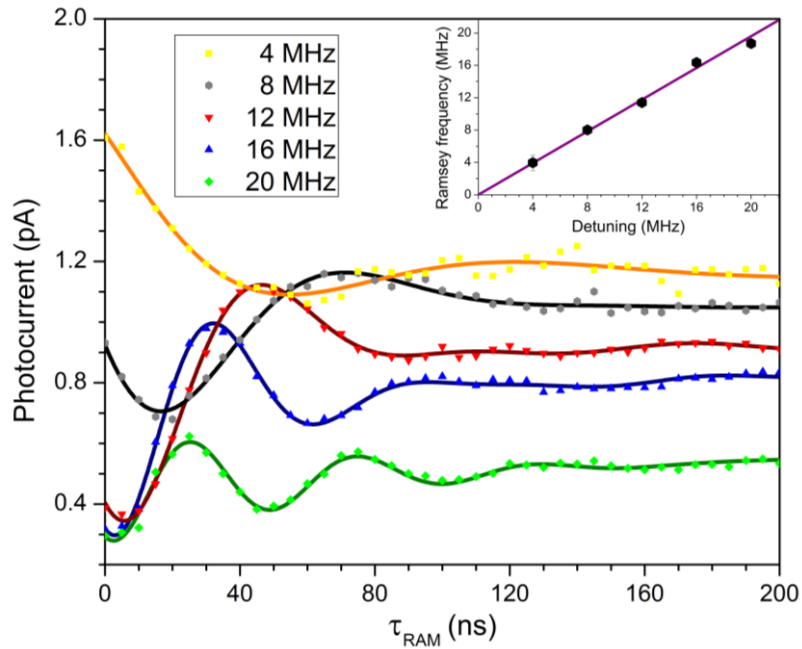


Figure 51: Photoelectric detection of Ramsey fringes for different detuning of MW excitation frequency from the NV resonant frequency. The scatter points are the experimental data, fitted considering a single exponential decay (continuous lines). Inset shows the linear dependence of Ramsey frequency to the MW detuning (purple line is the result of linear fit).

The average dephasing time  $T_2^*$  for all measurements is  $\sim 41$  ns using single exponential decay fitting (200) or  $\sim 66$  ns using Gaussian decay fitting of the data (201). This short value

reflects decoherent interactions of NV ensembles on the sample area over-implanted with  $^{14}\text{N}^{4+}$  ions. The main source of dephasing is the bath of paramagnetic substitutional nitrogen impurities ( $\text{N}_\text{S}^0$  centres) although  $^{14}\text{N}$  nuclear spins can also contribute (91; 55). Despite the very fast decay, this technique enables to readout Ramsey fringes at high frequency of 20 MHz with a very high contrast, confirming the ability of MW-referenced PDMR to measure samples with very short  $T_2^*$  times with high S/N ratio. By the proposed technique, Hahn-echo or more complex sequences such as CPMG (Carr-Purcell-Meiboom-Gill pulse train) can be encoded into the envelope carrier. The base value of the MW-triggered photocurrent is inversely proportional to the detuning frequency, reflecting the occupation of spin states integrated over the statistical weight of the  $|0\rangle$  and  $|-1\rangle$  manifolds.

An important milestone for the PDMR technique is to reach coherent manipulation of single NV spins. While our recent studies (128; 196) and other published work (197) demonstrated PDMR on NV ensembles, the photoelectric readout of single spins was not achieved yet. To downscale of the number of NV centres I used the N-implanted electronic grade diamond containing five regions of descending NV densities, corresponding to ensembles from 1000 to  $\sim 5$  NV centres in focus of the objective. The number of NV centres was calibrated from photoluminescence counts of a single NV obtained at the same conditions. First I measured the total photocurrent signal upon downscaling NV ensembles (see Figure 52 inset). For this I use lock-in technique referenced to a pulsed laser, without the MW field applied. This data could be fitted using a sublinear function. We speculate that this is due to a reduction of recombination lifetime in highly implanted region. From the fit we experimentally determine the total photocurrent resulting from the ionization of a single NV to be  $\sim 1.0$  pA for an electric field of  $2 \times 10^4 \text{ V} \cdot \text{cm}^{-1}$ , similarly to predictions presented in (128; 197). However, the measured photocurrent is a sum of NV-related photocurrent and of the background signal originating mainly from single substitutional nitrogen  $\text{N}_\text{S}^0$  ionization. We estimate that at these power conditions  $\sim 75\%$  of the signal comes from two-photon ionization of the NV centres (196). Thus I could experimentally verify the predictions of the photocurrent value expected for single NV centres in given electric field conditions by measurements on a small number of NV centres ( $\sim 5$ ), downscaled by at least  $\sim 10^4$  times compared to previous measurements (197).

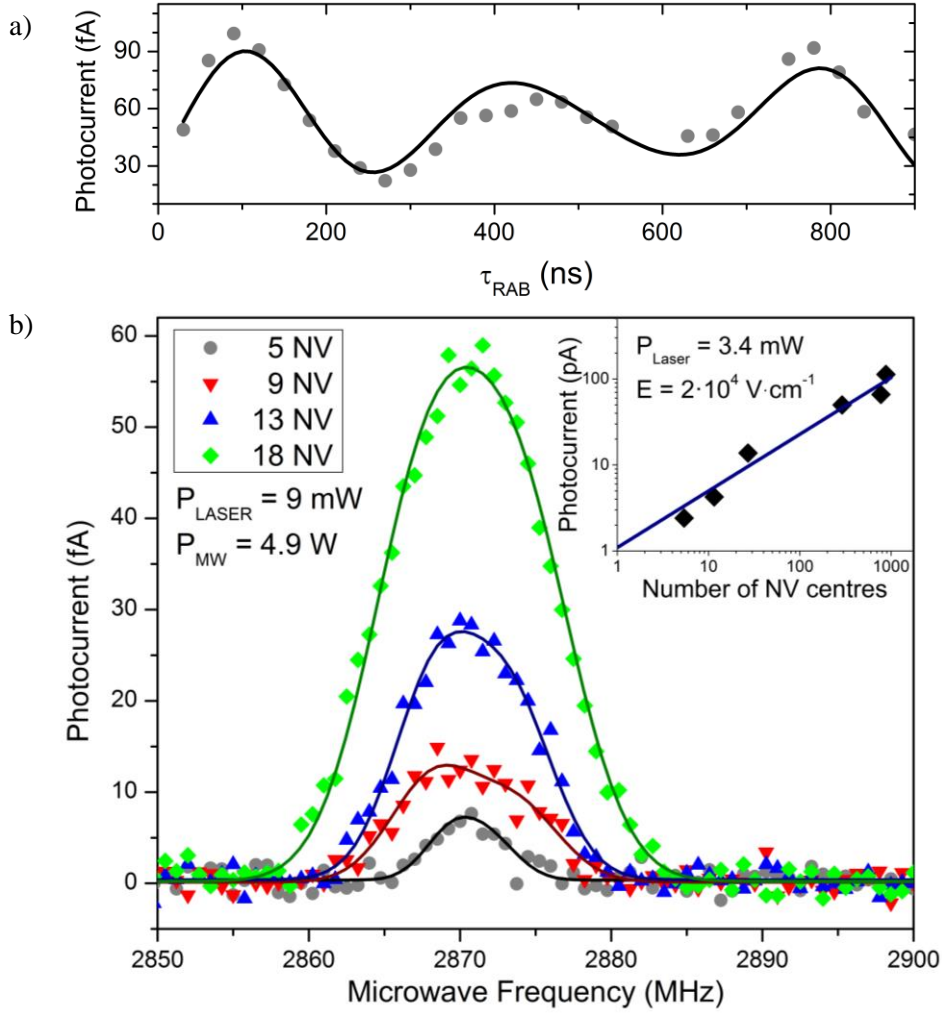


Figure 52: (a) Rabi measurement on 5 NV centres at MW power of 3 W. The fit of the data takes into account the beating originating from coupling to the nitrogen nuclear spins with frequency of 2.2 MHz, similarly to the fitting of Ramsey data in Figure 4. (b) Photocurrent spectra measured on small spin ensembles down to 5 NVs using a sequence consisting of short laser pulse followed by a MW  $\pi$ -pulse. The experimental data are fitted with two Gaussian functions. For comparison the inset shows the total photocurrent from different numbers of NV centres measured with only laser excitation (blue line is the result of fit).

By using pulse PDMR protocols with MW triggering, i.e. without any contribution of background photocurrent originating from  $N_s^0$  photoionization, I demonstrate Rabi measurement on the sample region with the lowest implantation density, e.g. with 5 NVs in the focus (Figure 52a). The presented results show the applicability of the scheme for measurements of just a very few individual NV centres. Figure 52b shows pulse PDMR spectra obtained for decreasing numbers of NV centres in the focus of the objective. Data were fitted using a two-peak Gaussian function (202), averaging over the central and hyperfine MR lines and a noise background offset was subtracted from the spectra. The estimated value for single NV photocurrent at resonance frequency averaged from all four measurements is  $\sim 2 \text{ fA}$ . This value is  $\sim 50$  times lower than the photocurrent expected for a single-NV in the used conditions

based on CW light-triggered measurements (see above) and considering a CW PDMR contrast of  $\sim 10\%$  (196). This is attributed to several factors such as the use of duty cycle (resulting in a reduced effective MW and laser power) and the loss of the contrast during the laser readout pulse (since the laser pulse is used for both readout and initialization of the NVs). However as shown in Figure 52a, the pulsed photocurrent related to the magnetic resonance of  $\sim 5$  NV centres is detected with very high contrast.

To explore the limitations of the pulsed PDMR method I concentrated on the comparison of theoretical and experimental values of noise level. The main components of the total noise  $N_{rms}$  come from the shot noise generated by the photocurrent  $I_{SN}(rms)$  (203), input noise of the pre-amplifier  $I_{Preamp}(rms)$  and input noise of the lock-in amplifier  $I_{Lock-in}(rms)$ , expressed as

$$N_{rms} = (\delta I_{SN}(rms) + \delta I_{Preamp}(rms) + \delta I_{Lock-in}(rms)) \sqrt{\Delta f}$$

where  $\Delta f$  is the bandwidth of detection electronics. Thanks to the lock-in amplifier detection, one is able to reduce the noise significantly, since in this case  $\Delta f$  corresponds to the equivalent noise bandwidth (ENBW) determined by the lock-in amplifier time constant. The ENBW can be then very narrow, thus increasing the S/N by rejecting the white noise (203). The total noise is then calculated as

$$N_{rms} = (\sqrt{e \cdot I} + \delta I_{Preamp}(rms) + \delta I_{Lock-in}(rms)) \cdot \sqrt{ENBW}$$

where  $e$  is the elementary charge and  $I$  is the measured photocurrent. Considering the specifications for our preamplifier and lock-in amplifier, I calculate for the CW technique  $N_{rms}/\sqrt{ENBW}$  of  $\sim 60.4 \text{ fA} \cdot \text{Hz}^{-1/2}$ , with a dominant noise originating from the preamplifier ( $\sim 60 \text{ fA} \cdot \text{Hz}^{-1/2}$  at given frequency), compared to measured value of  $\sim 83.7 \text{ fA} \cdot \text{Hz}^{-1/2}$  for 1000 NVs in the focus. I speculate that this difference ( $23.3 \text{ fA} \cdot \text{Hz}^{-1/2}$ ) between the experimental and predicted noise is due to photocurrent noise correlated to MW cross-talk occurring on the chip level. This type of cross-talk noise should be significantly reduced for the pulsed measurements where the laser readout pulse is decoupled from MW pulse. To confirm this I have determined the correlated noise for the experiment in Figure 52b, performed using the pulsed protocols. In this configuration the correlated noise is reduced to  $4.4 \text{ fA} \cdot \text{Hz}^{-1/2}$ . The correlated noise compared to the optically triggered CW PDMR ( $212.5 \text{ fA} \cdot \text{Hz}^{-1/2}$ ) is therefore reduced by a factor of 48. The shot noise for the MW-triggered PDMR is  $\sim 0.126 \text{ fA} \cdot \text{Hz}^{-1/2}$  calculated for a single NV spin photocurrent (considering a differential current between spin  $|0\rangle$  and  $|\pm 1\rangle$  states of 100 fA).

#### 4.8.5. Conclusion

To conclude, I demonstrate pulsed coherent readout techniques for small ensembles down to 5 individual NV centres in shallow implanted electronic grade diamond, which is the material used for relevant quantum applications. I developed MW referenced pulse sequences, enabling to eliminate the  $N_S^0$ -related background photocurrents, which was previously identified as a main obstacle for using PDMR technique for readout of single NV spins. By this way, together with lock-in readout technique, I reach the signal detection contrast close to 100%. A significant reduction of the correlated noise compared to CW technique made possible an order of magnitude enhancement of the S/N ratio. I developed hybrid Rabi and Ramsey photoelectric coherent spin manipulation protocols encoding high frequency MW and laser pulse sequences into a low frequency envelope. A further enhancement in S/N ratio can be achieved by designing nanoscopic electrodes for operating efficiently single NVs with high photoelectron gain (128; 196). The ability to read and control spin state by hybrid photocurrent method presented here demonstrates perspectives for progressing towards compact and scalable single spin device.

#### **Acknowledgements:**

Support from EU (FP7 project DIADEMS, grant No. 611143), Grant Agency of the Czech Republic (Project No. 16-16336S) and Czech-Flemish bilateral project BOF15BL08 are acknowledged. We would like to thank Professor Dmitry Budker from Johannes Gutenberg University, Mainz and from University of California, Berkeley for valuable discussions.

## 5. SUMMARY AND FUTURE PERSPECTIVES

Main aim of this work is development of detection methodology on the two, currently highly important, systems. One of them are probes based on nanodiamond particles (NDs) that can be utilized in in-vitro application and possibly in-vivo in near future. Here, I studied luminescence properties of the probes and developed novel detection techniques of the NDs in cell environment. The other systems are sensors based on single crystal diamond using novel photocurrent spin readout method in diamond, where I addressed the techniques towards the development of quantum chips. These chips have wide potential for application such as ultra-sensitive NMR detection or the sensors of ultra-small magnetic fields that could be applied in diagnostic methods i.e. magnetoencephalography or magnetocardiography. Such emerging medical diagnostic methods are starting to be used in large medical centers, however wider use is rather inconvenient thanks to the high price range. With the methodology presented in this work, it will be possible to substantially reduce pricing of such equipment and to provide compact devices with better spatial resolution, detection rates anticipated. For this purpose, techniques for realization, application and detection of NV based sensors have been studied on NV-containing single crystal diamond, for which we have developed novel and original principle of photoelectric detection. All of the goals has been fulfilled and are listed below:

- **Development of the optical setup for readout of NV specific signals**
  - I have rebuilt the home-built confocal setup, achieving imaging resolution of 300 nm and high sensitivity luminescence spectral scanning
- **Characterization of NDs for novel preparation methods**
  - I have measured and compared luminescent spectra of fluorescent NDs created by pellet and liquid target irradiation showing, that aqueous irradiation does not alter the NV luminescence properties of NDs
  - Using Raman spectroscopy I have demonstrated, that using liquid target yields lower lattice damage compared to pellet target irradiation
  - I have measured and analyzed luminescent spectra of fluorinated and oxidized fluorescent NDs demonstrating  $\approx 5\%$  increase in emission intensity of the NV<sup>-</sup> state upon fluorination
- **Detection of NDs in biological environment**
  - I have successfully internalized NDs in cancerous (MCF7) and dental pulp stem (DPSC) cells

- I have demonstrated novel way of how to detect near-IR probe (such as NV NDs) in cell environment with simultaneous visualization of non-fixed cell nucleus using Raman imaging without any additional dyes
- Using atomic force microscopy (AFM) in the force spectroscopy regime I have measured cell membrane Young's modulus variations upon NDs uptake demonstrating cell stiffening in time
- **Enhancing the detection rates for NV<sup>-</sup> spin state readout**
  - I have participated in the development of a completely new method for NV spin readout using photoelectric readout of magnetic resonances (denoted PDMR)
  - I have built the first PDMR setup and carried out the first photoelectric measurements
  - By varying the measurements parameters (triggering frequency, lock-in time constant, microwave and laser power, applied voltage, etc.) I have managed to suppress the noise and enhance the S/N ratio of PDMR.
  - I have studied and calculated the theoretical noise sources in PDMR measurements using lock-in detection and compared them with experimental results with prediction for the single NV shot noise
  - I have shown that by referencing lock-in detector to the microwave (MW) slow pulse frequency (~ 100 Hz) one can strip the PDMR signal from background photocurrents and measure thus with high S/N and contrast.
  - Using the MW referencing I have developed a method for coherent spin manipulation and readout with PDMR by encoding the high frequency (~ 20 MHz) pulse trains into the slow frequency (~ 100 Hz) envelope
  - Using the pulse sequences I was able to measure Rabi and Ramsey oscillations and downscale the detection from previous  $10^6$  to only 5 NVs in the focus.

### 5.1. Development of confocal setup

I have rebuilt the home-built confocal setup, achieving 300 nm resolution and high sensitivity spectral scanning of NV luminescence. Two additional detectors have been added to allow Time-Correlated Single Photon Counting (TCSPC) measurements. The whole system is now being enhanced to enable pulse Optically Detected Magnetic Resonance (ODMR) measurements. This will provide for magnetic sensing of NV centres either directly from ODMR resonance frequencies shift or by reading out the dynamic properties of the NV spins

such as  $T_1$  or  $T_2$  relaxation times. Such monitoring of temporary changes in magnetic environment is performed on a very short time scale and is of extreme interest for biomolecular sensing. This techniques will be further applied to ND sensors equipped with specific spin recognition chemical architectures.

## 5.2. Nanodiamond particles

The production of NV centres in Ib-type NDs has been optimized by altering the irradiation method (Stursa et al., Carbon, 2016, IF = 6.198). Use of aqueous suspension yields more homogeneous distribution of NV color centre per particles and brings possibility to achieve exactly one NV centre per ND. This is of interest for magnetic field sensing by the detection of electron spin resonance of  $NV^-$  color centre. I have contributed to this work by characterizing the produced nanoparticle. I measured and compared the luminescence of NDs create by both liquid and pellet target irradiation, to show that aqueous method does not change the  $NV^0/NV^-$  fluorescence ratio. Also, by measuring the Raman spectra and comparing the  $sp^2$  and  $sp^3$  carbon content of NDs I have found out, that aqueous irradiation causes less lattice damage than pellet irradiation.

Moreover, stabilization of NV luminescence for ND particles containing exactly one NV was demonstrated as the surface band bending induced by the covalent fluorination of the ND surface converts the NV to its bright state (Havlik et al., Advanced Functional Materials, 2016, IF = 11.38). This novel method is non-destructive (preserving the NDs morphology), provides with increased  $NV^-/NV^0$  ratio and creates colloidally stable nanoparticles. I have taken part in this work by studying the NV related luminescence. Using Raman spectroscopy I have analyzed the luminescence spectra of oxidized and variously fluorinated NDs and I have compared the  $NV^0/NV^-$  fluorescence ratio.

Furthermore, I have demonstrated successful internalization of ND in MCF7 and DPSC cell lines. To follow the NDs within the cells I have employed a Raman imaging technique (Gulka et al., in preparation for Journal of Biophotonics, IF = 3.82). Using a K-mean cluster analysis of obtained spectra (one per each pixel) it was possible to trace the NV luminescence and distinguish whether the signal is coming from already internalized or non-uptaken NDs. The simultaneously visualization of the nucleus of living cells was demonstrated, thanks to the Raman signal from cell, without the use of any additional dyes. This is a big advantage as this technique does not interfere with the cell (common methods includes staining or fixation of the cells).

To study the influence of ND uptake onto the cell membrane mechanical properties I have performed AFM measurement in force spectroscopy mode (Gulka et al., in progress. expected publication later in 2017). By analyzing the time-consequent force maps determination of the uptake rates with respect to the incubation time was possible with each cell analyzed individually. It was shown that ND uptake is responsible for mechanical changes of cell membrane stiffness as I observe cell hardening with time. The further plan is to consider the cell cycle in the measurements, as in a cell population, the dose of internalized nanoparticles in each cell varies as the expression of membrane proteins vary during the cell cycle. Thus the rate at which a cell takes up foreign material, as for instance nanoparticles, may depend on the cell phase, modifying accordingly their elasticity. The goal is to resolve how the state of the different cells affects the uptake of NDs by measuring the cell stiffness changes with the developed AFM spectroscopy method.

#### **Future perspectives:**

Recently, our collaborators have addressed an issue of ND particle aggregation in solvent reporting strategies for the modification of NDs, yielding bioorthogonally reactive hydrophilic shells (204) (205) (206). These hybrid particles show superior colloidal stability and they can be dissolved in aqueous buffers of high ionic strength and biological liquids. They are also protein-resistant: the polymer interface protects them against nonspecific protein adsorption. Moreover, the reactive groups on their surface enable highly efficient attachment of recognition/sensing moieties or complex molecular systems by various chemistries, including “click” chemistry. These features are crucial for the NDs function as selective chemo- or biosensors working in complicated matrices, including cytosol. The plan is to exploit these hydrophilic shells fabricating a new tool for highly sensitive, selective, and spatiotemporally resolved analysis of molecular events in biological environment. It will include construction of novel prototypes of nanosensors where optically detected magnetic resonance (ODMR) of the NV centre will be combined with sophisticated sensing architectures built on well-defined ND particles. Quantum sensing principles based on spin interactions of NV centre with smart molecular architectures at the sensors’ interfaces will be utilized. This will include three diverse approaches. Firstly, detection and quantification of free radicals via spin trap systems attached to NDs, secondly, selective molecular recognition of paramagnetic species (e.g. paramagnetic ions) followed by their direct spin-based quantification and finally use of cleavable spacers for rapid release of attached paramagnetic species from proximity of NV centre upon specific cleavage caused by an analyte.

### 5.3. Single crystal diamond

I have studied detection possibilities of NVs in the single crystal for the purpose of NV sensing application. Novel method for readout spin state of NV<sup>-</sup> centre has been developed by our team ([Bourgeois et al., Nature Communications, 2015, IF = 11.470](#)). The method is denoted PDMR and is based on photocurrent detection of charge carriers promoted to the conduction band of diamond by two-photon ionization of NV<sup>-</sup> centres. This novel technique is of great asset for magnetic sensing application as it overcomes limiting factors for optical detection such as low collection efficiency of photons and can be performed on an all-diamond devices. I have participated on the development of PDMR readout. I have built and designed the hardware of the PDMR setup and made first tests and measurements. I helped to test and adapt the controlling software and analyze the first photoelectric data. Together with E. Bourgeois we managed to measure for the first time magnetic resonance from NV centres using photoelectric readout.

Further, the dual-beam photoionization scheme was studied, where a blue laser is used for 1 photon ionization of NV centre and green laser is used for achieving the internal photo-transition leading to the spin contrast ([Bourgeois et al., Physical Review B, 2017, IF = 3.718](#)). This technique was a first step to suppress N<sub>S</sub><sup>0</sup>-related photocurrent and to control photoionization rate and magnetic resonance (MR) contrast independently. I have contributed to this study by a thorough analysis of the MW resonance signal strength dependency on the PDMR parameters (including triggering frequency, lock-in time constant, microwave and laser power, applied voltage, detection frequency filters, sensitivity of the pre-amplification etc.). The results enabled to detect PDMR with higher signal-to-noise ratio reducing thus the measurement times.

Using PDMR for quantum sensing applications - and in particular to read and image nearby target spins - requires coherent pulsed spin manipulation and photoelectric readout of a single NV centre. During my last years of PhD study I have developed such specific pulsed protocols for PDMR detection ([Gulka et al., Physical Review Applied, accepted, IF = 4.061](#)). By using lock-in amplifier I could lock on the  $m_s = 0 \leftrightarrow m_s = \pm 1$  spin transition and therefore strip any background photocurrent related to ionization of N<sub>S</sub><sup>0</sup> (or other) defects, leading to high contrast and S/N ratio. The photoelectric detection of Rabi and Ramsey sequences was demonstrated on ensembles from 1000 to just 5 NV spins even on a sample with very short T<sub>2</sub><sup>\*</sup> time (~ 41 ns), proving high sensitivity of the method anticipated to reach single spin detection. These results open up a pathway towards the realisation of scalable photoelectric quantum chips.

### **Future perspectives:**

One particularly interesting application of PDMR is a development of electrically-readout quantum spin sensors with optimized performances, enabling highly sensitive, selective, and spatio-temporally resolved NMR quantum analysis of magnetic fields originating from molecular objects. These non-perturbing and non-invasive quantum spin probes acting as a nanoscale magnetic resonance imaging system will allow determination of single molecule structure without the need of averaging, which is one of the most prominent ambition of today's nano-characterization techniques. The enhanced S/N ratio enabled by PDMR will lead to a major improvement of sensitivity and acquisition time, which is the key element for spin-probe applications as single molecular matrix imagers. For example in a theoretical 3D nano-MRI (magnetic resonance imaging) proposal, the total acquisition time to image the  $^1\text{H}$  structure of rapamycin using optical readout of a single NV centre is more than 7 days (and twice as long for the  $^{13}\text{C}$  structure) (8). Our first measurements show that the detection rates of PDMR ( $\sim 10^7$  electrons. $\text{s}^{-1}$  per NV and higher) provide a vast rate enhancement of almost 3 orders of magnitude compared to confocal ODMR ( $2 \cdot 10^4$  photons. $\text{s}^{-1}$  per NV at same conditions and laser power of 3.4 mW) (196). Taking into account the current PDMR detection rates, the time required for imaging of the rapamycin molecule would be already reduced to tens of minutes.

## 6. OUTLOOK FOR THE BIOMEDICAL ENGINEERING

As a stable-spin qubit with long coherence time and photoluminescence detection, nitrogen-vacancy (NV) centre in diamond has been demonstrated as a unique room-temperature sensor. Many of NV-sensing utilizations outreach into biomedical engineering including clinical and theranostic applications. This chapter summarizes the related biomedical application of nanodiamonds (NDs) and single crystal diamond (SCD) and discusses how the novelty of this thesis contributes to the current state-of-art methods and research.

### **A) BIOMEDICAL APPLICATIONS OF NANODIAMONDS:**

Vast majority of the ND biomedical applications involves direct in-vitro cellular application with in-vivo applications anticipated in near future. The considerable interest in NDs' use for theranostic applications has raised concerns about the biocompatibility and nontoxicity of diamond particles. Bulk diamond is known for its excellent biocompatibility and nontoxicity, mainly due to the  $sp^3$  carbon, that makes diamond material chemically and biologically inert (10). At nanoscale, one has to consider increased surface-to-volume ratio (9) and therefore higher chemical surface reactivity (14), so understanding the nature of nanodiamond interactions with surrounding biological structures is critical (207). Several factors need to be taken into account when examining ND biocompatibility: particle size, ND concentration, exposure time, surface chemistry and cell-type-specific response (9). The long-term stability (5 months) and nontoxicity has been demonstrated even on a large concentration (up to 75 mg/kg of body weight) on rat studies using standard-sized ( $\sim 100$  nm) HPHT NDs (208). Even though NDs are so far considered well biocompatible and nontoxic for cultured cells (209; 210) and animals (211; 208), further studies are necessary to examine long-term organ exposure outcomes [for possible "nanotoxicity" induced by the nanoscopic size (212)] and duration needed for complete clearance (207). Apart from biocompatibility, another important NDs' feature is near-IR luminescence that has small absorption in tissues and is easily spectrally distinguishable (with longer wavelengths than cell's auto-fluorescence) and thus can be conveniently separated with the optical long-pass or bandpass filter. Lifetime of the detected fluorescence can be also used to identify NVs as the bio-luminescence happens on substantially shorter timescale [1–4 ns (213)] than NV luminescence [ $\sim 11$  ns (214)].

### Nanodiamond-mediated drug and gene delivery:

Up-to-date NDs' applications in living biological systems focus mainly on **drug delivery** (212). Large number of therapeutically important drugs have poor water solubility and their clinical applications are thus limited (215). One of the approaches to circumvent this issue is to complex poorly water-soluble drugs with nanoparticles (216) to enhance their dispersion while keeping the drug activity. To be considered as a drug delivery platform of this kind, the NDs must be biocompatible, able to carry a broad range of therapeutics and must have good water dispersibility. Diamond nanoparticles fit all these requirements and, furthermore, their fluorescence can be used to detect the NDs and to monitor the drug release. The detachment of the carried molecule can be observed optically by detecting the luminescence spectral change as the charge molecules on the NDs' surface alter the charge state of NV centres (5). This principle is visualized in Figure 53.

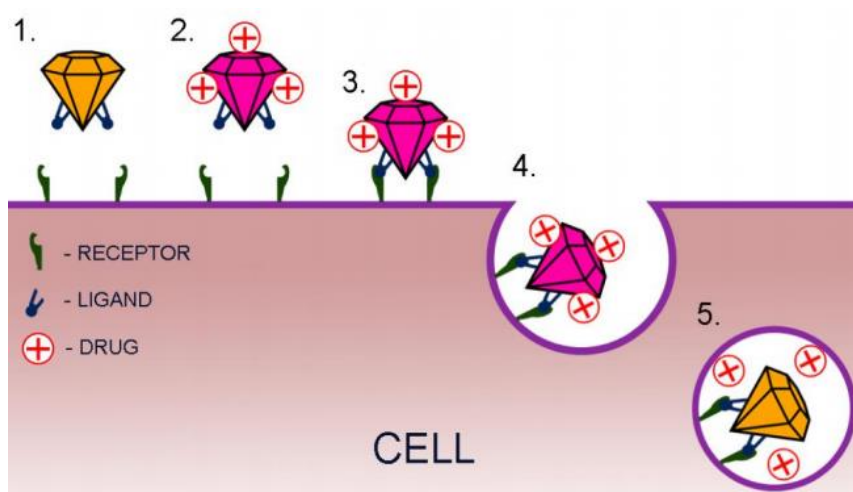


Figure 53: Principle of nanodiamond-mediated delivery of therapeutics with direct optical monitoring of drug release. The charge of the ligands/drugs attached to the NDs' surface shifts the  $NV^-/NV^0$  ratio which leads to the colour change of the detected luminescence.

First attempts at ND-drug delivery systems were prepared mainly by absorption of lipophilic drug molecules onto the surface of small (4-6 nm) detonation NDs and creating cluster (see Figure 54) of 100-200 nm size (217). The aggregates result in enhanced blood circulation half-time and tumour retention and different anticancer drugs have been delivered using this approach (212). However, obtaining a narrow size distribution of these clusters with high stability is challenging and thus there is a potential risk for non-specific interactions with plasma proteins and unpredictable side effects (218). Later, stabilization of single ND particles has been demonstrated by attaching polymers on ND surface (219) and drug molecules have

been conjugated to this platform (220; 221). Further, polymer shells were introduced (204) that significantly increased the colloidal stability of such modified NDs and offered enhancement especially for delivery of highly hydrophilic drugs (212). Vast range of different cargos have been delivered to cells by NDs including cancer treating drugs [sorafenib (222), doxorubicin (223), daunorubicin (224), cisplatin (225), paclitaxel (226)], proteins (227; 228), small molecules under acidic conditions (228), siRNA for specific cancers (229) and nucleic acids (see further). NDs were also used as a composite with gutta-percha for root canal (endodontic) therapy (230) or conjugated with alendronate to achieve bone-targeted delivery for osteoporosis treatment (231).

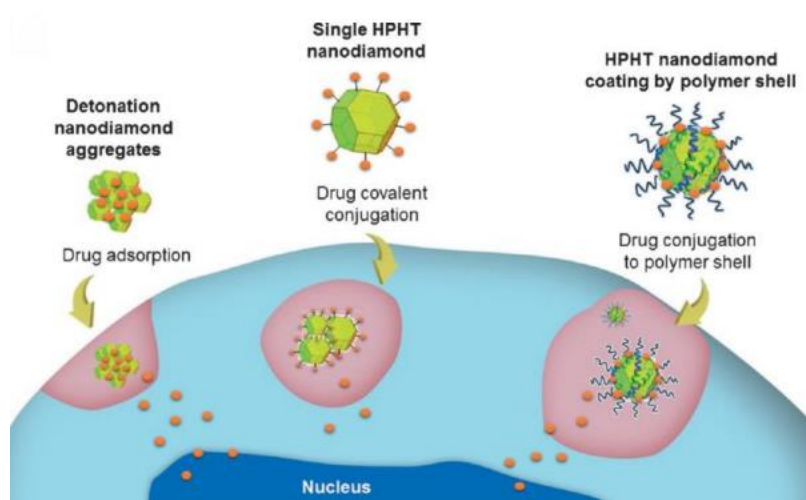


Figure 54: Different drug delivery systems based on nanodiamond particles. Taken from (212).

The fact that NDs are capable of safely and efficiently introduce DNA coding to the cells in a culture makes them a good candidate for **gene therapy** applications. Moreover, they can be used as a cell targeting bifunctional device: a DNA-delivery vehicle and a fluorescent label at the same time. The gene therapy is problematic owing to the facts, that naked nucleic acids have inefficient cellular delivery due to the physicochemical characteristics (i.e. negative surface charge, large molecular weight) (232) and that there is a deficiency in acceptable vector delivery systems (233). Diamond nanoparticles have found a role in gene transfection because of their superior properties. The DNA delivery has been demonstrated using fenton-treated hydroxylated NDs functionalized with triethylammonium to pair electrostatically with negatively charge plasmid DNA (234). Other approaches employ PEI functionalization of NDs and then apply them to DNA delivery (235) and direct monitoring of cargo release (6).

### **Nanodiamonds as markers for bioimaging:**

The excellent photostability of NV defects provides a great advantage over commonly used fluorophores (236) and makes the NDs one of the most promising candidates for long-term biomedical imaging/labelling both in vitro and in vivo (237). **Cellular imaging** with NDs can provide critical information on cellular function, movement, and development and can assist in diagnosis and treatment of diseases. To date, NDs have been successfully internalized in various cell lines with possibility of reconstructed three-dimensional imaging and accurate particle tracking (238) recently demonstrated in real time (239) (3). NDs have been used as a luminescence probe e.g. to investigate the uptake mechanism of transferrin in HeLa cells (240), to monitor the intracellular transport of proteins through tunneling membrane nanotubes (241) or to help understand the transforming-growth-factor-beta receptors and their pathways (242). NDs can be also used for **organism imaging** to study the functionality and characteristic of entire system. Fluorescent NDs, for example, were employed to investigate the entire digestive system tract of *Caenorhabditis elegans* (211). Furthermore, potential for long-term imaging (up to 28 days) was demonstrated after an intravenous injection of NDs into mice to study NDs' fate and biodistribution (243). Alternative imaging techniques of NDs make use of the **ODMR signal** from NV centres. Nanodiamond imaging (in 3D) was demonstrated for example by scanning the magnetic field free-point while the central resonant microwave (MW) frequency and light illumination was applied to the whole sample (see Figure 55a) (244). Here, the optical excitation shifts the NV spins into a highly fluorescent state, and the MW affects only spins near the field-free point resulting in the decrease of fluorescent signal. The phantom with NDs was placed in the chicken breast and imaged. Sensitivity and spatial resolution was calculated from the results and it was suggested that this method has the potential to yield images with high sensitivity ( $\sim 100$  fg nanodiamond) together with high spatial resolution ( $\sim 100$   $\mu\text{m}$ ), which are mutually exclusive in existing imaging systems (see Figure 55b).

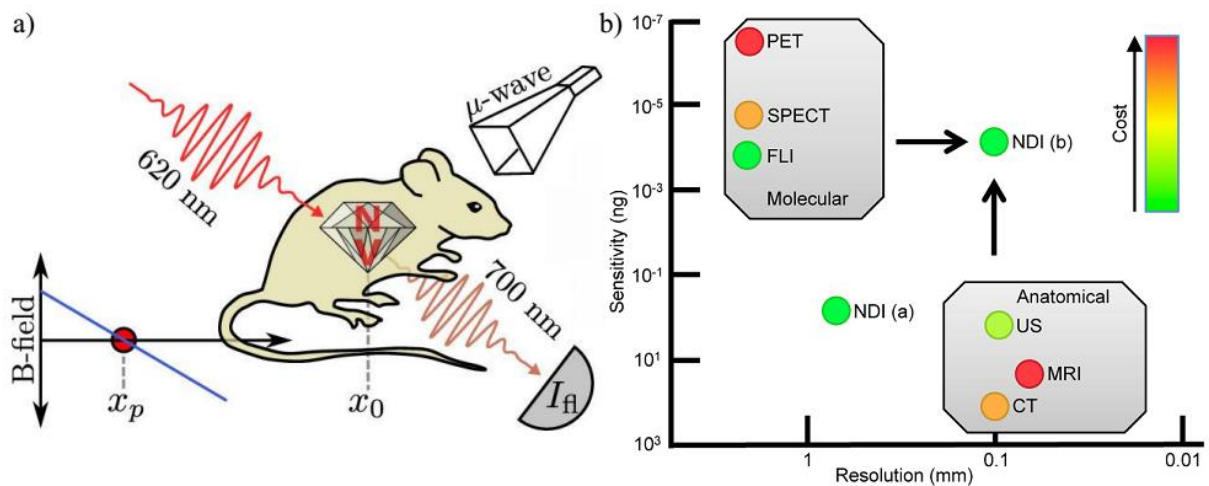


Figure 55: Nanodiamond imaging using ODMR principle. (a) Schematics of the measurement. The whole sample is illuminated and excited with microwave ( $\mu$ -wave) and the NV luminescence is detected. To create the image, magnetic field free-point is scanned. (b) Comparison of sensitivity and the resolution with the commonly used methods [NDI (b) – results of nanodiamond imaging, NDI (a) – future implementation of nanodiamond imaging, FLI – fluorescence imaging, US - ultrasound]. Taken and modified from (244).

### Quantum sensing in cells:

Apart from nanodiamond imaging, ODMR signal from NV centres can be employed for **quantum sensing**. Measurements of magnetic fields and other physical quantities with high sensitivity (55) and nanoscale spatial resolution (85) are possible as the fluorescence signal intensity is modulated upon interactions of the NV's single electron spin with the surroundings. Even though this field is just arising, several successful examples prove the great potential of NDs to be developed into the smallest sensing probes for nanoscale detection of ultra-small magnetic fields and electron spins in vitro and eventually in vivo (212).

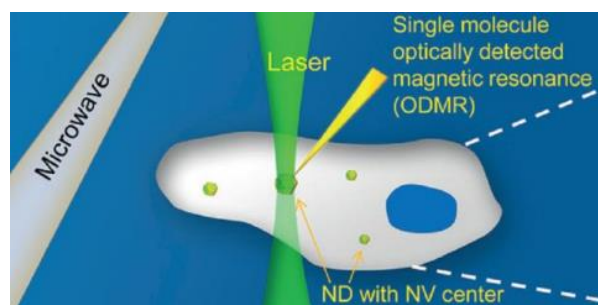


Figure 56: Illustration of ND quantum sensing experimental setup for detection inside living cells. Taken from (212).

The possibility to study the biological reactions inside living cells by quantum sensing with NDs has been confirmed in (245), where ODMR from single ND was detected inside HeLa cells. Thanks to the unique ODMR spectrum of a ND with single NV centre it was possible to

identify and track the particles inside the cells. The common experimental setup for ODMR quantum sensing with nanodiamonds is depicted in Figure 56. One of the fascinating utilization of quantum sensing is **nanoscale thermometry**. The measurement is based on the temperature dependence of the zero-field splitting as the precise value of the MW transition frequency changes. The ability to monitor local temperature variations has been demonstrated in a living human embryonic fibroblast (246), with measurement precision as small as 1.8 mK and a spatial resolution as small as 200 nm. Other applications include **monitoring of ion concentrations** with use of spin relaxometry (247), **optical trapping** of NDs with concurrent ODMR measurement for maneuvering the ND inside the cellular environment with nanometer precision (107) or **measurement of membrane potentials** based on electric field detection (107). Sketches for the quantum sensing application are shown in Figure 57.

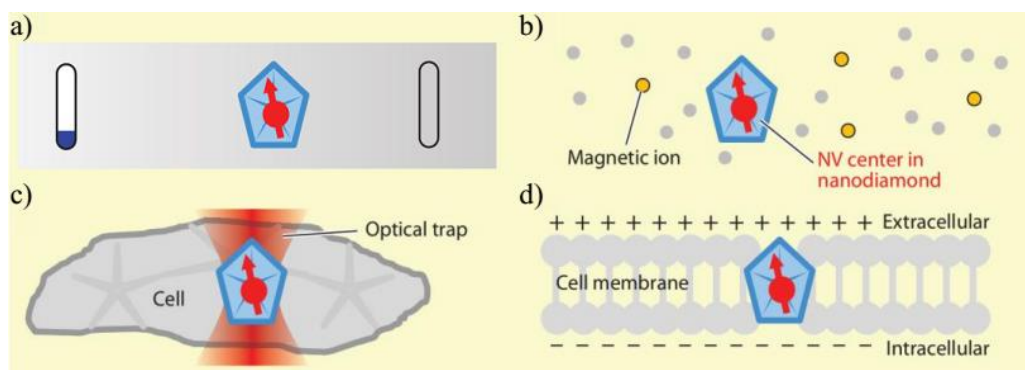


Figure 57: Promising applications of NDs with NV centres for quantum sensing including (a) nanoscale thermometry, (b) monitoring of ion concentrations, (c) optical trapping and (d) measurement of membrane potentials. Taken from (107).

### **Novelty and contribution of the thesis' results with respect to the state-of-art:**

The applications of NDs presented here make use of NV fluorescence either for imaging or sensing. For this, bright particles are necessary. Each NV centre has a comparable brightness to a single dye molecule of a conventional fluorophore (108) but, if the number of optically active NV centres per particle increases, the total photoluminescence increases as well. For quantum sensing, magnetometry and orientation tracking of ND only one NV centre per particle is desirable (248). This thesis described a novel method of ND preparation by liquid target irradiation that yields a three-fold larger fraction of luminescent NDs which is important for all above application. Another boosting of luminescence has been demonstrated by a new fluorination method of NDs that not only increases the number of optically active NVs but also creates well soluble particles, which is essential for cellular experiments. Both of these methods (liquid target irradiation and fluorination) also contribute to production of NDs containing

exactly one NV centre. Other two results presented on NDs (Raman imaging on NDs with respect to nucleus and AFM cell membrane stiffness measurement upon ND uptake) contribute further to understanding the processes responsible for ND uptake and the NDs cellular fate. Raman imaging method also provides a way to visualize cell nucleus without the need of any label or cell fixation so it enables to study cell-ND interactions without additional cell perturbing.

## **B) BIOMEDICAL APPLICATIONS OF SINGLE CRYSTAL DIAMOND:**

The fact that the NV spin quantum states can be influenced even by ultra-weak external electric or magnetic fields gives rise to one of the most visionary application of NV sensors: the detection and three-dimensional mapping of nuclear spins in nanoscale samples with atomic resolution (**nano-MRI**). The quantum detection and metrology are anticipated to bring a ground-breaking understanding of life cycle processes, including applications to medicine. These techniques move towards a direct monitoring and imaging of single molecular objects or even resolving their atomic structure by using quantum protocols without need of averaging over ensembles (8). Unfortunately most of the quantum sensors, such as ensembles of cold atoms, or SQUIDS require specific working conditions such as cryogenic temperatures or ultra-high vacuum and have limited spatial resolution (75).

Recently, it has been shown that for NV ensembles magnetic sensitivity can be as low as  $\sim 100 \text{ fT}\sqrt{\text{Hz}}$  with predicted quantum limit  $\sim 0.9 \text{ fT}\sqrt{\text{Hz}}$  (2), thus practically approaching the sensitivity of SQUIDS and cold atom ensembles ( $\sim \text{fT}\sqrt{\text{Hz}}$ ). Using a single NV centre qubit spatial resolution of single molecule can be reached and, moreover, NV operates at room temperature. Some first works have demonstrated single NV qubit sensor as a quantum spin-probe for detection of external single electron spin (92), nuclear spins (75) or even 3D nano-MRI (8). By using the NMR-based protocols, the resulting information can be worked out either classically or by quantum way using quantum tomography techniques, approaching super-resolution (8). The main principle of such methods is detection of weak magnetic fields originating from the targeted spins by appropriate manipulation of the spins to affect the precession phase accumulation of the highly coherent NV electronic spin. For instance, electron spin external to diamond can be detected using double electron–electron resonance (DEER), where spin echo MW sequence ( $\pi/2, \pi, \pi/2$ ) is applied to NV centre and a RF pulse tuned to NV  $\pi$ -pulse is scanned to flip the probed spin, therefore the spins dipolar magnetic field is reversed and the equivalence of the NV spin precession is disturbed. Using similar scheme a

single proton NMR (both time-domain and spectroscopic) can be detected sensing nanotesla field fluctuations at room temperature (75).

This is a significant application of the NV sensor since the conventional coil-based induction method is insensitive to samples at nanometer scale, as their sensitivity is limited only to large spin ensembles (212). In a conventional MRI machine, large magnets are used to set up a field gradient in all three directions and thus to enable creation of 3D images. With NV-based nano-MRI, natural magnetic properties of the single NV centre qubit (which is a magnetic dipole) can be employed for this purpose (8) (see Figure 58a). The nano-MRI technique would bring a possibility to look inside the proteins and learn how they interact with chemicals, such as newly developed drug molecules, and provide thus an important new tool for drug discovery. Because the method is non-invasive, it could be theoretically used to image the interior of living cells or to detect metal ions in cells (249).

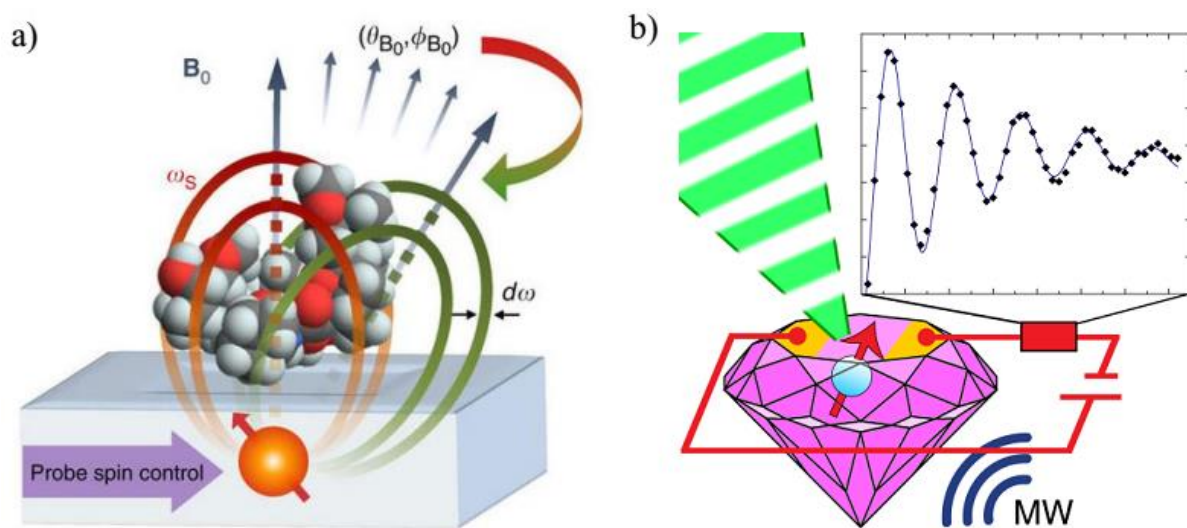


Figure 58: (a) Implementation of a single NV qubit for a nano-MRI application using ODMR. The probe acts as both sensor and gradient field source for the spatial-frequency encoding of the nuclear spins in the target molecule. Taken from (8). (b) The proposed novel detection principle implementing the PDMR scheme to coherently read out the NV spin state.

### Contribution to the state of art – PDMR sensor:

Current quantum methods rely on using optical readout of single NV, leading to voxel volume of approximately  $5 \text{ nm}^3$  (93) and to long acquisition time averaging over many measurements (in the best case 1 photon over 10-50  $\mu\text{s}$  range is detected by ODMR). The novel method Photoelectric Detection of Magnetic Resonance (PDMR) in diamond that was developed as a part of this thesis can significantly shift the potential of NV centre for single molecular detection due to the high detection rate. This proposed readout method (see Figure

58b) is essential to the developed imaging technique as it will improve the sensitivity of the detection by a factor  $10^3$  or higher (196). Therefore, it would enable single shot readout of the developed probe spin and thus access dynamically the changes in i.e. biological or chemical environment with high signal-to-noise (S/N) ratio. Also, overcoming of the diffraction limit imposed by the optics is feasible by construction of nanoscale pixels and or even full matrix of such pixels to develop quantum detector with high spatial resolution. Establishing single NV readout with enhanced S/N ratio enabled by PDMR will lead to a major improvement of sensitivity and acquisition time, which is the key element for spin-probe applications as single molecular matrix imagers. For example the theoretical total acquisition time to image the  $^1\text{H}$  structure of rapamycin using 3D nano-MRI optical readout of a single NV centre is more than 7 days (8). Taking into account the detection rate enhancement of almost 3 orders of magnitude, the time required for imaging of the rapamycin molecule would be already reduced to tens of minutes with PDMR.

## 7. LIST OF AUTHOR'S PUBLICATIONS AND SELECTED PRESENTATIONS

### 7.1. Publications

- [1] **M. Gulka**, M. Martin, B. Varga, T. Cloitre, P. Cigler, M. Nesladek, C. Gergely, *AFM study of diamond particles internalization by monitoring the cell membrane stiffness changes*, in progress
- [2] **M. Gulka**, H. Salehi, B. Varga, T. Cloitre, F. J. G. Cuisinier, P. Cigler, M. Nesladek, C. Gergely, *Label free visualization of near-IR probes in cells using Raman imaging*, Journal of Biophotonics, in preparation, **IF = 3.82**
- [3] M. Krecmarova, E. Bourgeois, J. Hruby, **M. Gulka**, Ch. Freiwald, T. Vandenryt, R. Thoelen, V. Mortet, M. Nesladek, *Manipulation of NV center charge state on highly boron doped diamond electrode for biosensing applications*, Material Research Letters, in preparation, **IF = 5.89**
- [4] **M. Gulka**, E. Bourgeois, J. Hruby, P. Siyushev, G. Wachter, F. Aumayr, P. R. Hemmer, A. Gali, F. Jelezko, M. Trupke, M. Nesladek, *Pulsed photoelectric coherent manipulation and detection of NV centre spins in diamond*, Physical Review Applied (accepted), 2017, **IF = 4.061**
- [5] E. Bourgeois, E. Londero, K. Buczak, J. Hruby, **M. Gulka**, Y. Balasubramaniam, G. Wachter, J. Stursa, K. Dobes, F. Aumayr, M. Trupke, A. Gali, and M. Nesladek, *Enhanced photoelectric detection of NV magnetic resonances in diamond under dual-beam excitation*, Physical Review B (Rapid Communications), 2017, **IF = 3.718**
- [6] J. Havlik, H. Raabova, **M. Gulka**, V. Petrakova, M. Krecmarova, V. Masek, P. Lousa, J. Stursa, H.-G. Boyen, M. Nesladek, P. Cigler, *Benchmark Fluorination of Fluorescent Nanodiamonds on a Preparative Scale: Toward Unusually Hydrophilic Bright Particles*, Advanced Functional Materials, 2016, **IF = 11.38**

- [7] J. Stursa, J Havlik, V. Petrakova, **M. Gulka**, J. Ralis, V. Zach, Z. Pulec, V. Stepan, S. A. Zargaleh, M. Ledvina, M. Nesladek, F. Treussart, P. Cigler, *Mass production of fluorescent nanodiamonds with a narrow emission intensity distribution*, Carbon, 2016, **IF = 6.198**
- [8] E. Bourgeois, A. Jarmola, P. Siyushev, **M. Gulka**, J. Hruby, F. Jelezko, D. Budker, M. Nesladek, *Photoelectrical detection of electron spin resonance of nitrogen-vacancy centres in diamond*, Nature Communications, 2015, **IF = 11.470**
- [9] J. Havlik, V. Petrakova, I. Rehor, V. Petrak, **M. Gulka**, J. Stursa, J. Kucka, J. Ralis, T. Rendler, S-Y. Lee, R. Reuter, J. Wrachtrup, M. Ledvina, M. Nesladek, P. Cigler, *Boosting nanodiamond fluorescence: towards development of brighter probes*, Nanoscale, 2013, **IF = 6.739**
- [10] **M. Gulka**, V. Petrakova, A. Taylor, L. Fekete, F. Fendrych, P. Cigler, M. Ledvina, J. Stursa, M. Nesladek, *Luminescence properties of nitrogen-vacancy centres in nanodiamond as a function of size*, Instruments and Methods for Biology and Medicine, 2012

## 7.2. First-author presentations

### Oral presentations at international scientific conferences:

- [1] **M. Gulka**, E. Bourgeois, J. Hruby, M. Trupke, M. Nesladek, *Pulsed photoelectric coherent manipulation and detection of NV center spins in diamond*, Hasselt Diamond Workshop 2017, SBDD XXII, Mar 8 - 10, Hasselt, Belgium
- [2] **M. Gulka**, M. Nesladek, *Fluorescent diamond probes: charge sensing and intracellular delivery*, SPIE: Photonics West 2017, OPTO, Jan 31 – Feb 2, San Francisco, California

- **Invited paper**

- [3] **M. Gulka**, E. Bourgeois, J. Hruby, M. Trupke, M. Nesladek, *Magnetometry based on photoelectric readout of electron spin resonance of NV centres in diamond*, E-MRS 2016, Fall Meeting, Sep 19 - 22, Warsaw, Poland  
- Obtained “**The Best Student Presentation Award**” in symposium A: Atomic and molecular scale systems and devices

**Other oral presentations:**

- [1] **M. Gulka**, *Magnetic sensing using NV centres in diamond*, Nanoscale Diagnostic Methods in Biology and Medicine 2015, student conference, Kutná Hora
- [2] **M. Gulka**, *Diamond nano-probes*, Nanoscale Diagnostic Methods in Biology and Medicine 2014, student conference, Poděbrady
- [3] **M. Gulka**, *Diamond nano-probes – How to read their signals*, Diplomky na stojáka, 2013, student competition, Prague  
- Obtained **audience award** for best presentation.
- [4] **M. Gulka**, V. Petráková, A. Taylor, L. Fekete, F. Fendrych, P. Cígler, M. Ledvina, J. Štursa and M. Nesládek. *Luminescence properties of nitrogen-vacancy centres in nanodiamond as a function of size*, Instruments and Methods for Biology and Medicine 2012, FBME CTU, Prague  
- Obtained award for **best presentation**

**Poster presentations at international scientific conferences:**

- [1] **M. Gulka**, E. Bourgeois, J. Hruby, M. Trupke, M. Nesladek, *Photoelectric Nitrogen-Vacancy Electron Spin Magnetometry*, MRS Spring Meeting & Exhibit 2017, Apr 17 – 21, Phoenix, Arizona
- [2] **M. Gulka**, M. Martin, H. Salehi, B. Varga, T. Cloitre, F. J. G. Cuisinier, P. Cígler, M. Nesládek, C. Gergely, *Study of diamond particles internalization by monitoring cell membrane stiffness changes and their luminescent signal*, Hasselt Diamond Workshop 2016, SBDD XXI, Mar 9 - 11, Hasselt, Belgium

- [3] **M. Gulka**, M. Martin, H. Salehi, E. Middendorp, T. Cloitre, F. J. G. Cuisinier, M. Nesládek, C. Gergely, *Tailored internalization process of peptide coated luminescent nanodiamond particles in various cell lines*, SLAS 5<sup>th</sup> Annual Conference and Exhibition 2016, Jan 23 – 27, San Diego, California  
- Obtained “**Tony B. Academic Travel Award**” for the high quality abstract
- [4] **M. Gulka**, V. Petránková, V. Petrák, A. Taylor, L. Fekete, P. Cígler, M. Ledvina, J. Štursa, M. Nesládek. *Stabilization of nitrogen-vacancy centres in nanodiamond by fluorine surface termination*, MRS Spring Meeting & Exhibit 2015, Apr 6 – 10, San Francisco, California
- [5] **M. Gulka**, J. Hrubý, V. Petránková, Z. Remeš and M. Nesládek. *Nitrogen-vacancy centers in nanodiamond for cellular sensing*, International Microscopy Congress 2014, Feb 7 - 12, Prague, Czech Republic
- [6] **M. Gulka**, V. Petránková, V. Petrák, A. Taylor, L. Fekete, P. Cígler, M. Ledvina, J. Šturza and M. Nesládek. *Changes in nanodiamond particles luminescence due to the size effects and surface interactions*, Hasselt Diamond Workshop 2013, SBDD XVIII, Feb 27 – Mar 1, Hasselt, Belgium

## Reference

1. **Nouailhat, Alain.** *An Introduction to Nanoscience and Nanotechnology.* London : ISTE Ltd and John Wiley & Sons, Inc. , 2008. 978-1-84821-007-3 .
2. **Wolf, T, et al.** Subpicotesla Diamond Magnetometry. *Phys. Rev. X.* 2015, Vol. 5.
3. **Chang, Y. R. and al.** Mass production and dynamic imaging of fluorescent nanodiamonds. *nature Nanotechnology.* May, 2008, Vol. 3, 5.
4. **Petrakova, V. and al.** Luminescence of Nanodiamond Driven by Atomic Functionalization: Towards Novel Detection Principles. *Advance Functional Material.* 2012, Vol. 22.
5. —. Charge-Sensitive Fluorescent Nanosensors Created from Nanodiamond. *Nanoscale.* 2015, Vol. 7, 12307-12311.
6. —. Imaging of transfection and intracellular release of intact, non-labeled DNA using fluorescent nanodiamonds. *Nanoscale.* 23, 2016, Vol. 8, 12002-12.
7. **Havlik, J. and al.** Boosting nanodiamond fluorescence: towards development of brighter probes. *Nanoscale.* 2012.
8. **Perunicic, V. S., et al.** A quantum spin-probe molecular microscope. *Nature Communications.* 2016, Vol. 7, 12667.
9. **Schrand, A. and al.** Nanodiamond Particles: Properties and Perspectives for Bioapplications. *Critical Reviews in Solid State and Materials Sciences.* 2009, Vols. 1-2, Vol. 34.
10. **Vaijayanthimala, V. and Chang, H.C.** Functionalized fluorescent nanodiamonds for biomedical applications. *Nanomedicine.* January, 2009, Vol. 1, 4.
11. **Collins, A. T.** Intrinsic and extrinsic absorption and luminescence in diamond. *Physica B: Condensed Matter.* April, 1993, Vols. 1-4, Vol. 185.
12. **Walker, J.** Optical absorption and luminescence in diamond. *Reports on Progress in Physics* Email alert RSS feed. 10, 1979, vol. 42.
13. **Breeding, Ch. M. and Shigley, J. E.** The “type” classification system of diamonds and its importance in gemology. *Gemds and gemology.* Summer, 2009, Vol. 2, Vol. 45.
14. **Mochalin V.N., Shenderova O., Ho D., Gogotsi Y.** The properties and applications of nanodiamonds. *Nature Nanotechnology.* December, 2011, Vol. 7, 1.
15. **Bundy, F. P.** Direct Conversion of Graphite to Diamond in Static Pressure Apparatus. *The Journal of Chemical Physics.* 1963, Vol. 38, 631.
16. **May, P. W.** Diamond thin films: a 21st-century material. *Philosophical Transactions of the Royal Society of London A.* January, 2000, Vol. 358, 1766.
17. **Stacey, A., et al.** Controlled synthesis of high quality micro/nano-diamonds by microwave plasma chemical vapor deposition. *Diamond and Related Materials.* January, 2009, Vol. 18, 1.
18. **Yugo, S. and al.** Generation of diamond nuclei by electric field in plasma chemical vapor deposition. *Applied Physics Letters.* 04, 1991, Vol. 58, 10.
19. **Iakoubovskii, K., et al.** Structure and defects of detonation synthesis nanodiamond . *Diamond and Related Materials .* 2000, Vol. 9.
20. **Krueger, Anke.** Diamond Nanoparticles: Jewels for Chemistry and Physics. *Advanced Materials.* June, 2008, Vol. 20, 12.
21. **Boudou, J.-P. and al.** High yield fabrication of fluorescent nanodiamonds. *Nanotechnology.* 2009, Vol. 20, 23.
22. **Pham, L. M. and al.** Enhanced metrology using preferential orientation of nitrogen-vacancy centers in diamond. *Physical review B.* September, 2012, Vol. 86.
23. **Pham, Linh My.** *Magnetic Field Sensing with Nitrogen-Vacancy Color Centers in Diamond.* Cambridge, Massachusetts : Harvard University, 2013.
24. **Grotz, B. and al.** Charge state manipulation of qubits in diamond. *Nature Communications.* 2012.
25. **Felton, S. and al.** Electron paramagnetic resonance studies of the neutral nitrogen vacancy in diamond. *Physical review B.* 2008, Vol. 77.
26. **Goss, J. P. and al.** Vacancy-impurity complexes and limitations for implantation doping of diamond. *Physical Review B.* 2006, Vol. 72.
27. **Collins, A. T.** The Fermi level in diamond. *Journal of Physics: Condensed Matter.* 2002, Vol. 14, 14.
28. **Manson, N.B.** Photo-ionization of the nitrogen-vacancy center in diamond. *Diamond and Related Materials.* 2005, Vol. 14, 10.
29. **Gaebel, T. and al.** Photochromism in single nitrogen-vacancy defect in diamond. *Applied physics B.* 2006, Vol. 82.
30. **Balasubramanian, G. and al.** Ultralong spin coherence time in isotopically engineered diamond. *Nature materials.* 2009, Vol. 8.
31. **Doherty, M. W. and al.** The nitrogen-vacancy colour centre in diamond. *Physics Report.* 2013, Vol. 528, 1.

32. **Gali, A., Fyta, M. and Kaxiras, E.** Ab initio supercell calculations on nitrogen-vacancy center in diamond: Electronic structure and hyperfine tensors. *Physical review B*. April, 2008, Vol. 77, 155206.
33. **Doherty, M. W. and al.** Theory of the ground-state spin of the NV<sup>-</sup> center in diamond. *Physical review B*. May, 2012, Vol. 85, 205203.
34. **Carbonera, D.** Optically detected magnetic resonance (ODMR) of photoexcited triplet states. *Photosynthesis Research*. 2009, Vol. 102, 2-3.
35. **Acosta, V. M.** *Optical Magnetometry with Nitrogen-Vacancy Centers in Diamond*. Berkeley : University of California, 2011.
36. **Schafer-Nolte, E. O.** *Development of a Diamond-based Scanning Probe Spin Sensor Operating at Low Temperature in Ultra High Vacuum*. Stuttgart : 3. Physikalisches Institut der Universität Stuttgart, 2014.
37. **Acosta, V. M. and al.** Diamonds with a high density of nitrogen-vacancy centers for magnetometry applications. *Physical review B*. 2009, Vol. 80, 115202.
38. **Acosta, V. M., et al.** Optical properties of the nitrogen-vacancy singlet levels in diamond. *Physical review B*. November, 2010, Vol. 82, 201202.
39. **Bradac, C.** *The properties of nitrogen-vacancy centres in nanodiamond*. Sydney : Macquarie University, 2012.
40. **Harrison, J., Sellars, M. J. and Manson, N. B.** Measurement of the optically induced spin polarisation of N-V centres in diamond. *Diamond and Related Materials*. 2005, Vol. 15, 4-8.
41. **Pham, L. M. and al.** Magnetic field imaging with nitrogen-vacancy ensembles. *Nee journal of medicine*. April, 2011, Vol. 13, 045021.
42. **Batalov, A. and al.** Temporal Coherence of Photons Emitted by Single Nitrogen-Vacancy Defect Centers in Diamond Using Optical Rabi-Oscillation. *Physical review letters*. 2008, Vol. 100, 077401.
43. **Striebel, F. T.** *Engineering of Diamond for integrated Quantum Optics and Magnetometry*. Ulm : Ulm University, 2012.
44. **Geiselmann, M.** *All optical manipulation of a single nitrogen-vacancy centre in nanodiamond*. Barcelona : Universitat Politècnica de Catalunya, 2014.
45. **Han, K. Y., Hell, S. W. and al.** Three-Dimensional Stimulated Emission Depletion Microscopy of Nitrogen-Vacancy Centers in Diamond Using Continuous-Wave Light. *Nano Letters*. 2009, Vol. 9, 9.
46. **Pinto, H. and al.** Theory of the surface effects on the luminescence of the NV<sup>-</sup> defect in nanodiamond. *Physica status solidi A*. 2011, Vol. 208, 9.
47. **Rondin, L. and al.** Surface-induced charge state conversion of nitrogen-vacancy defects in nanodiamonds. *Physical review B*. 2010, Vol. 82, 115449.
48. **Say, J. M. and al.** Fluorescent Nanodiamonds for Biological Applications. *Optical Society of America*. 2011, Vol. PS2.
49. **Kalish, R. and al.** Nitrogen doping of diamond by ion implantation. *Diamond and Related Materials*. March, 1997, Vol. 6, 2-4.
50. **Rabeau, J. R. and al.** Implantation of labelled single nitrogen vacancy centers in diamond using 15N. *Applied Physics Letters*. 2006, Vol. 88, 2.
51. **Rabeau, J. and al.** Single Nitrogen Vacancy Centers in Chemical Vapor Deposited Diamond Nanocrystals. *Nano Letters*. 2007, Vol. 7, 11.
52. **Edmonds, A. M. and al.** Production of oriented nitrogen-vacancy color centers in synthetic diamond. *Physical review B*. July, 2012, Vol. 86, 035201.
53. **Rabeau, J. R. and al.** Implantation of labelled single nitrogen vacancy centers in diamond using 15N. *Applied Physics Letters*. 2006, Vol. 88, 2.
54. **Maertz, B. J.** Vector magnetic field microscopy using nitrogen vacancy centers in diamond. *Applied Physics Letters*. 2010, Vol. 96, 9.
55. **Taylor, J. M. and al.** High-sensitivity diamond magnetometer with nanoscale resolution. *Nature Physics*. 2008, Vol. 4, 810-816.
56. **Schweiger, A. and Jeschke, G.** *Principles of Pulse Electron Paramagnetic Resonance*. Oxford : Springer-Verlag, 2001. 0937-9347.
57. **He, X.-F., Manson, N. B. and Fisk, P. T. H.** Paramagnetic resonance of photoexcited N- V defects in diamond. I. Level anticrossing in the 3A ground state. *Physical Review B*. 1993, Vol. 8809, 47.
58. **Takahashi, S., et al.** Quenching Spin Decoherence in Diamond through Spin Bath Polarization. *Physical Review Letters*. 2008, Vol. 197601, 108.
59. **Jarmola, A., et al.** Temperature- and Magnetic-Field-Dependent Longitudinal Spin Relaxation in. *Physical Review Letter*. 2012, Vol. 108, 197601.
60. **Yamamoto, T. and al.** Extending spin coherence times of diamond qubits by high-temperature annealing. *Physical Review B*. 2013, Vol. 075206, 88.
61. **King, J. P., Coles, P. J. and Reimer, J. A.** Optical polarization of C 13 nuclei in diamond through nitrogen vacancy centers. *Physical Review B*. 2010, Vol. 073201, 81.

62. **Lawson, S. C., et al.** On the existence of positively charged single-substitutional nitrogen in diamond. *Journal of Physics: Condensed Matter*. 1998, Vol. 6171, 10.
63. **Hanson, R., et al.** Coherent dynamics of a single spin interacting with an adjustable spin bath. *Science*. 2008, 320.
64. **Tisler, J and al.** Fluorescence and spin properties of defects in single digit nanodiamonds. *ACS nano*. 2009, 3.
65. **Balasubramanian, G. and al.** Nanoscale imaging magnetometry with diamond spins under ambient conditions. *Nature*. 2008, Vol. 455, 7213.
66. **Faust, T., et al.** Coherent control of a classical nanomechanical two-level system. *Nature Physics*. 2013, Vol. 9, 485–488.
67. **Wasilevsky, W., et al.** Quantum noise limited and entanglement-assisted magnetometry. *Physical Review Letters*. 2010, Vol. 104, 209902.
68. **Edelstein, A.** Advances in magnetometry. *Journal of Physics: Condensed Matter*. 28pp, 2007, Vol. 165217, 19.
69. **Fishbine, B.** SQUID magnetometry: Harnessing the Power of Tiny Magnetic Fields. *Los Alamos Reaserch Quarterly*. Spring, 2003.
70. **Rondin, L., et al.** Magnetometry with nitrogen-vacancy defects in diamond. *Reports on Progress in Physics*. 26pp, 2014, Vol. 056503, 77.
71. **Hong, S. and al.** Nanoscale magnetometry with NV centers in diamond. *MRS bulletin*. 2013, 38.
72. **Williamson, S.J., Romani, G.-L., Kaufman, L., Modena, I.** *Biomagnetism: An Interdisciplinary Approach*. Rome : Springer Science, 1983. ISBN 978-1-4757-1787-7.
73. **Webster, J. G.** *The Measurement, Instrumentation and Sensors Handbook*. Florida : CRC Press LCC, 1999. 0-8493-2145-X.
74. **Budker, D. and Romalis, M.** Optical magnetometry. *Nature Physics*. April, 2007, vol. 3.
75. **Mamin, H. J. and al.** Nanoscale Nuclear Magnetic Resonance with a Nitrogen-Vacancy Spin Sensor. *Science*. February, 2013, Vol. 1, Vol. 339.
76. **Geiselmann, M. and al.** Three-dimensional optical manipulation of a single electron spin. *Nature Nanotechnology*. March, 2013, Vol. 8.
77. **Acosta, V. M. and al.** Temperature Dependence of the Nitrogen-Vacancy Magnetic Resonance in Diamond. *Physical Review Letters*. 2011, Vol. 106, 209901.
78. **Togan, E. and al.** Quantum entanglement between an optical photon and a solid-state spin qubit. *Nature*. 2010, Vol. 446.
79. **Van Oort, E. and Glasbeek, M.** Electric-field-induced modulation of spin echoes of N-V centers in diamond. *Chemical Physics Letters*. 1990, Vol. 168, 6.
80. **Dolde, F. and al.** Electric-field sensing using single diamond spins. *Nature Physics*. 2011, Vol. 7.
81. **Maurer, C.P. and al.** Room-Temperature Quantum Bit Memory Exceeding One Second. *Science*. 2012, Vol. 336, 6086.
82. **Rugar D., R. Budakian, H. J. Mamin, and B. W. Chui.** Single spin detection by magnetic resonance force microscopy. *Nature*. 2004, Vol. 430.
83. **Degen, L. C.** Scanning magnetic field microscope with a diamond single-spin sensor. *Applied Physics Letter*. Vol. 92, 24.
84. **Schoenfeld, R. S. and Harneit W.** Real Time Magnetic Field Sensing and Imaging Using a Single Spin in Diamond. *Physical review letters*. 2011, Vol. 106, 030802.
85. **Maletinsky, P. and al.** A robust scanning diamond sensor for nanoscale imaging with single nitrogen-vacancy centres. *Nature nanotechnology*. 2012, Vol. 7.
86. **Rittweger, E., Wildanger, D. and Hell, S. W.** Far-field fluorescence nanoscopy of diamond color centers by ground state depletion. *Europhysics Letters*. Vol. 86, 1.
87. **Han, K. Y., et al.** Metastable dark states enable ground state depletion microscopy of nitrogen vacancy centers in diamond with diffraction-unlimited resolution. *Nano Letters*. 2010, Vol. 10, 8.
88. **Maurer, P. C. and al.** Far-field optical imaging and manipulation of individual spins with nanoscale resolution. *Nature Physics*. 2010, Vol. 6.
89. **Waldherr, G. and al.** Dark States of Single Nitrogen-Vacancy Centers in Diamond Unraveled by Single Shot NMR. *Physical review letters*. 2011, Vol. 106, 157601.
90. **Steinert, A. and al.** High sensitivity magnetic imaging using an array of spins in diamond. *Review of scientific instruments*. 2010, Vol. 81, 043705.
91. **Acosta, V. M. and al.** Broadband magnetometry by infrared-absorption detection of diamond NV centers. *Applied Physics Letters*. 2010, Vol. 97, 174104.
92. **Grotz, B. and al.** Sensing external spins with nitrogen-vacancy diamond. *New Journal of Physics*. 2011, 13.
93. **Staudacher, T., et al.** *Science*. 2013, Vol. 339, 6119.
94. **Davies, G.** Vibronic spectra in diamond. *Journal of Physics C: Solid State Physics*. 1974, Vol. 7, 20.

95. **Fuchs, G. D., et al.** Gigahertz dynamics of a strongly driven single quantum spin. *Science*. 2009, Vol. 326, 5959.
96. **Maze, J. R. and al.** Nanoscale magnetic sensing with an individual electronic spin in diamond. *Nature*. 2008, Vol. 455.
97. **Clarke, J. and Braginski, A. I.** *The SQUID Handbook*. Weinheim : WILEY, 2004. 3-527-40229-2.
98. **Sage, D. Le and al.** Optical magnetic imaging of living cells. *Nature*. 2013, Vol. 496.
99. **Jelezko, F. and Wrachtrup, J.** Single defect centres in diamond: A review. *Physica status solidi (a)*. 2006, Vol. 203, 13.
100. **Manson, N. B., Harrison, J. P. and Sellars, M. J.** Nitrogen-vacancy center in diamond: Model of the electronic structure and associated dynamics. *Physical review B*. 2006, Vol. 74, 104303.
101. **Bradac, C. and al.** Observation and control of blinking nitrogen-vacancy centres in discrete nanodiamonds. *Nature Nanotechnology*. 2010, Vol. 5.
102. **Weissleder, R. and Ntziachristos, V.** Shedding light onto live molecular targets. *Nature Medicine*. 2003, Vol. 9, 1.
103. **Hall, L. T. and al.** Monitoring ion-channel function in real time through quantum decoherence. *Proc Natl Acad Sci U S A*. 2010, Vol. 107, 4.
104. **McGuinness, L. P. and al.** Ambient Nanoscale Sensing with Single Spins Using Quantum Decoherence. *New Journal of Physics*. 2013, Vol. 15, 073042.
105. **Chen, M. and al.** Nanodiamond-mediated delivery of water-insoluble therapeutics. *ACS Nano*. 2008, Vol. 2, 10.
106. **Slegerova, J. and al.** Nanodiamonds as Intracellular Probes for Imaging in Biology and Medicine. [book auth.] Iwasaki Y., Harada A. Prokop A. *Intracellular Delivery II*. s.l. : Springer, 2014.
107. **Schirhagl, R., et al.** Nitrogen-Vacancy Centers in Diamond: Nanoscale Sensors for Physics and Biology. *Annual Review of Physical Chemistry*. 2014, Vol. 65.
108. **Faklaris, O. and al.** Photoluminescent nanodiamonds: Comparison of the photoluminescence saturation properties of the NV color center and a cyanine dye at the single emitter level, and study of the color center concentration under different preparation conditions. *Diamond and Related Materials*. 2010, Vol. 19, 7-9.
109. **Loveland, W. D., Morrissey, D. J. and Seaborg, G. T.** *Modern nuclear chemistry*. New Jersey : John Wiley & Sons, Inc., 2006. 13 978-0-471-11532-8.
110. **Campbell, B. and al.** Lattice damage caused by the irradiation of diamond. *Nuclear Instruments and Methods in Physics Research Section A: Accelerators, Spectrometers, Detectors and Associated Equipment*. 2002, Vol. 476, 3.
111. **Palmer, W. D.** Irradiation damage in diamond, especially by electrons in the MeV range. [book auth.] G. Davies. *Properties and Growth of Diamond*. London : INSPEC, 1994.
112. **Mainwood, A., Cunningham, J. and Usher, D.** Radiation damage of silicon and diamond by high energy neutrons, protons and  $\alpha$  particles. *Materials Science Forum*. 1997, Vol. 787.
113. **Iakubovskii, K., Dannefaer, S. and Stesmans, A.** Evidence for vacancy-interstitial pairs in Ib-type diamond. *Physical review B*. 2005, Vol. 71, 233201.
114. **Zaitsev, A. M.** *Optical Properties of Diamond*. Berlin : Springer-Verlag Berlin Heidelberg, 2001. 978-3-540-66582-3.
115. **Song, X. and al.** Generation of nitrogen-vacancy color center in nanodiamonds by high temperature annealing. *Applied Physics Letters*. 2013, Vol. 102, 13.
116. **Robinson, J. T. and al.** Properties of Fluorinated Graphene Films. *Nano Letters*. 8, 2010, Vol. 10, 3001-3005.
117. **Cheng, S.-H. and al.** Reversible fluorination of graphene: Evidence of a two-dimensional wide bandgap semiconductor. *Physical Review B*. 2010, Vol. 81, 205435 .
118. **Zboril, R. and al.** Graphene Fluoride: A Stable Stoichiometric Graphene Derivative and its Chemical Conversion to Graphene. *Small*. 24, 2010, Vol. 6, 2885–2891.
119. **Gu, Z. and al.** Cutting Single-Wall Carbon Nanotubes through Fluorination. *Nano Letters*. 9, 2002, Vol. 2, 1009–1013.
120. **Mickelson, E. T. and al.** Fluorination of single-wall carbon nanotubes. *Chemical Physics Letters*. 1998, Vol. 296, 188-194.
121. **Liu, Y., Vander Wal, R. L. and Khabashesku, V. N.** Functionalization of Carbon Nano-onions by Direct Fluorination. *Chemistry of Materials*. 4, 2007, Vol. 19, 778-786.
122. **Plank, N. O. V. and Cheung, R.** Thiolation of single-wall carbon nanotubes and their self-assembly. *Applied Physics Letters*. 15, 2004, Vol. 85.
123. **Osterkamp, Ch. and al.** Stabilizing shallow color centers in diamond created by nitrogen delta-doping using SF<sub>6</sub> plasma treatment. *Applied Physics Letters*. 11, 2015, Vol. 106.
124. **Ohashi, K. and al.** Negatively Charged Nitrogen-Vacancy Centers in a 5 nm Thin 12C Diamond Film. *Nano Letters*. 10, 2016, Vol. 13, 4733–4738.

125. **Aharonovich, I., Greentree, A. D. and Prawer, S.** Diamond photonics. *Nature Photonics*. 2011, Vol. 5, 397–405.
126. **Pfaff, W. and al.** Unconditional quantum teleportation between distant solid-state quantum bits. *Science*. 6196, 2014, Vol. 345, 532-535.
127. **Gruber, A. and al.** Scanning Confocal Optical Microscopy and Magnetic Resonance on Single Defect Centers. *Science*. 5321, 1997, Vol. 276, 2012-2014.
128. **Bourgeois, E. and al.** Photoelectric detection of electron spin resonance of nitrogen-vacancy centres in diamond. *Nature Communication*. 2015, Vol. 6, 8577.
129. **Kealey, Ch. P. and al.** Fluorination of polycrystalline diamond films and powders. An investigation using FTIR spectroscopy, SEM, energy-filtered TEM, XPS and fluorine-18 radiotracer methods. *Journal of Materials Chemistry*. 2001, Vol. 11, 879-886.
130. **Lud, S. Q. and al.** Electronic properties of ultrananocrystalline diamond surfaces. *Applied Physics Letters*. 2010, Vol. 96, 092109.
131. **Freedman, A.** Halogenation of diamond (100) and (111) surfaces by atomic beams. *Journal of Applied Physics*. 1994, Vol. 75, 3112.
132. **Smentkowski, V. S. and Yates, J. T. Jr.** Fluorination of Diamond Surfaces by Irradiation of Perfluorinated Alkyl Iodides. *Science*. 5246, 1996, Vol. 271, 193-195.
133. **Panich, A. M. and al.** Structure and Bonding in Fluorinated Nanodiamond. *Journal of Physical Chemistry*. 2, 2010, Vol. 114, 774–782.
134. **Ray, M. A. and al.** Cold plasma functionalization of nanodiamond particles. *Diamond and Related Materials*. 11-12, 2006, Vol. 15, 1809–1812.
135. **Klauser, F. and al.** Direct and Protein-Mediated Cell Attachment on Differently Terminated Nanocrystalline Diamond. *Chemical Vapor Deposition*. 1-3, 2010, Vol. 16, 42-49.
136. **Rehor, I., Cigler, P.** Precise estimation of HPHT nanodiamond size distribution based on transmission electron microscopy image analysis. *Diamond and Related Materials*. 2014, Vol. 46, 21-24.
137. **Liu, Y. and al.** Functionalization of Nanoscale Diamond Powder: Fluoro-, Alkyl-, Amino-, and Amino Acid-Nanodiamond Derivatives. *Chemistry of Materials*. 20, 2004, Vol. 16, 3924–3930.
138. **Dolenko, T. A. and al.** Diamond–Water Coupling Effects in Raman and Photoluminescence Spectra of Nanodiamond Colloidal Suspensions. *The Journal of Physical Chemistry*. 45, 2012, Vol. 116, 24314–24319.
139. **Wolcott, A. and al.** Surface Structure of Aerobically Oxidized Diamond Nanocrystals. *The Journal of Physical Chemistry*. 46, 2014, Vol. 118, 26695–26702.
140. **Wang, X. and al.** Higher coverage of carboxylic acid groups on oxidized single crystal diamond (001). *Diamond and Related Materials*. 10, 2011, Vol. 20, 1319–1324.
141. **Nguyen, T.-T.-B., Chang, H.-Ch. and Wu, V. W.-K.** Adsorption and hydrolytic activity of lysozyme on diamond nanocrystallites. *Diamond and Related Materials*. 47, 2007, Vol. 16, 872–876.
142. **Patel, N. R. and Flowers, R. A. 2nd.** Mechanistic study of silver-catalyzed decarboxylative fluorination. *Journal of Organic Chemistry*. 11, 2015, Vol. 80, 5834-41.
143. **Hoste, H., Van De Vondel, D. F. and P., Van Der Kelen. G.** XPS Spectra of organometallic phenyl compounds of P, As, Sb and Bi. *Journal of Electron Spectroscopy and Related Phenomena*. 3, 1979, Vol. 17, 191-195.
144. **Mohan, N. and al.** Sub-20-nm Fluorescent Nanodiamonds as Photostable Biolabels and Fluorescence Resonance Energy Transfer Donors. *Advanced Materials*. 7, 2010, Vol. 22, 843–847.
145. **Stacey, A. and al.** Nitrogen Terminated Diamond. *Advanced Materials Interfaces*. 10, 2015, Vol. 2, 1500079.
146. **Cui, S. and Hu, E. L.** Increased negatively charged nitrogen-vacancy centers in fluorinated diamond. *Applied Physics Letters*. 5, 2013, Vol. 103, 051603.
147. **Cai, J. and al.** A large-scale quantum simulator on a diamond surface at room temperature. *Nature Physics*. 2013, Vol. 9, 168–173.
148. **Moore, L. and al.** Comprehensive interrogation of the cellular response to fluorescent, detonation and functionalized nanodiamonds. *Nanoscale*. 2014, Vol. 20, 6.
149. **Faklaris, O. and al.** Photoluminescent Diamond Nanoparticles for Cell Labeling: Study of the Uptake Mechanism in Mammalian Cells. *ACS Nano*. 2009, Vol. 3, 12.
150. **Chu, Z., et al.** Unambiguous observation of shape effects on cellular fate of nanoparticles. *Scientific Reports*. 2014, Vol. 4, 4495.
151. **Chao, J.-I. and al.** Nanometer-Sized Diamond Particle as a Probe for Biolabeling. *Biophysical Journal*. 2007, Vol. 93, 2199–2208.
152. **Cheng, C.-Y. and al.** Direct and in vitro observation of growth hormone receptor molecules in A549 human lung epithelial cells by nanodiamond labeling. *Applied Physics Letters*. 2007, Vol. 90, 163903.
153. **Perevedentseva, E. and al.** The interaction of the protein lysozyme with bacteria E. coli observed using nanodiamond labelling. *Nanotechnology*. 2007, Vol. 18, 315102.

154. —. Nanodiamond internalization in cells and the cell uptake mechanism. *Journal of Nanoparticle Research*. 2013, Vol. 15, 1834.
155. **Pope, I. and al.** Coherent anti-Stokes Raman scattering microscopy of single nanodiamonds. *Nature Nanotechnology*. 2014, Vol. 9, 940–946.
156. **Uzunbajakava, N., et al.** Nonresonant Confocal Raman Imaging of DNA and Protein Distribution in Apoptotic Cells. *Biophysical Journal*. 2003, Vol. 84, 3968.
157. **MacQueen, J.** Some Methods for Classification and Analysis of MultiVariate Observations. *Proc. of the fifth Berkeley Symposium on Mathematical Statistics and Probability*. 1967, Vol. 1, 281-297.
158. **Salehi, H. and al.** Label-free detection of anticancer drug paclitaxel in living cells by confocal Raman microscopy. *Applied Physics Letter*. 2013, Vol. 102, 113701.
159. **Salehi, H and al.** Confocal Raman spectroscopy to monitor intracellular penetration of TiO<sub>2</sub> nanoparticles. *Journal of Raman Spectroscopy*. 2014, Vol. 45, 807–813.
160. **Hui, Y. Y., Cheng, Ch.-L. and Chang, H.-Ch.** Nanodiamonds for optical bioimaging. *Journyl of Physics D: Applied Physics*. 2010, Vol. 43, 374021.
161. **Martin, M. and al.** Morphology and Nanomechanics of Sensory Neurons. *PLOS One*. 2, 2013, Vol. 8, e56286.
162. **Snijder, B. and al.** Population context determines cell-to-cell variability in endocytosis and virus infection. *Nature*. 2009, Vol. 461, 520-523.
163. **Boucrot, E. and Kirchhausen, T.** Endosomal recycling controls plasma membrane area during mitosis. *PNAS*. 2007, Vol. 104, 7939–7944.
164. **Kim, J. A. and al.** Role of cell cycle on the cellular uptake and dilution of nanoparticles in a cell population. *Nature Nanotechnology*. 2012, Vol. 7, 62–68.
165. **Raucher, D. and Sheetz, M. P.** Characteristics of a membrane reservoir buffering membrane tension. *Biophysical Journal*. 4, 1999, Vol. 77, 1992–2002.
166. **Schweitzer, J.K. and al.** Endocytosis resumes during late mitosis and is required for cytokinesis. *Journal of Biological Chemistry*. 50, 2005, Vol. 280, 41628–41635.
167. **Momenzadeh, S. A. and al.** Nanoengineered Diamond Waveguide as a Robust Bright Platform for Nanomagnetometry Using Shallow Nitrogen Vacancy Centers. *Nano Letters*. 2015, Vol. 15, 1.
168. **Li, L. and al.** Efficient photon collection from a nitrogen vacancy center in a circular bullseye grating. *Nano Letters*. 2015, Vol. 15.
169. **Childress, L. and Hanson, R.** Diamond NV centers for quantum computing and quantum networks. *MRS Buletin*. 2015, Vol. 38, 134-138.
170. **Shields, B. J., et al.** Efficient readout of a single spin state in diamond via spin-to-charge conversion. *Physical Review Letters*. 2015, Vol. 114, 136402.
171. **Brenneis, A. and al.** Ultrafast electronic read-out of diamond NV centers coupled to graphene. *Nature Nanotechnology*. 2014, Vol. 10, 135–139.
172. **Visconti, P. and al.** The fabrication of sub-10 nm planar electrodes and their use for a molecule-based transistor. *Nanotechnology*. 2004, Vol. 15, 807.
173. **Remes, Z., et al.** Mechanism of photoconductivity in intrinsic epitaxial CVD diamond studied by photocurrent spectroscopy and photocurrent decay measurements. *Diamond Related Materials*. 2005, Vol. 14, 556-560.
174. **Jensen, K., et al.** Light narrowing of magnetic resonances in ensembles of nitrogen-vacancy centers in diamond. *Physical review B*. 2013, Vol. 87, 014115.
175. **Aslam, N., et al.** Photo-induced ionization dynamics of the nitrogen vacancy defect in diamond investigated by single-shot charge state detection. *New Journal of Physics*. 2013, Vol. 15, 013064.
176. **Weber, J. R. and al.** Quantum computing with defects. *PNAS*. 2010, Vol. 107, 014115.
177. **Siyushev, P. and al.** Optically controlled switching of the charge state of a single nitrogen-vacancy center in diamond at cryogenic temperatures. *Physical review letters*. 2013, Vol. 110, 176402.
178. **Rosa, J. and al.** Simultaneous characterization of defect states in CVD diamond by PDS, EPR, Raman and photocurrent spectroscopies. *Diamond and Related Materials*. 1998, Vol. 7, 1048-1053.
179. **Hanson, R., Gywat, O and Awschalom, D. D.** Room-temperature manipulation and decoherence of a single spin in diamond. *Physical Review B*. 2006, Vol. 74, 161203(R).
180. **Laraoui, A. and Meriles, C. A.** Rotating frame spin dynamics of a Nitrogen-Vacancy center in a diamond nanocrystal. *Physical Review B*. 2011, Vol. 84, 161403.
181. **Doherty, M. W., et al.** The nitrogen-vacancy colour centre in diamond. *Physics Reports*. 2013, Vol. 528, 1, pp. 1-45.
182. **Tetienne, J.-P. and al.** Magnetic-field-dependent photodynamics of single NV defects in diamond: an application to qualitative all-optical magnetic imaging. *New Journal of Physics*. 2012, Vol. 14, 103033.
183. **Mrózek, M., et al.** Circularly polarized microwaves for magnetic resonance study in the GHz range: Application to nitrogen-vacancy in diamonds. *Applied Physisc Letters*. 2015, Vol. 107, 013505.

184. **Gali, A. and al.** Theory of Spin-Conserving Excitation of the NV- Center in Diamond. *Physical Review Letters*. 2009, Vol. 103, 186404.
185. **Krukau, A. V. and al.** Influence of the exchange screening parameter on the performance of screened hybrid functionals. *The Journal of Chemical Physics*. 2006, Vol. 125, 224106.
186. **Perdew, J. P., Burke, K. and Ernzerhof, M.** Generalized Gradient Approximation Made Simpl. *Physical Review Letters*. 1996, Vol. 77, 1396.
187. **Inkson, J. C.** Deep impurities in semiconductors. II. The optical cross section. *Journal of Physics C: Solid State Physics*. 1981, Vol. 14, 1093-1101.
188. **Nesladek, M. and al.** Dominant defect levels in diamond thin films: A photocurrent and electron paramagnetic resonance study. *Applied Physics Letters*. 25, 1998, Vol. 72, 3306.
189. **Enckevort, W. J. P. and Versteegen, E. H.** Temperature dependence of optical absorption by the single-substitutional nitrogen donor in diamond. *Journal of Physics: Condensed Matter*. 9, 1992, Vol. 4, 2361.
190. **Deàk, P. and al.** Formation of NV centers in diamond: A theoretical study based on calculated transitions and migration of nitrogen and vacancy related defects. *Physical Review B*. 2014, Vol. 89, 075203.
191. **Goldman, M. L. and al.** State-selective intersystem crossing in nitrogen-vacancy centers. *Physical Review B*. 2015, Vol. 91, 165201.
192. **Pirandola, S. and Braunstein, S. L.** Physics: Unite to build a quantum Internet. *Nature*. 2016, Vol. 532, 7598.
193. **Morello, A. and al.** Single-shot readout of an electron spin in silicon. *Nature*. 2010, Vol. 467, 687–691.
194. **Neumann, P., et al.** High-Precision Nanoscale Temperature Sensing Using Single Defects in Diamond. *Nano Lett.* 6, 2013, Vol. 13, 2738–2742.
195. **Chen, J., et al.** Optical quenching and recovery of photoconductivity in single-crystal diamond. *arXiv:1607.08354*. 2016.
196. **Bourgeois, E. and al.** Enhanced photoelectric detection of NV magnetic resonances in diamond under dual-beam excitation. *Phys. Rev. B (accepted)*. 2016.
197. **Hrubesch, F. M. and al.** Efficient electrical spin readout of NV- centers in diamond. *Phys. Rev. Lett. (accepted)*. 2017, see arXiv:1608.02459.
198. **Childress, L. and al.** Coherent dynamics of coupled electron and nuclear spin qubits in diamond. *Science*. 2006, Vol. 314, 5797.
199. **Xin, H. and al.** Influence of Microwave Detuning on Ramsey Fringes of a Single Nitrogen. *Chinese Physics Letters*. 2012, Vol. 29, 2.
200. **Grèzes, C.** *Towards a Spin-Ensemble Quantum Memory for Superconducting Qubits*. s.l. : Springer, 2015.
201. **Liu, G.-Q. and al.** *Controllable effects of quantum fluctuations on spin free-induction decay at room temperature*. Scientific Reports : 2, 2012. 432.
202. **Horowitz, V. R., et al.** Electron spin resonance of nitrogen-vacancy centers in optically trapped nanodiamonds. *PNAS*. 2012, Vol. 109, 34.
203. **Mandelis, A.** Signal-to-noise ratio in lock-in amplifier synchronous detection: A generalized communications systems approach with applications to frequency, time, and hybrid (rate window) photothermal measurements. *Review of Scientific Instruments*. 1994, Vol. 65, 3309.
204. **Rehor, I. and al.** Fluorescent Nanodiamonds Embedded in Biocompatible Translucent Shells. *Small*. 2014, Vol. 10, 6.
205. **Slegerova, J. et al.** Designing the nanobiointerface of fluorescent nanodiamonds: highly selective targeting of glioma cancer cells. *Nanoscale*. 2015, Vol. 7, 2.
206. **Rehor, I. and al.** Fluorescent Nanodiamonds with Bioorthogonally Reactive Protein-Resistant Polymeric Coatings. *ChemPlusChem*. 2014, Vol. 79, 1.
207. **Ho, D.** Beyond the sparkle: the impact of nanodiamonds as biolabeling and therapeutic agents. *ACS Nano*. 2009, Vol. 3, 12.
208. **Vaijayanthimala, V., et al.** The long-term stability and biocompatibility of fluorescent nanodiamond as an in vivo contrast agent. *Biomaterials*. 2012, Vol. 33, 31.
209. **Liu, K. K., et al.** Endocytic carboxylated nanodiamond for the labeling and tracking of cell division and differentiation in cancer and stem cells. *Biomaterials*. 30, 2009, 26.
210. **Schrand, A. M., et al.** Are Diamond Nanoparticles Cytotoxic? *The Journal of Physical Chemistry B*. 111, 2007, 1.
211. **Mohan, N., et al.** In vivo imaging and toxicity assessments of fluorescent nanodiamonds in *Caenorhabditis elegans*. *Nano Letters*. 10, 2010, 9.
212. **Wu, Y., et al.** Diamond Quantum Devices in Biology. *Angewandte Chemie International Edition*. 2016, Vol. 55, 23.
213. **N., Billinton. and Knight, A. W.** Seeing the wood through the trees: a review of techniques for distinguishing green fluorescent protein from endogenous autofluorescence. *Analytical Biochemistry*. 2001, Vol. 291.

214. **Collins, A. T., Thomaz, M. F. and Jorge, M. I. B.** Luminescence decay time of the 1.945 eV centre in type Ib diamond. *Journal of Physics C: Solid State Physics*. 1983, Vol. 16, 81.
215. **Chen, X. and Zhang, W.** Diamond nanostructures for drug delivery, bioimaging, and biosensing. *Chemical Society Reviews*. 3, 2017.
216. **Lam, R and Ho, D.** Nanodiamonds as vehicles for systemic and localized drug delivery. *Expert Opinion on Drug Delivery*. 6, 2009, 9.
217. **Huang, H., et al.** Active Nanodiamond Hydrogels for Chemotherapeutic Delivery. *Nano Letters*. 7, 2007, 11.
218. **Vinante, M., et al.** Human plasma protein adsorption on carbon-based materials. *Journal of Nanoscience and Nanotechnology*. 9, 2009, 6.
219. **Krueger, A. and Lang, D.** Functionality is Key: Recent Progress in the Surface Modification of Nanodiamond. *Advanced Functional Materials*. 22, 2012, 5.
220. **Li, X., et al.** TAT-conjugated nanodiamond for the enhanced delivery of doxorubicin. *Journal of Materials Chemistry*. 22, 2001.
221. **Liu, K. K., et al.** Covalent linkage of nanodiamond-paclitaxel for drug delivery and cancer therapy. *Nanotechnology*. 20, 2010, 31.
222. **Zhang, Z., et al.** The use of lipid-coated nanodiamond to improve bioavailability and efficacy of sorafenib in resisting metastasis of gastric cancer. *Biomaterials*. 35, 2014, 15.
223. **Chow, E. K., et al.** Nanodiamond therapeutic delivery agents mediate enhanced chemoresistant tumor treatment. *Science Translational Medicine*. 3, 2011, 73.
224. **Man, H. B., et al.** Synthesis of nanodiamond-daunorubicin conjugates to overcome multidrug chemoresistance in leukemia. *Nanomedicine*. 10, 2014, 2.
225. **Cui, Z. F., et al.** Sodium alginate-functionalized nanodiamonds as sustained chemotherapeutic drug-release vectors. *Carbon*. 97, 2016, 78.
226. **Zhang, X. Q., et al.** Multimodal nanodiamond drug delivery carriers for selective targeting, imaging, and enhanced chemotherapeutic efficacy. *Advanced Materials*. 23, 2011, 41.
227. **Shimkunas, R. A., et al.** Nanodiamond-insulin complexes as pH-dependent protein delivery vehicles. *Biomaterials*. 30, 2009, 29.
228. **Purtov, K. V., et al.** Purtov KV, Petunin AI, Burov AE, Puzyr AP, Bondar VS. *Nanoscale Research Letters*. 5, 2010, 3.
229. **Alhaddad, A., et al.** Nanodiamond as a vector for siRNA delivery to Ewing sarcoma cells. *Small*. 7, 2011, 21.
230. **Lee, D. K., et al.** Nanodiamond-Gutta Percha Composite Biomaterials for Root Canal Therapy. *ACS Nano*. 9, 2015, 11.
231. **Ryu, T. K., et al.** Bone-targeted delivery of nanodiamond-based drug carriers conjugated with alendronate for potential osteoporosis treatment. *Journal of Controlled Release*. 28, 2016, 232.
232. **Wiethoff, C. M. and Middaugh, C. R.** Barriers to nonviral gene delivery. *Journal of Pharmaceutical Sciences*. 92, 2003, 2.
233. **Passeri, D., et al.** Biomedical Applications of Nanodiamonds: An Overview. *Journal of Nanoscience and Nanotechnology*. 15, 2015, 2.
234. **Martín, R., et al.** Fenton-treated functionalized diamond nanoparticles as gene delivery system. *ACS Nano*. 4, 2010, 1.
235. **Zhang, X. Q., et al.** Polymer-functionalized nanodiamond platforms as vehicles for gene delivery. *ACS Nano*. 3, 2009, 9.
236. **Kaur, R. and Badea, I.** Nanodiamonds as novel nanomaterials for biomedical applications: drug delivery and imaging systems. *International Journal of Nanomedicine*. 8, 2013, 203.
237. **Lai, L. and Barnard, A. S.** Functionalized Nanodiamonds for Biological and Medical Applications. *Journal of Nanoscience and Nanotechnology*. 15, 2015, 2.
238. **Fu, C. C., et al.** Characterization and application of single fluorescent nanodiamonds as cellular biomarkers. *Proceedings of the National Academy of Sciences of the USA*. 104, 2007, 3.
239. **Faklaris, O., et al.** Comparison of the photoluminescence properties of semiconductor quantum dots and non-blinking diamond nanoparticles. Observation of the diffusion of diamond nanoparticles in living cells. *Journal of the European Optical Society*. 4, 2009.
240. **Weng, M. F., et al.** Fluorescent nanodiamonds. *Diamond and Related Materials*. 18, 2009, 2-3.
241. **Epperla, C. P., et al.** Nanodiamond-Mediated Intercellular Transport of Proteins through Membrane Tunneling Nanotubes. *Small*. 11, 2015, 45.
242. **Liu, W., et al.** 3D Single-Molecule Imaging of Transmembrane Signaling by Targeting Nanodiamonds. *Advanced Functional Materials*. 26, 2016, 3.
243. **Yuan, Y., et al.** Biodistribution and fate of nanodiamonds in vivo. *Diamond and Related Materials*. 18, 2009, 1.

244. **Hegy, A. and Yablonovitch, E.** Molecular Imaging by Optically Detected Electron Spin Resonance of Nitrogen-Vacancies in Nanodiamonds. *Nano Letters*. 13, 2013, 3.
245. **McGuinness, L. P., et al.** Quantum measurement and orientation tracking of fluorescent nanodiamonds inside living cells. *Nature Nanotechnology*. 6, 2011, 358.
246. **Kucsko, G., et al.** Nanometre-scale thermometry in a living cell. *Nature*. 500, 2013, 54.
247. **Steinert, S., et al.** Magnetic spin imaging under ambient conditions with sub-cellular resolution. *Nature Communications*. 4, 2013.
248. **Sturasa, J. and al.** Mass production of fluorescent nanodiamonds with a narrow emission intensity distribution. *Carbon*. 96, 2016, 812.
249. **Simpson, D. A., et al.** Quantum magnetic resonance microscopy. *arXiv:1702.04418*. 2017.